



Corporate Office

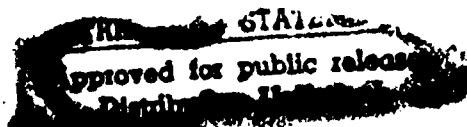
AD-A269 610



FINAL REPORT

Development of a Modified Betatron Accelerator

DTIC
ELECTE
SEP 21 1993
S E D



9

2

6

93-21857



**Best
Available
Copy**

SECURITY CLASSIFICATION: Unclassified

SFA-93/007

Development of a Modified Betatron Accelerator

Prepared by: Spencer Marsh, Kevin Smith, Steve Krafsig, and
Lloyd Seto

SFA, Inc.
1401 McCormick Drive
Landover, Maryland 20785

Date: August 1993

Contract Number: N00014-89-C-2265

Prepared for: Naval Research Laboratory
4555 Overlook Avenue, SW
Washington, DC 20375-5000

Accesion For	
NTIS	CRA&I
DTIC	TAB
Unannounced	
Justification	
By	
Distribution /	
Availability Codes	
Dist	Avail and / or Special
A-1	

2025 RELEASE UNDER E.O. 14176

REPORT DOCUMENTATION PAGE

Form Approved
OMB No. 0704-0188

Public reporting burden for this collection of information is estimated to average 1 hour per response, including the time for reviewing instructions, searching existing data sources, gathering and maintaining data needed, and completing and reviewing the collection of information. Send comments regarding this burden estimate or any other aspect of this collection of information, including suggestions for reducing this burden to Washington Headquarters Services, Directorate for Information Operations and Reports, 1215 Jefferson Davis Highway, Suite 1204, Arlington, VA 22202-4302, and to the Office of Management and Budget, Paperwork Reduction Project (0704-0188), Washington, DC 20503.

1. AGENCY USE ONLY (Leave Blank)		2. REPORT DATE August 1993	3. REPORT TYPE AND DATES COVERED Final Report 9/13/89 to 6/12/93
4. TITLE AND SUBTITLE Development of a Modified Betatron Accelerator		5. FUNDING NUMBERS N00014-89-C-2265	
6. AUTHOR(S) Spencer Marsh, Kevin Smith, Steve Krafsig, and Lloyd Seto			
7. PERFORMING ORGANIZATION NAME(S) AND ADDRESS(ES) SFA, Inc. 1401 McCormick Drive Landover, MD 20785		8. PERFORMING ORGANIZATION REPORT NUMBER SFA--93/007	
9. SPONSORING/MONITORING AGENCY NAME(S) AND ADDRESS(ES) Naval Research Laboratory 4555 Overlook Ave., SW Washington, DC 20375-5000		10. SPONSORING/MONITORING AGENCY REPORT NUMBER	
11. SUPPLEMENTARY NOTES			
12a. DISTRIBUTION/AVAILABILITY STATEMENT Approved for public release: Distribution is unlimited		12b. DISTRIBUTION CODE	
13. ABSTRACT (Maximum 200 words) Under contract N00014-89-C-2265, SFA provided support to the Naval Research Laboratory Beam Physics Branch by researching and developing the Modified Betatron. This branch is engaged in research and development of compact, high-power accelerators and their applications. The major research emphasis is on high-current, cyclic accelerators, such as the modified betatron located at NRL in Washington, DC. In a betatron, electrons are accelerated to high energies by an electric field. Particular applications of interest include intense coherent radiation sources and beam propagation. SFA has supported the Beam Physics Branch for 12 years. Under multiple tasks, SFA technical personnel have engineered, designed, fabricated, installed, and tested special-purpose equipment, components, and instruments for conducting various research projects to improve the capabilities of compact accelerators. This engineering and development work is performed in close collaboration with the experimental effort to ensure compatibility, optimal function, and effective use of government equipment and facilities.			
14. SUBJECT TERMS		15. NUMBER OF PAGES 52 pages	16. PRICE CODE
17. SECURITY CLASSIFICATION OF REPORT Unclassified	18. SECURITY CLASSIFICATION OF THIS PAGE Unclassified	19. SECURITY CLASSIFICATION OF ABSTRACT Unclassified	20. LIMITATION OF ABSTRACT Unlimited

Under contract N00014-89-C-2265, SFA provided support to the Naval Research Laboratory Beam Physics Branch by researching and developing the Modified Betatron. This branch is engaged in research and development of compact, high-power accelerators and their applications. The major research emphasis is on high-current, cyclic accelerators, such as the modified betatron located at NRL in Washington, DC. In a betatron, electrons are accelerated to high energies by an electric field. Particular applications of interest include intense coherent radiation sources and beam propagation.

SFA has supported the Beam Physics Branch for 12 years. Under multiple tasks, SFA technical personnel have engineered, designed, fabricated, installed, and tested special-purpose equipment, components, and instruments for conducting various research projects to improve the capabilities of compact accelerators. This engineering and development work is performed in close collaboration with the experimental effort to ensure compatibility, optimal function, and effective use of government equipment and facilities.

The goal of the modified betatron accelerator project was to accelerate a 1 kA electron beam to an energy of 50 MeV. The research program centered on the critical physics issues associated with this goal, such as beam stability, self field effects, image forces, and injection and extraction processes. Achievement of this goal revolutionized the DoD's directed-energy weapons technologies, establishing the Beam Physics Branch's modified betatron accelerator as the technological leader in the field. SFA has played an integral supporting role on this project from the novel construction of the vacuum chamber to expert operation and day-to-day maintenance and modification of the betatron.

The modified betatron accelerator is a large, complex facility. Several high-energy storage-capacitor banks and pulsed-power systems, with the associated distribution and coil systems, are required to create the various magnetic fields for acceleration and beam confinement and to supply the beam. In addition to the electrical components, the structural framework to support the betatron chamber and associated magnetic field coils must allow for precision positioning of the various coils and yet be able to withstand considerable forces and torques during a shot. Due to this complexity, extensive mechanical and electrical engineering was required for the modification and/or fabrication of new parts for the betatron. SFA's engineering support consisted of:

- *Design Engineering*—In cooperation with government scientists, SFA provided support to conceptualize research equipment that satisfied the structural, mechanical, electrical, vacuum, magnetic, electrostatic, cost, and schedule requirements of the project. SFA prepared layout drawings, performed analyses for such properties as strength and deflection, selected materials, and prepared detail drawings.
- *Development*—When required, SFA undertook the development of specific technologies that were necessary to successfully build required research equipment. SFA identified materials and located sources, located fabricators, and built prototypes. SFA obtained competitive bids and placed purchase requisitions, monitored the progress of fabricators, and took delivery of equipment as required. SFA also transported equipment to NRL; inspected the equipment; and assisted in installation, preliminary adjustments, and operation. This area also included fabricator development. In the past, research equipment fabrication requirements arose for which there was no known industrial base or the existing base was too expensive. SFA, therefore, worked with various contractors or subcontractors as required to assist in the development of the technology base. This was accomplished by locating contractors/subcontractors that possessed related skills, then educating them to develop the required base.
- *Testing*—SFA undertook extensive testing of individual components and materials to define and verify important characteristics relevant to the proposed use. SFA also maintained databases of test results, including both in-house testing and testing carried out at other sites. The development of new or modification of existing systems entails the design, assembly, testing, and installation of new components or modifications to existing components to improve the performance of the accelerator and to investigate key physics issues (such as extraction). Branch scientists were responsible for the conceptual design of equipment. Through interaction with SFA's engineers, the conceptual design was

refined and detailed designs produced. During this process, manufacturability of the equipment was also addressed. In particular, a straightforward design process can result in difficult-to-manufacture components. To ensure that designs were producible, SFA investigated several possible manufacturing processes at the outset. Using this approach, SFA often arrived at novel manufacturing solutions. An example of this was SFA's participation in the MBA vacuum chamber development. Several materials were considered for the chamber, and SFA engineers determined that a fiberglass/epoxy chamber would meet the project needs. To manufacture the components, a local fiberglass boat manufacturer was trained by SFA to produce the toroidal vacuum chamber sections. This effort resulted not only in a superior product but also in a reduction in cost.

In support of this contract, SFA has performed numerous tasks related to vacuum systems. These tasks have included vacuum chamber design, leak checking, and measurement of outgassing rates and pumpdown rates. Recently, SFA personnel designed a cylindrical vacuum chamber with a pumped volume of 0.5 m³ out of 304 stainless steel alloy. Thirty ports were designed to allow for electron gun introduction, optical observation, pumping connections, mechanical manipulation, and various diagnostics. These ports ranged in diameter from 1 inch to 8 inches. Single-side vacuum welds were specified to eliminate the possibility of virtual leaks—trapped pockets of gas on the interior of a vacuum system. Stress and stability analyses were carried out to ensure structural integrity. Procurement drawings were prepared and competitive bids were obtained. A contract was placed with a reasonable price and delivery schedule. During fabrication of the vacuum chamber, design work was completed on the support structures, baking and cooling systems, and pump selection. After delivery of the vacuum chamber, the system was assembled, groomed, and placed into operation. A single Sargent-Welch Turbo Molecular Pump Station having a capacity of 400 l/s was able to pump the system down to 2×10^{-7} torr in approximately 4 hours. With baking and further grooming, a vacuum of 7×10^{-8} torr was achieved.

Publications Appendix

APPENDIX

Table of Contents

Publication	Page
Beam extraction scheme from the modified betatron accelerator. C.A. Kapetanakos, S.J. Marsh, and D. Dialetis. <i>Physical Review Letters</i> 61, No. 1: 86-9	4
Improved beam confinement in the modified betatron with strong focusing. C.A. Kapetanakos, L.K. Len, T. Smith, J. Golden, K. Smith, S.J. Marsh, D. Dialetis, J. Mathew, P. Loschialpo, and J.H. Chang. <i>Physical Review Letters</i> 64, No. 20: 2374-77	8
Compact, high-current accelerators and their prospective applications. C.A. Kapetanakos, L.K. Len, T. Smith, D. Dialetis, S.J. Marsh, P. Loschialpo, J. Golden, J. Mathew, and J.H. Chang. <i>Phys. Fluids B</i> , August 1991: 2396-2402	12
Beam trapping in a modified betatron accelerator. C.A. Kapetanakos, D. Dialetis, S.J. Marsh, L.K. Len, and T. Smith. <i>Physical Review Letters</i> 44, No. 6: 3900-06.	19
Excitation of the $l = 12$ cyclotron resonance in the NRL modified betatron accelerator. L.K. Len, T. Smith, P. Loschialpo, J. Mathew, S.J. Marsh, D. Dialetis, J. Golden, J.H. Chang, and C.A. Kapetanakos. Paper presented at the Society of Photo-Optical Instrumentation Engineers Conference, 20-24 January 1992, Los Angeles, CA. <i>Intense Microwave and Particle Beams III</i> , SPIE Proceedings Vol. 1629, Bellingham, WA.. .	27
Dynamic behavior of an electron ring close to a cyclotron resonance in a modified betatron accelerator. D. Dialetis, S.J. Marsh, and C.A. Kapetanakos. <i>Physical Review Letters</i> 47, No. 3: 2043-60.	35

Beam Extraction Scheme from the Modified Betatron Accelerator

C. A. Kapetanakos, S. J. Marsh,^(a) and D. Dialetis^(b)

Plasma Physics Division, Naval Research Laboratory, Washington, D.C. 20375

(Received 10 March 1988)

A technique is proposed for extraction of the electron ring from the modified betatron accelerator. Basically, this technique consists of exciting the resonance that naturally exists for some specific values of the ratio of the vertical to toroidal magnetic field.

PACS numbers: 52.75.Di, 29.20.Fj, 41.80.Ee

The modified betatron accelerator^{1,2} is one among the several compact, high-current accelerator concepts currently under development in various laboratories. In this device a strong toroidal magnetic field B_θ has been added to the conventional betatron³ magnetic field configuration. Although B_θ substantially improves the stability of the conventional betatron, the beam injection and capture and the electron ring extraction after the completion of acceleration are substantially more involved as a result of the toroidal field.

In this Letter, we report on an extraction scheme that is easily realizable and has the potential to lead to very high extraction efficiency. Briefly, the proposed extraction scheme is based on the transformation of the circulating electron ring into a stationary helix, in the toroidal direction, by excitation of the resonance that naturally exists for some specific values of the ratio of the vertical to toroidal magnetic field. Transformation of the ring into a helix is achieved with a localized vertical magnetic field disturbance that is generated by an agitator coil. As the minor radius of the helix increases with each passage through the gap of the agitator coil, the electrons eventually reach the extractor, which has the property that all the magnetic field components transverse to its axis are equal to zero. Thus, the electron ring upwinds into a straight beam.

Although the proposed scheme is related to the standard techniques^{4,5} used for extraction of the beam from existing circular accelerators, several of its key features are different because of the presence of the toroidal magnetic field.

Extraction scheme.—After the completion of acceleration, i.e., when the desired electron beam energy has been achieved, the electron ring centroid is displaced radially by the intentional mismatch of the magnetic flux and the betatron magnetic field. In the results that will be shown in the next section, this mismatch has been achieved by superimposition of a low-amplitude vertical magnetic field that varies exponentially with time on the betatron field. It has been shown theoretically and verified by extensive numerical results that during the radial displacement of the ring centroid the amplitude of the slow mode¹ remains very small, i.e., a few millimeters, provided that the mismatching field varies slowly

with respect to the ring bounce (poloidal) period. Furthermore, computer simulations with the U.S. Naval Research Laboratory MOBE particle-in-cell computer code have shown that during the radial displacement, that lasts several microseconds, the minor cross section of the ring preserves its integrity and the ring emittance remains constant.

As the major radius of the ring centroid increases slowly with time, the gyrating electrons reach the localized magnetic disturbance generated by the agitator coil. At this radial position the ratio of the vertical magnetic field B_z to the toroidal magnetic field B_θ has been selected to satisfy the condition

$$B_z/B_\theta = 2l/(2l^2 - 1), \quad (1)$$

where $l = 1, 2, 3, \dots$

Equation (1) implies that the frequency of the fast mode¹ is l times the frequency of gyration around the major axis. When $B_\theta \gg B_z$, Eq. (1) is reduced to $\Omega_\theta = l\Omega_z$, where $\Omega_\theta = eB_\theta/m$ and $\Omega_z = eB_z/m$.

The purpose of the magnetic disturbance is to excite the resonance.^{6,7} As an electron enters the lower magnetic field region of the disturbance, its velocity vector, which initially is directed in the toroidal direction, rotates slightly in the radial direction, i.e., the electron obtains a radial velocity component. It can be shown from the equations of motion that this radial velocity is given by

$$\Delta v_r \approx -2(\Delta\Omega_z^2/\gamma)r_a\Delta\theta, \quad (2)$$

where $\Delta\Omega_z^2$ is the cyclotron frequency that corresponds to the field of the disturbance generated by the agitator coil, γ is the relativistic factor, r_a is the radial distance of the agitator coil, and $\Delta\theta$ is the toroidal half width of the magnetic disturbance.

As a result of the acquired radial velocity, the electrons start to gyrate in the toroidal magnetic field with a radius

$$\rho = 2(N/l)(\Delta\Omega_z^2/\Omega_z)r_a\Delta\theta, \quad (3)$$

where N is the number of passes through the disturbance. If condition (1) is not satisfied, ρ grows as $N^{1/2}$ instead of proportionally to N .

Since γ is very large, self-fields can be ignored. However, because of the gradient of B_z , the slow mode¹ (bounce motion) is still excited and the orbits of electrons in the transverse (r, z) plane precess very slowly. Therefore, for times short in comparison with the bounce period, i.e., for a few revolutions around the major axis, all the electrons of the ring perform coherent motion and a stationary helix, in the toroidal direction, is formed. A top view of the helix is shown in Fig. 1, for $l=3$.

Ideally, the radial gradient of the magnetic disturbance should be extremely high, because otherwise the fast mode¹ is excited before the ring reaches the disturbance. In the computer runs of the next section, a disturbance with a satisfactorily sharp radial gradient is obtained by the single-turn agitator coil shown in Fig. 2. The radial gradient of the disturbance is further improved with two single-turn loops that are located at the edges of the gap. In the computer runs, the magnetic field of the disturbance has been obtained from exact analytical expressions that are too long to be given here.

With successive passes through the disturbance of the agitator the radial excursion of the orbit increases until the gyrating electrons reach the extractor, which is located at $\theta=0$ and at a slightly greater radial distance than the agitator coil. The results of the next section were obtained with a simple extractor consisting of two parallel plates with current flowing in opposite directions. These two plates have infinite extent in the z and semi-infinite extent in the y directions. The linear current density of the plates is adjusted to make the total B_z between the plates at $\theta=0$ equal to zero. The side of the extractor at $\theta=0$ is completely enclosed. As a result the fringing fields are absent. The electrons enter the extractor through a thin conducting foil. At the entrance of the extractor the vertical displacement of the electrons and their radial velocity are almost zero. However, they have a small vertical velocity.

In practice, this extractor can be realized by bending the two plates to form a torus. In order for the field to be uniform over a finite vertical distance, the cross section of each plate, after bending, should be D shaped. In the results of the next section, the orbit of the extracted beam is terminated after it propagates tens of centimeters inside the extractor. The reason is that ΔB_z is independent of y while the betatron field decreases with y . Thus, cancellation of the fields is not achieved over the entire length of the extractor. In practice exact cancellation of the two fields can be obtained by an increase in the separation of the two plates as y increases.

In the previous discussions, we have assumed that the magnetic disturbance generated by the agitator coil is static. An alternative mode of operation is to expand the ring until it reaches the gap of the agitator coil and then to pulse the coil rapidly. Since the inductance of the agitator is typically only a few nanohenries, short rise times, of the order of a few nanoseconds, can be achieved with modest voltages. In the pulsed mode of operation the fraction of the ring that will be lost is approximately equal to the ratio of coil rise time to period of gyration around the major axis.

Finally, it should be noticed that an ion channel⁸ formed by a laser beam along the axis of the extractor may improve the extraction process and eliminate the need for an additional coil to cancel the component of B_z that is transverse to the axis of the extractor or the need to cancel completely the B_z inside the extractor.

Results.—We have studied the proposed extraction scheme in both the static and pulsed modes for a range of parameters that are compatible with the U.S. Naval Research Laboratory modified betatron accelerator. In this Letter, we present results from three runs: one in the pulsed mode for $\gamma=40$ and two in the static mode for $\gamma=40$ and 400. The various parameters of these three runs are listed in Table I. Since $\gamma \gg 1$, self-fields and im-

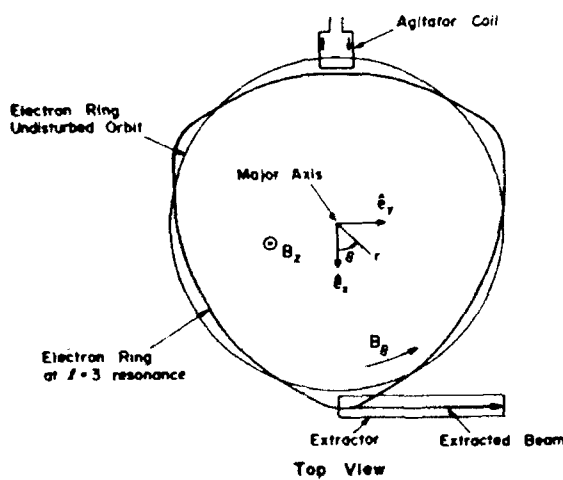


FIG. 1. Schematic of the proposed extraction scheme.

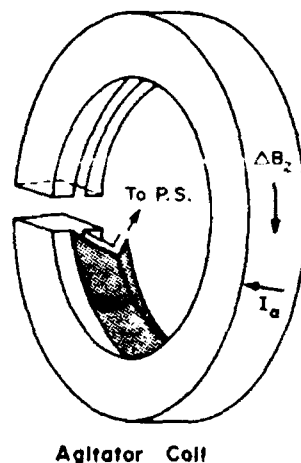


FIG. 2. Agitator coil that generates the localized disturbance. It is powered by a coaxial transmission line.

TABLE I. List of various parameters for the runs shown in Figs. 3 to 5.

Parameter	Run No.	267	266	268
Agitator's mode		Pulsed	Static	Static
Relativistic factor γ		40	40	400
Major radius r_0 (cm)		100	100	100
Vertical field at r_0 (G)		649.9	649.9	6501
Toroidal field at r_0 (G)		-1921	-1971	-19700
Field index n		0.5	0.5	0.5
Resonance integer l		3	3	3
Amplitude of mismatching field (G)		...	60	600
Time constant of mismatching field (μ sec)		...	10	10
Agitator				
Toroidal position		1.3π	1.26π	1.26π
Toroidal width $2\Delta\theta$ (rad)		0.05	0.066	0.066
Inner radius (cm)		120	120	120
Outer radius (cm)		122	124	124
Opening (cm)		1.0	2	2
Linear current density (kA/cm)		0.25	0.375	3.750
Field ΔB_z^0 (G)		-300	-450	-4500
Extractor				
Opening toroidal position		0	0	0
Minimum inner radius (cm)		121.5	120.5	120.5
Minimum outer radius (cm)		125.5	124.5	124.5
Field ΔB_z^0 (G)		-590.0	-590	-5900

age fields have been ignored and therefore the ring current is not a relevant parameter. Also at this high γ the beam minor diameter is expected to be only a few millimeters.

In run 267, the pulsed agitator was turned on after the ring's major radius became 121 cm. Figure 3(a) shows the radial excursion of a typical electron that was located at $\theta=0$ at the turning on of the agitator. After a single pass through the agitator the electron obtains enough radial excursion to enter the extractor and is extracted. Figure 3(b) shows that the electron at the disturbance obtains a transverse velocity approximately $2.8 \times 10^{-2} c$. Equation (2) predicts a $\Delta v = 2.7 \times 10^{-2} c$. In addition, the numerical results show that the electron gyrates around B_0 with a 1-cm radius, which is also the radius predicted by Eq. (3).

In run 266, the electron started at $r=110$ cm and was moved radially by the mismatching field. The elapsed time from the minor axis to the agitator is $\approx 4.5 \mu$ sec, that corresponds to an average radial velocity of $\approx 2.2 \times 10^6$ cm/sec. The amplitude of the slow mode is less than 2 mm. Figure 4(a) shows the radial excursions of a typical electron in the r, θ plane and Fig. 4(b) shows a top view of its orbit. The electrons reach the extractor with a vertical displacement from the midplane that is only a few millimeters. For the reason given in the previous section, the run was terminated after the electron propagated ≈ 30 cm inside the extractor.

In run 268, γ was increased to 400 with a corresponding increase in the value of magnetic fields. Figure 5(a)

shows the radial excursions of the electron and Fig. 5(b) is a top view of the orbit. The coherence of the radial excursions is remarkable. We have found that this coherence is preserved even when Eq. (1) is not satisfied

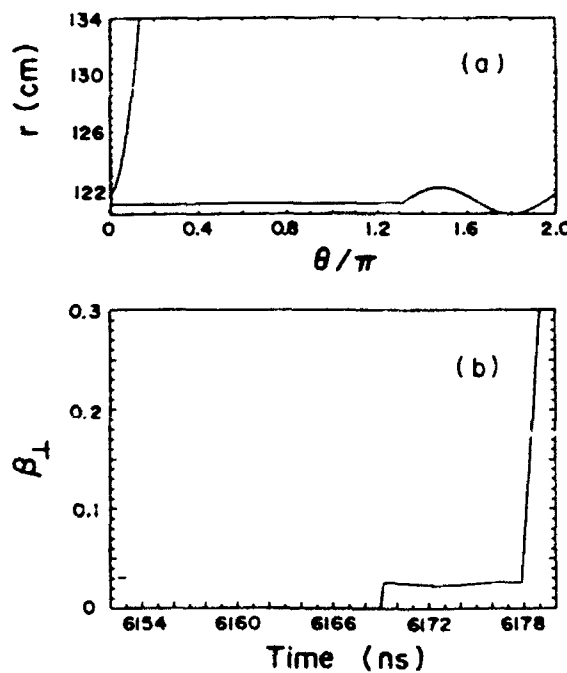


FIG. 3. (a) Radial excursions of a typical electron and (b) its corresponding normalized transverse velocity for the run 267.

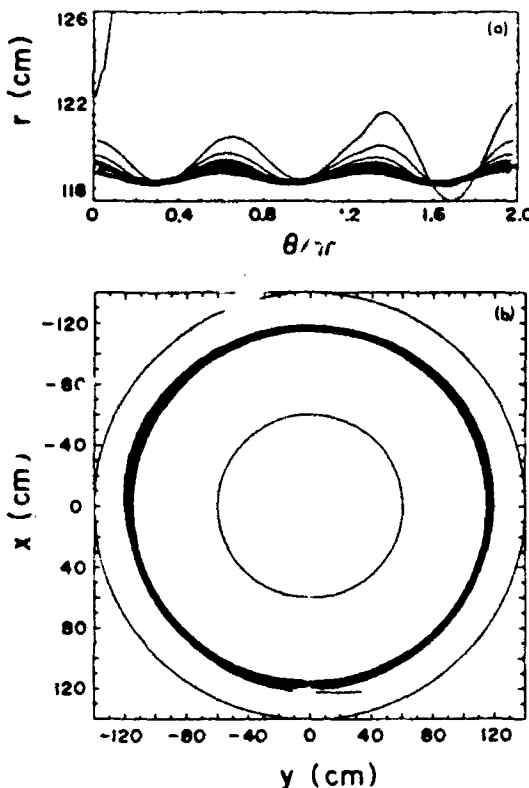


FIG. 4. (a) Radial excursions of a typical electron and (b) top view of its trajectory in the x , y plane for run 266.

exactly, i.e., when the value of field B_θ is off by tens of gauss. Finally, by operation at $l=1$ or 2 instead of at $l=3$, the value of B_θ can be substantially reduced.

Several successive runs with $\gamma=400$ electrons that are located at different positions on the minor cross section of a 3-mm-diam ring show that all these electrons arrive at the entrance of the extractor with less than 1 nsec time difference. In addition, the results show that although the vertical width of the ring has been slightly reduced, its corresponding radial width has been increased by approximately a factor of 3. This spread of the beam is probably associated with the slightly different value of ΔB , experienced by the different electrons as a result of the finite gradient of the agitator.

In conclusion, we have developed a new extraction scheme that is practical and has the potential, since all the electrons of the ring perform coherent motion, to lead to a very high extraction efficiency.

The authors are grateful to Professor D. Kerst and Dr. J. Golden, Dr. P. Sprangle, and Dr. R. Faehl for many illuminating discussions. This work was supported by the Space and Naval Warfare Systems Command and

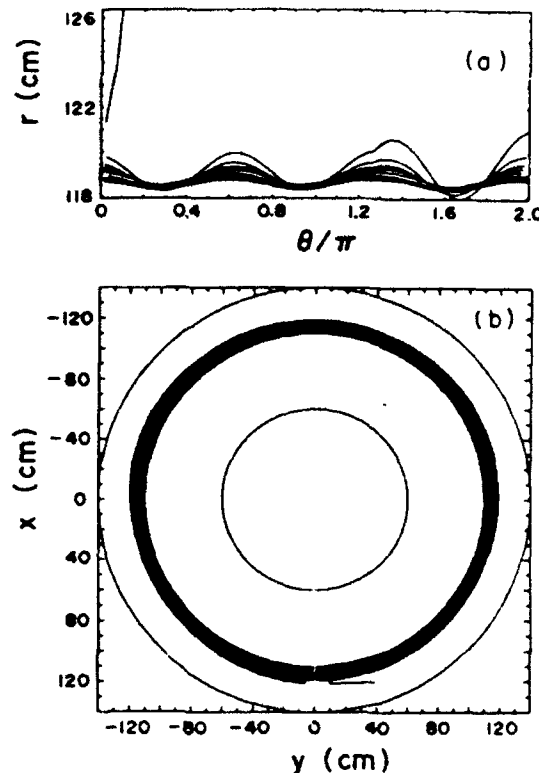


FIG. 5 (a) Radial excursion of a typical electron and (b) top view of its trajectory in the x , y plane for run 268.

the U.S. Office of Naval Research.

^(a)Permanent address: Sachs/Freeman Associates, Inc., Landover, MD 20785.

^(b)Permanent address: Science Applications, Inc., McLean, VA 22102.

¹C. A. Kapetanakos, P. Sprangle, D. P. Chernin, S. J. Marsh, and I. Haber, Phys. Fluids **26**, 1634 (1983).

²H. Ishizuka, G. Lindley, B. Mandelbaum, A. Fisher, and N. Rostoker, Phys. Rev. Lett. **53**, 266 (1984).

³D. W. Kerst, Nature (London) **157**, 90 (1940).

⁴L. C. Teng, in *Physics of High Energy Particle Accelerators*, edited by R. A. Carrigan, F. R. Huson, and M. Month, AIP Conference Proceedings No. 87 (American Institute of Physics, New York, 1982), p. 62.

⁵E. J. N. Wilson, in CERN Report No. 77-13, 1987 (unpublished), p. 111.

⁶D. Chernin and P. Sprangle, Part. Accel. **12**, 101 (1982).

⁷D. Dialetis, S. J. Marsh, and C. A. Kapetanakos, Part. Accel. **21**, 227 (1987).

⁸B. Hui and Y. Y. Lau, Phys. Rev. Lett. **53**, 2024 (1984).

Improved Beam Confinement in the Modified Betatron with Strong Focusing

C. A. Kapetanakos, L. K. Len,^(a) T. Smith, J. Golden,^(b) K. Smith,^(c) S. J. Marsh,^(c) D. Dialetis,^(d) J. Mathew, P. Loschialpo, and J. H. Chang

Plasma Physics Division, Naval Research Laboratory, Washington, D.C. 20375

(Received 16 January 1990)

The lifetime of the circulating electron beam in the Naval Research Laboratory modified betatron has been increased by more than 2 orders of magnitude with the addition of strong focusing windings to the device. The injected beam consistently spirals from the injector to the minor axis and is trapped. The -0.5 -kA trapped electron ring has been accelerated above 10 MeV from the injection energy of 0.5 to 0.6 MeV. The beam acceleration has been confirmed not only by the x-ray attenuation technique but also with the detection of photoneutrons.

PACS numbers: 41.80.Ee, 29.20.Fj

Accelerators that combine high-current capability and high effective accelerating gradient are currently under development in several laboratories.¹⁻⁵ These accelerators have two common features, namely, strong focusing that improves their current-carrying capability and recirculation that enhances their effective accelerating gradient.

Among these accelerators is the modified betatron.⁶⁻⁸ This device is currently under investigation at the University of California, Irvine² and also at the Naval Research Laboratory¹ (NRL). In its original form the modified betatron consists of a strong toroidal magnetic field and a time-varying betatron field that is responsible for the acceleration.

Extensive studies of beam capture and confinement in the NRL modified betatron led to the formation of electron rings with circulating current as high as 3 kA and have furnished valuable information on the critical physics issues of the concept. In addition, these studies have shown that over a wide range of parameters the ring lifetime was limited to a few microseconds which is comparable to the magnetic-field diffusion time through the vacuum chamber. Thus, it became apparent from these results that the magnetic-field configuration of the device had to be modified to increase the beam lifetime and thus to achieve acceleration. A decision was made to proceed rapidly with the design, fabrication, and installation of strong focusing windings.

Stellarator⁹ (four twisted windings that carry current in alternate directions) and Torsatron¹⁰ (two twisted windings that carry current in the same direction) winding configurations were considered. Both configurations have advantages and shortcomings. The stellarator configuration was finally selected not only because of the small net vertical field and the lower current per winding but also because it is compatible with our contemplated extraction scheme.^{11,12}

This paper briefly describes the NRL modified betatron in its latest form and summarizes the most impor-

tant experimental results after the installation of the strong focusing windings. Although experiments were carried out at various background pressures, most of the results reported in this paper were limited to pressures between 2×10^{-6} and 8×10^{-6} Torr. In this pressure range the electron-beam electrical neutralization time by direct collisional ionization of the background gas has been estimated to be between 180 and 45 μ sec. Work is in progress to reduce the background pressure by at least an order of magnitude and thus avoid substantial plasma formation over the entire beam lifetime. This is in contrast to the main effort in the Stellatron at Irvine² that is focused on the formation of runaway electron beams and therefore the pressure is incidentally high.

Description of the experiment.—(1) External magnetic fields: The NRL modified betatron comprises three different external magnetic fields; the betatron field that is a function of time and is responsible for the acceleration of the electrons, the toroidal magnetic field that varies only slightly during the acceleration of the electron ring, and the strong focusing field that also has a very weak time dependence. The coils that generate these three fields are shown schematically in Fig. 1.

(2) The betatron field: The betatron¹³ magnetic field controls mainly the major radius of the gyrating electron ring and is produced by eighteen air-core, circular coils connected in series. Their total inductance is approximately 530 μ H. The coils are powered by an 8.64-mF capacitor bank that can be charged up to 17 kV. At full charge, the bank delivers to the coils a peak current of about 45 kA. The current flowing through the coils produces a field that varies sinusoidally with time having a quarter period of 2.5 msec and an amplitude on the minor axis at peak charging voltage equal to 2.1 kG. Immediately after the peak the field is crowbarred with a 4.5-msec decay time.

The flux condition and field index are adjusted by two sets of trimmer coils that are connected in parallel to the main coils. The current through the trimmers is adjust-

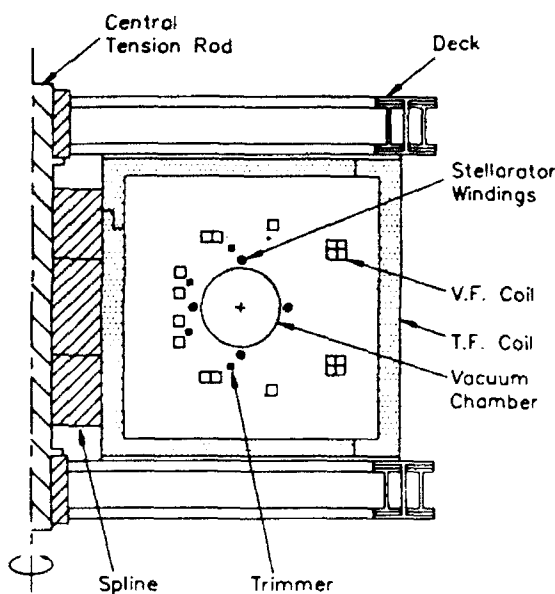


FIG. 1. Elevation of the device showing the vertical field (V.F.), toroidal field (T.F.), stellarator windings, and some structural components.

ed with series inductors. Typically $\sim 10\%-15\%$ of the total current flows through the trimmers.

(3) The toroidal field: The toroidal magnetic field controls mainly the minor cross section of the electron ring and the growth rate of several unstable collective modes. This field is generated by twelve air-core, rectangular coils that are connected in series.

The coils are made of aluminum square tubing and have a 150 cm height and 135 cm width. The total inductance of the twelve coils is $\sim 85 \mu\text{H}$ and are powered by a 24-mF capacitor bank that can be charged to a peak voltage of 10.6 kV. At peak voltage, the bank delivers to the coils $\sim 180 \text{ kA}$. This current produces a field that varies sinusoidally with time having a quarter period of 1.9 msec and an amplitude on the minor axis equal to 3.9 kG.

(4) The strong focusing field: The strong focusing field improves the confining properties of the other two fields by reducing the sensitivity of the beam centroid and individual electrons to energy mismatch and energy spread.

In the NRL modified betatron the strong focusing field is generated by four twisted windings carrying current in alternate directions. The left-handed windings are located 23.4 cm from the minor axis and have a 209.4-cm period, i.e., there are three periods over the circumference of the torus. They are supported by epoxy-reinforced graphite jackets and have been designed to carry up to 2.5 kA. The windings are connected in series and the current temporal profile is controlled by a ballast inductor.

The stellarator field index n_s is defined, in the linear

approximation, as¹⁰

$$n_s = -(\Omega_s^c \epsilon_s)^2 a r_0 / 2 \Omega_{z0} \Omega_{s0},$$

where

$$\Omega_s^c \epsilon_s \approx 4 a \Omega_0 \rho_0 K_2'(2 a \rho_0),$$

$\Omega_0 = |e| B_0 / m$, $B_0 = 2 \mu_0 I_s / L$, $a = 2\pi / L$, r_0 is the major radius, K_2' is the derivative of the modified Bessel function, and Ω_{z0} and Ω_{s0} are the cyclotron frequencies of the vertical and toroidal fields on the minor axis. Since in the NRL modified betatron I_s , Ω_{s0} , and Ω_{z0} / γ remain approximately constant during acceleration, n_s scales inversely proportional to the relativistic factor γ . The stellarator field index is related to the maximum gradient $g = -(\partial B_z / \partial r)_{\text{max}} = -(\partial B_z / \partial z)_{\text{max}}$ of the stellarator field by $n_s = -g^2 r_0 / 2 a B_{z0} \Omega_{s0}$. For $B_{s0} = 2.0 \text{ kG}$, $B_{z0} = 25 \text{ G}$, $a = 0.03/\text{cm}$, $\rho_0 = 23.42 \text{ cm}$, and $I_s = 19 \text{ kA}$, $n_s = 14$, and $g = 20 \text{ G/cm}$.

(5) The vacuum chamber and diode: The 100-cm major radius, 15.2-cm-inside minor radius vacuum chamber has been constructed using epoxy-reinforced carbon fibers. The desired conductivity is obtained by embedding a phosphor bronze screen inside the body of the graphite. The graphite is 2.5 mm thick and has a surface resistivity of $26.6 \text{ m}\Omega$ on a square. The screen has 250×250 wires per inch and is made of $40\text{-}\mu\text{m-diam}$ wire with an equivalent surface resistivity of $12.8 \text{ m}\Omega$ on a square. The calculated resistance for the entire vacuum chamber is $57 \text{ m}\Omega$. The measured dc resistance of the toroidal vacuum vessel is $68 \pm 2 \text{ m}\Omega$. The outside surface of the chamber is covered with a 6.3-mm-thick, epoxy-reinforced fiberglass layer.

This novel construction technique has several attractive features, including controllable resistivity and thus magnetic-field penetration time, high stiffness, and tensile strength, high-radiation resistance (up to 500 Mrad) and low-outgassing rate ($\sim 10^{-8} \text{ Torr/sec cm}^2$).

The electrons are emitted from a thin carbon disk mounted at one end of a 2.5-cm-diam cylindrical cathode stalk clad with molybdenum. The carbon disk is flush with the molybdenum cladding and faces the circular opening of the conical anode, that is located 8.7 cm from the minor axis of the toroidal chamber. To minimize the magnetic-field component transverse to the emitting surface of the cathode the core of the cathode stalk is made out of high $\sigma\mu$ ferromagnetic material. The unsaturated state of the ferromagnetic material is prolonged by a thin copper housing.

Experimental results.—During the first microsecond following injection, the beam transverse motion is studied by monitoring the light emitted from a 10- μm -thick polycarbonate foil that is stretched across the minor cross section of the vacuum chamber.¹ The foil is graphite coated on the upstream side to avoid electrostatic charging. Figure 2 shows two open-shutter photographs of the light emitted as the ring passes through the foil

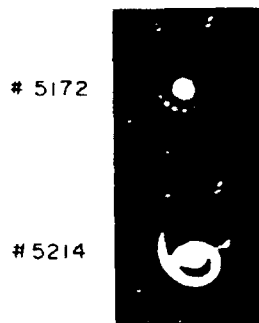
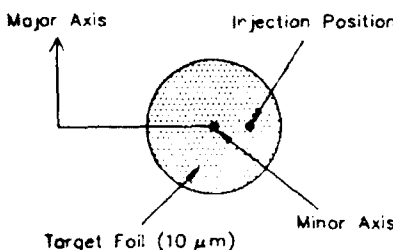


FIG. 2. Open-shutter photographs of the light emitted when the beam passes a 10- μm -thick foil.

The light spots near the edges of the photograph are position fiducials produced by a ring of light-emitting diodes located approximately 0.7 cm from the vacuum chamber wall. Reflections from the wall are also noticeable near the upper edge of the photograph.

For several combinations of injection parameters the beam consistently spirals from the injection position to the minor axis and is trapped. The transit time of the beam to the minor axis is typically less than 0.5 μsec . In shot No. 5172 both the beam current and B_θ are low and thus the bounce frequency is high. As the beam spirals from the diode to the minor axis it creates distinct light spots as it passes through the foil. By increasing the beam current and B_θ the bounce frequency is reduced and thus the light spots start to overlap and the spiral becomes continuous as in shot No. 5214.

The trapping mechanism is presently unknown. A likely candidate is the wall resistivity. However, the predicted decay rate Γ^{-1} from the linear theory¹⁴ for the parameters of the experiment is between 10 and 20 μsec , i.e., too long to explain the experimental results.

The circulating electron ring current is monitored with two Rogowski coils that are located inside the vacuum chamber. A typical wave form is shown in Fig. 3. Although some losses occur immediately after injection, the circulating current remains practically constant during the first 10 μsec . Observations are limited to 10 μsec by the signal level and the 100- μsec passive integrator. Attempts to use active integrators have been, so far, unsuccessful.

In the results reported here the injected electron beam is produced by a diode with a 1-cm-diam carbon cathode

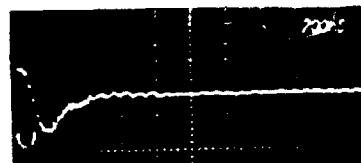


FIG. 3. Output from a Rogowski coil that is located 15° downstream of the diode. The plateau (trapped current) corresponds to 525 A.

disk that is matched to a 1-cm-diam anode hole. For such a beam radius the maximum trapped current is between 0.5 and 0.6 kA. The results indicate that the trapped current increases as the beam diameter increases. Experiments with larger radius beams are presently in progress.

The ring lifetime is inferred from the x rays produced when the beam strikes a 2.5-cm-wide, 1-mm-thick lead limiter. The x rays are monitored by a collimated x-ray detector (scintillator-photomultiplier tube) that is housed inside a lead box. In the results reported in this paper, the x rays enter the scintillator through a 1.94-cm-diam hole and the detector is located 10.8 m from the target. A typical wave form of the x-ray monitor is shown in Fig. 4. From the value of the B_θ field it can be easily computed that the main peak of the x-ray signal corresponds to a particle energy near 11.0 MeV. The energy of the electrons that are lost at a later time is obviously higher.

The x-ray signal is very reproducible in both amplitude and shape. For the first 200–300 μsec we do not observe any x rays. The time at which x rays are initially observed and the times the various signal peaks occur are directly proportional to B_θ and inversely proportional to dB_z/dt . In addition, the temporal occurrence of the

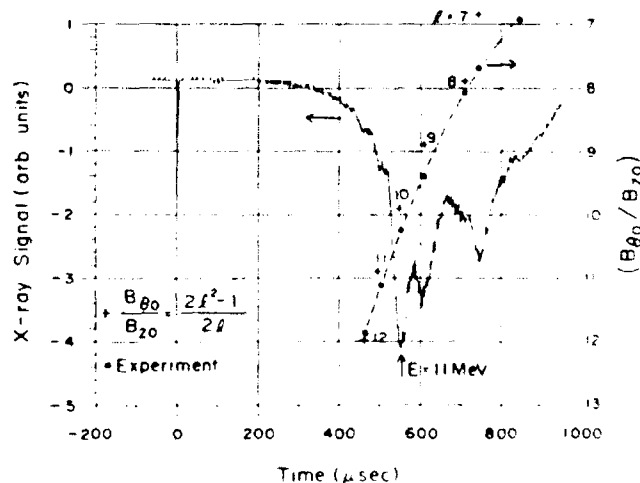


FIG. 4. Output of the x-ray detector vs time and $B_{\theta 0}/B_{20}$ at the peaks of the x-ray signal for $B_{\theta 0} = 3.6$ kG, $I_{SI} = 20$ kA, and $(B_z)/B_{\theta 0} = 1.9$.

x-ray signal appears to be independent of the trapped current for at least up to 0.5 kA and also of the background pressure up to 6×10^{-5} Torr. However, the amplitude of the x-ray signal decreases rapidly with increasing pressure above 8×10^{-6} Torr. For the results of Fig. 4, the electrons gain energy at the rate of 0.39 keV/revolution. Those electrons lost at the main x-ray peak have performed in excess of 28000 revolutions around the major axis. In our best results the corresponding number is ~ 35000 revolutions and the electron energy about 12 MeV.

The spiky shape of the x-ray signal and therefore the beam loss is consistent with the excitation of the cyclotron resonance.^{15,16} Figure 4 also shows the ratio B_θ/B_z versus time. The solid circles are from the experiment and the crosses are the prediction of the theory. The poor agreement between theory and experiment for low- l values is probably associated with the omission of toroidal effects in the theoretical model. The results are also consistent with the excitation of the electron-cyclotron instability.¹⁷ This instability is caused by the coupling of the electron-cyclotron mode to the TE_{11} waveguide mode of the torus. Work is in progress to pinpoint the exact cause of the beam loss.

The x-ray signal has been studied with the usual attenuation technique. A layer of lead more than 5 cm thick is needed to completely eliminate the signal. A 1.3-cm-thick layer does not have any effect on the signal except on the initial spike that is due to the injected beam. In addition to the x-ray attenuation technique, the beam acceleration has been confirmed with the photoneutrons produced from the $D(\gamma, n)H$ reaction. A plastic tube in the form of a ring containing heavy water was inserted behind the limiter. The photons produced on the target photodisintegrate the deuterium and produce neutrons that are monitored with a rhodium activation detector.¹⁸ The number of counts measured during the first minute exceeds 7 standard deviations.

The intensity and polarization of the synchrotron radiation has been computed numerically. At low energy (≤ 1 MeV) the radiation spectrum is dominated by a peak at the Doppler-shifted B_θ cyclotron frequency. As the electron energy increases the effect of the B_θ cyclotron motion is reduced and the spectrum approaches that of a purely circular orbit.

Two high-gain (50 db) heterodyne receivers are used to monitor the emitted radiation in the bands 26.5–28.5 and 36.5–38.5 GHz during acceleration. The measurements show that the amplitude of the radiation scales linearly with the trapped ring current. During the first 200 nsec, both the amplitude and polarization are consistent with the predicted single-particle emission. In addition, the temporal shift of the first peak is in good agreement with the predicted toroidal field and energy

dependence of the Doppler-shifted cyclotron frequency. However, the late-time behavior of the radiation signals is not presently well understood. The radiation signal starts to decay after ~ 200 μ sec, contrary to the prediction of the theory. It is likely that electron losses, plasma formation, or beam displacement out of the field of view of the detectors are responsible for the observed discrepancy.

The authors are grateful to Professor D. Kerst, Dr. P. Sprangle, and Dr. Y. H. Seo for many illuminating discussions. This work was supported by the ONR and the Space and Naval Warfare Systems Command.

Note added.—Since the submission of the paper, the trapped current increased to 0.9–1.0 kA and the beam energy to 15–16 MeV.

^(a)Permanent address: FM Technologies, Inc., 10529-B Braddock Road, Fairfax, VA 22032.

^(b)Permanent address: Berkeley Research Associates, 5532 Hempstead Way, Springfield, VA 22151.

^(c)Permanent address: Sachs/Freeman Associates, Inc., Landover, MD 20785.

^(d)Permanent address: Science Applications, Inc., 1710 Goodridge Drive, McLean, VA 22102.

¹J. Golden *et al.*, in *Proceedings of the Seventh International Conference on High-Power Particle Beams, Karlsruhe, Germany, July 1988*, edited by W. Bauer and W. Schmidt (Kernforschungszentrum Karlsruhe GmbH, Karlsruhe, 1988), Vol. I, p. 221.

²H. Ishizuka *et al.*, in *Proceedings of the Seventh International Conference on High-Power Particle Beams* (Ref. 1), Vol. II, p. 857.

³S. Humphries, Jr., and L. K. Len, in *Proceedings of the 1987 Particle Accelerator Conference, Washington, DC, March 1987*, edited by E. R. Lindstrom and L. S. Taylor (IEEE, New York, 1987), p. 914.

⁴V. Bailey *et al.*, in *Proceedings of the 1987 Particle Accelerator Conference* (Ref. 3), p. 920.

⁵W. K. Tucker *et al.*, in *Proceedings of the 1987 Particle Accelerator Conference* (Ref. 3), p. 957.

⁶P. Sprangle and C. A. Kapetanakos, *J. Appl. Phys.* **49**, 1 (1978).

⁷C. A. Kapetanakos *et al.*, *Phys. Fluids* **26**, 1634 (1983).

⁸N. Rostoker, *Comments Plasma Phys.* **6**, 91 (1980).

⁹C. Roberson *et al.*, *Phys. Rev. Lett.* **50**, 507 (1983).

¹⁰C. A. Kapetanakos *et al.*, *Part. Accel.* **21**, 1 (1987).

¹¹C. A. Kapetanakos *et al.*, *Phys. Rev. Lett.* **61**, 86 (1987).

¹²S. J. Marsh *et al.*, *J. Appl. Phys.* **64**, 6138 (1988).

¹³D. W. Kerst, *Nature (London)* **157**, 90 (1946).

¹⁴P. Sprangle and C. A. Kapetanakos, *Part. Accel.* **18**, 203 (1986).

¹⁵D. Chernin and P. Sprangle, *Part. Accel.* **12**, 101 (1982).

¹⁶C. W. Roberson *et al.*, *Part. Accel.* **17**, 79 (1985).

¹⁷P. Sprangle (private communication).

¹⁸F. C. Young, *IEEE Trans. Nucl. Sci.* **22**, 718 (1975).

Compact, high-current accelerators and their prospective applications*

C. A. Kapetanakos,[†] L. K. Len,[‡] T. Smith, D. Dialetis,[§] S. J. Marsh,^{||} P. Loschialpo,

J. Golden,[¶] J. Mathew, and J. H. Chang

Plasma Physics Division, Naval Research Laboratory, Washington, DC 20375-5000

(Received 5 December 1990; accepted 1 April 1991)

This paper briefly surveys the three compact, high-current accelerators that are presently under development in the United States in support of a national program. In addition, it reports recent experimental results from the Naval Research Laboratory (NRL) modified betatron [Phys. Rev. Lett. **64**, 2374 (1990)] with emphasis on the electron-cyclotron resonance that presently limits the energy of the beam to approximately 18 MeV. Finally, it briefly addresses selective existing and prospective applications of accelerators.

I. INTRODUCTION

Over the last 60 years the technology of high-energy accelerators has advanced to a remarkable level of sophistication.¹ These conventional accelerators are designed to operate reliably at high energies but at relatively low current, primarily to avoid complications related to beam self-field effects. Thus the beam dynamics in conventional accelerators is determined mainly by the externally applied fields.

Over the last several years, it has become apparent that accelerators with both high current and high-average power could have interesting applications not only in national defense² but also in several areas of the civilian economy.¹

In contrast with the conventional accelerators that operate in the single-particle regime, high-current accelerators operate in an uncharted territory, in which space charge effects from the self and image fields are as important as externally applied fields. The free energy stored in the intense self fields of these beams can drive collective instabilities and strong magnetic fields are needed to reduce the rapid growth rate of these unstable modes. Several of the key physics issues associated with the high-current accelerators are similar to those in plasma physics. Therefore it is not accidental that the majority of researchers that are presently developing this technology have been trained in plasma physics and not in conventional accelerator technology.

Compact, high-current accelerators are currently under development in several laboratories.³⁻⁷ As a result of their compactness and light weight, these devices are expected to be substantially less costly than conventional accelerators of comparable power. In addition, because of their high-current carrying capability, these accelerators have the potential to generate very powerful electron beams that can provide high dose rates at reduced unit irradiation cost.

During the last several years several applications have

been suggested,^{1,8} such as water purification, sludge disinfection, cracking of crude oil, and excavation of tunnels, all requiring high-average power and low unit irradiation cost. These applications are presently on hold waiting for the development of inexpensive beams.

In this paper, we briefly survey the three compact accelerators that are currently under development in support of the DARPA/services program and report recent experimental results from the NRL modified betatron. The last section briefly addresses existing and prospective applications of accelerators.

II. REVIEW OF COMPACT, HIGH-CURRENT ACCELERATORS

Compact, high-current accelerators are currently under development at the University of California, Irvine,⁴ University of New Mexico,⁵ Pulse Sciences Inc.⁶ (PSI), Sandia National Laboratory⁷ (SNL), and the Naval Research Laboratory³ (NRL). All these concepts are induction accelerators. The reason is that induction accelerators are inherently low-impedance devices and thus are ideally suited to drive high-current beams. The acceleration process is based on the electric field produced by a time-varying magnetic field. The electric field can be either continuous or localized along the accelerating path.

This section briefly reviews the three electron acceleration concepts that are part of the national program: The spiral line induction accelerator (SLIA) developed at PSI, the recirculating linear accelerator (RLA) developed at SNL, and the modified betatron accelerator (MBA) developed at NRL. In addition to being inductive, these three accelerators utilize strong focusing in order to improve their current carrying capability and recirculation to enhance their accelerating gradient.

A. Spiral line induction accelerator⁶

The SLIA concept is shown schematically in Fig. 1(a). The beam is injected at one end of the spiral line and is accelerated at the advanced test accelerator (ATA) type accelerating cells. The minor radius of the beam is controlled by an axial magnetic field and the beam is guided at the bends by a static vertical and strong focusing field. At the exit, the beam

*Paper 116, Bull. Am. Phys. Soc. **35**, 1919 (1990).

[†]Invited speaker.

[‡]Permanent address: FM Technologies, Inc., 10529-B Braddock Road, Fairfax, Virginia 22032.

[§]Permanent address: Science Applications, Inc., 170 Goodridge Drive, McLean, Virginia 22102.

^{||}Permanent address: SFA, Inc., Landover, Maryland 20785.

[¶]Permanent address: Berkeley Research Associates, 5532 Hampstead Way, Springfield, Virginia 22151.

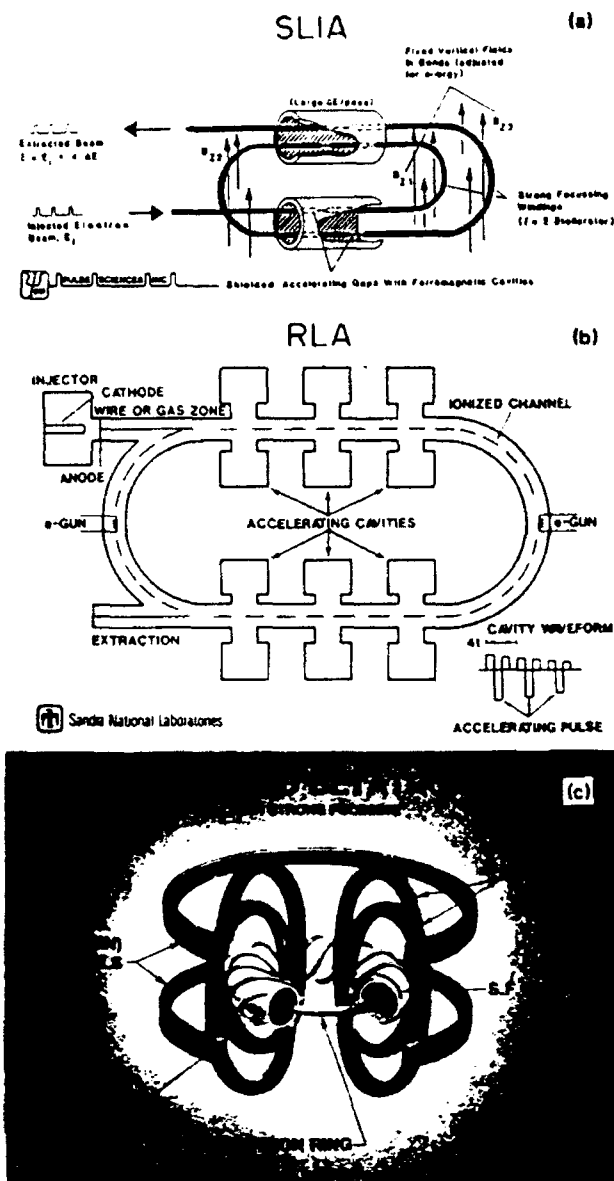


FIG. 1. Schematics of the three compact, high-current accelerators presently under development in support of the national compact accelerator development program

energy is equal to the injection energy plus the energy gain per pass times the number of passes.

Since the SLIA is open-ended, difficulties associated with injection and extraction are avoided. Furthermore, this configuration provides flexibility in the selection of shape of the electron pulses. Important outstanding technical issues associated with the SLIA concept are the excitation of the beam breakup instability (BBU), the matching of fields between the straight sections and the bends, and the development of high-frequency power supply for driving and resetting the ferromagnetic cores.

A proof-of-concept (POC) experiment is presently under design and construction. Its most important parameters are listed in Table I. The 3.5 MeV, 10 kA, 35 nsec duration injected beam pulse will be accelerated to 9.5 MeV by passing twice through the two, 1.5 MeV accelerating units.

B. Recirculating linear accelerator⁷

The RLA is shown schematically in Fig. 1(b). The injected beam is accelerated by dielectric cavities that are placed in tandem along the straight sections of the race track. Beam focusing is provided by an ion channel formed by a low-energy, low-current electron beam. A time-rising vertical magnetic field guides the beam at the bends.

Important advantages of RLA concept are the suppression of BBU and the wide energy bandwidth provided by the ion channel. In addition to injection and extraction, maintaining the integrity and centering of the ion channel during acceleration and avoiding beam erosion are key technical issues.

A POC experiment is currently under construction. Its most important parameters are listed in Table I. The 3.5 MeV, 10 kA, 40 nsec duration electron beam pulse will be accelerated to 8–10 MeV by passing three times through the two, 1 MeV dielectric cavities.

C. The modified betatron accelerator^{9–11}

In both the SLIA and the RLA, the accelerating electric field is localized at the gaps. In contrast, the electric field in the MBA is continuous along the entire beam path and thus

TABLE I. Parameters of proof-of-concept (POC) experiments

SLIA	RLA	MBA
Injected beam	Injected beam	Injected beam
Energy ~ 3.5 MeV	Energy 3.5 MeV	Energy 0.6–0.7 MeV
Current ~ 10 kA	Current 10 kA	Current < 2 kA
Duration ~ 35 nsec	Duration 40 nsec	Duration ~ 40 nsec
Axial mag. field 5.5 kG		Torus major radius 100 cm
Vert. mag. field < 0.32 kG		Torus minor radius 15 cm
S.F. gradient < 0.25 kG/cm	Channel radius 1.5 cm	Toroidal mag. field 2–5 kG
No. of passes 2	Channel density/beam density 0.4	Vertical mag. field B_z 0–2 kG
No. of acc. units 2	No. of passes 3	Current in S.F. windings 20–25 kA
Energy gain/acc. unit 1.5 MeV	No. of cavities 2	No. of S.F. field periods 6
	Energy gain/cavity 1 MeV	$dB_z/dt \leq 1.5 \text{ G}/\mu\text{sec}$

the accelerator is constrained to circular shape. An artist's conception of the MBA is shown in Fig. 1(c). The injected beam is accelerated by the time-varying vertical (betatron) magnetic field B_z . The toroidal magnetic field B_θ controls mainly the minor radius of the beam and the growth rate of the various unstable modes while the vertical and strong focusing fields control mainly the major radius of the electron ring. The stability properties of the stellarator windings for high-current beams were studied initially by Gluckstern¹² in linear geometry and by Roberson¹³ *et al.* in toroidal geometry.

Important advantages of the MBA are the natural synchronization of B_z and particle energy, the absence of the BBU mode and its compact size and light weight. Outstanding technical issues are the suppression of the cyclotron resonances, collective instabilities, and the extraction of the beam.

A POC experiment is currently in operation at NRL. The various parameters of the device are listed in Table I. Its objective is to study the critical physics issues associated with the concept and to accelerate at 1 kA, 20 nsec electron beam pulse to 20 MeV with subsequent extraction of the beam.¹⁴ Presently, the trapped electron beam has been accelerated to between 17–18 MeV from the injected energy of 0.6–0.7 MeV. The maximum trapped current is up to 1.5 kA and the trapping efficiency is as high as 75%.

III. RECENT EXPERIMENTAL RESULTS FROM THE MBA

The NRL modified betatron accelerator has been described previously^{1,15,16} and a summary of the initial experimental results has been published.^{1,16} In this paper, we summarize the highlights of the most recent results.

During the first microsecond following injection, the beam motion is inferred from the light emitted when the electrons pass through a thin (3 μm) plastic foil stretched across the minor cross section of the vacuum chamber. The open shutter photographs show that for a wide range of experimental parameters and after fine tuning the fields, the injected beam consistently spirals from the injector to the vicinity of the minor axis and is trapped. The beam travel time from the injector to the minor axis depends on the values of the various fields and is typically between 300–1000 nsec.

The trapping of the beam is most likely due to the wall resistivity of the vacuum chamber. The physical mechanism of the resistive trapping can be understood as follows. Consider a pencil-like electron beam inside a cylindrical pipe with finite resistivity wall. Because of the resistivity of the wall, the electric and magnetic images do not coincide and thus the centroid of an off-axis beam experiences a negative radial magnetic field component. This field component crossed with the axial velocity of the beam produces a poloidal force, which is in the opposite direction to the poloidal motion of the beam. In the absence of the strong focusing and when the self-fields dominate the external fields (high-current regime), the poloidal force in conjunction with the axial (toroidal) magnetic field drives the beam to the wall (drag instability). However, in the presence of strong focus-

ing, the direction of the poloidal motion can be reversed and the beam spirals to the minor axis.

The resistive wall trapping mechanism has been analyzed previously.¹⁷ The linear theory was done for a beam near the minor axis. In this case, the relevant diffusion time is $\tau_1 \approx \mu_0 a / 2\rho$, where a is the minor radius of the torus and ρ its surface resistivity. For the parameters of the NRL-MBA, $\tau_1 \approx 10 \mu\text{sec}$. The linear decay rate Γ^{-1} from the theory is between 10–15 μsec , as expected. This time is at least a factor of 30 too long to explain the results.

In contrast to the analysis that assumes the beam is near the minor axis, the beam in the experiment during injection is near the wall and therefore the relevant diffusion time is $\tau_2 = \mu_0 \Delta / \pi^2 \rho$, where Δ is the thickness of the wall. The ratio $\tau_1 / \tau_2 = \pi^2 a / \Delta = 300$. The fact that τ_2 is substantially shorter than the observed trapping time is not surprising since the beam remains near the wall only for a short period of time. Experiments are presently under way to test the hypothesis of the resistive trapping.

The x rays are monitored by three collimated x-ray detectors (scintillator-photomultiplier tube) that are housed inside lead boxes. In the results shown in Fig. 2, the x rays enter the scintillator through a 1.94 cm diam tube and the detector is located 10.8 m from the vacuum chamber. As a rule, the shape of the x-ray signal recorded by all three detectors is spiky and the peaks always occur at the same value of $B_{\theta 0} / B_{z0}$ ($B_{\theta 0}$ is the toroidal and B_{z0} the vertical magnetic fields on the minor axis) independently of the current flowing in the stellarator windings.

In addition to the x-ray pulse, Fig. 2 shows the ratio of $B_{\theta 0} / B_{z0}$ at the peaks of the signal. The solid circles are from the experiment and the crosses are from the resonance condition $B_{\theta 0} / B_{z0} = (2l^2 - 1) / 2l$, $l = 1, 2, \dots$, of the cyclotron resonance.^{18,19} The solid line shows the trend of the experimental results with time. For $l = 8, 9$, and 10 , experiment and theory are in good agreement. However, for the remaining l values there is noticeable divergence between the theoretical predictions and the experiment.

The theory of the cyclotron resonance has been developed under the assumption that the beam is located on the

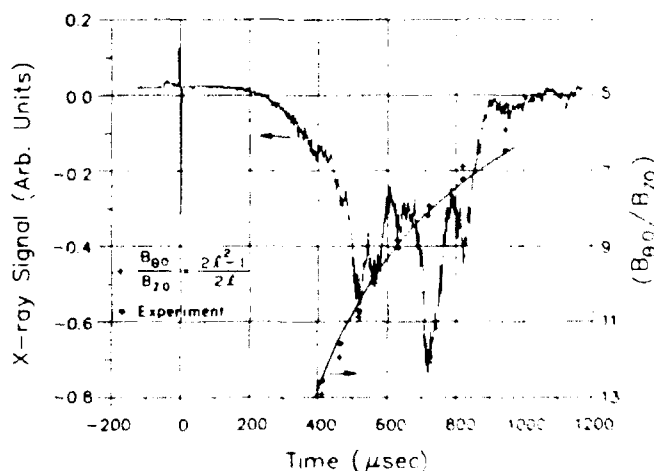


FIG. 2. X-ray pulse and ratio of $B_{\theta 0} / B_{z0}$ at the peaks of the x-ray signal. The main peak corresponds to 17.2 MeV.

minor axis. However, the experimental observations indicate that the electron ring starts to move off axis after 200–300 μ sec. Recently, the theory of the cyclotron resonance has been extended to a beam that is located on the midplane but off the minor axis. For such a beam the resonance conditions becomes

$$r_0 \Omega_{\theta 0} / c \gamma \beta_\theta = (2l^2 - 1) / 2l, \quad (1)$$

where r_0 is the major radius, $\Omega_{\theta 0}$ is the cyclotron frequency of the toroidal field, γ is the relativistic factor, and β_θ is the normalized toroidal velocity. Perfect match between the experimental results and the revised theory is obtained if it is assumed that the equilibrium position of the beam moves initially toward the major axis and then away from it with a constant outward radial speed of 0.23 mm/ μ sec, starting at about 460 μ sec.

In a modified betatron with strong focusing windings, there are four characteristic transverse modes¹³ $\omega_{\pm\pm}$. Integer resonances occur when the frequency of these modes, in the laboratory frame, over the relativistic cyclotron frequency of the vertical field Ω_{z0}/γ on the minor axis is an integer, i.e., when

$$\omega_{\pm\pm} / (\Omega_{z0}/\gamma) = K, \quad \text{where } K = \pm 1, \pm 2, \dots$$

The cyclotron resonance occurs when $\omega_{\pm\pm} / (\Omega_{z0}/\gamma) = K$, and, for the parameters of the NRL modified betatron listed in Table II, the cyclotron resonances are shown in Fig. 3. It is apparent from this figure that as the beam energy increases, the beam centroid crosses progressively lower-integer number resonances.

In the general case, the expressions for the four characteristic modes $\omega_{\pm\pm}$ are very complicated. However, for modest beam and strong focusing winding currents, as those found in the NRL device, the modes are considerably simplified. Under these conditions, $\omega_{\pm\pm} \approx -\Omega_{\theta 0}/\gamma$, where m is the number of field periods. In addition, when $B_{\theta 0} \gg B_{z0}$, the resonance condition takes the very simple form $B_{\theta 0}/B_{z0} \approx l$, where $l = 1, 2, \dots$. Therefore the cyclotron resonance is due to the coupling, caused by a field error(s), of the cyclotron motions associated with the toroidal and vertical fields.

The physical mechanism of the cyclotron resonance can be easily understood with the help of Fig. 4. Consider an electron rotating in a uniform vertical field B_z in the presence of a toroidal field B_θ . When this electron is at its equilibrium position, its orbit is a circle, centered around the major axis, and the velocity vector is tangential to the circular or-

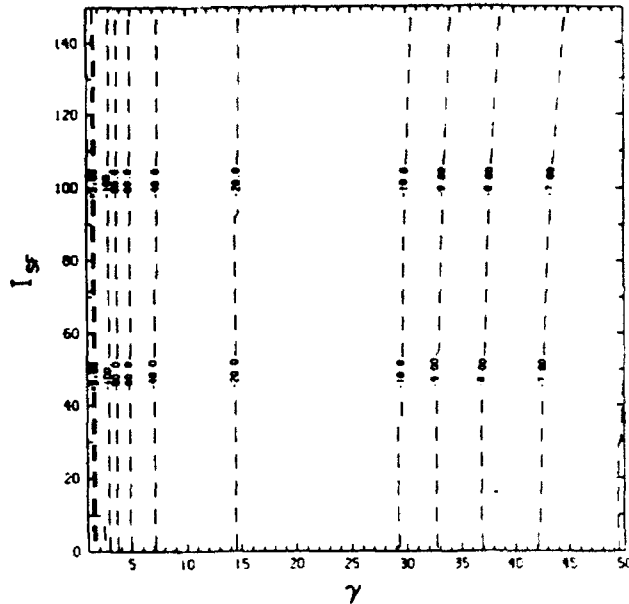


FIG. 3. Beam centroid integer cyclotron resonances for the parameters listed in Table II.

bit. Now, let us assume that a negative vertical field disturbance ΔB_z is introduced at a short segment of the orbit with toroidal half-width $\Delta\theta$. As the electron crosses the disturbance, it sees a reduced B_z and tries to acquire a larger radius. Thus, its velocity vector rotates clockwise and the electron develops a radial velocity component. As a result, the electron starts to rotate around B_θ and its orbit is transformed from a circle into a helix. When the resonance condition is satisfied, the electron will return to the disturbance on phase and it will acquire additional radial velocity and the radius of the helix will further increase.

The combined motion of the electron around B_z and B_θ is very similar to the motion of the Earth around the Sun and its axis. Fortunately, the time it takes the Earth to orbit the Sun (1 yr) over the time it takes the Earth to spin around its axis (1 day) is 365.242 199, i.e., is not an integer. By select-

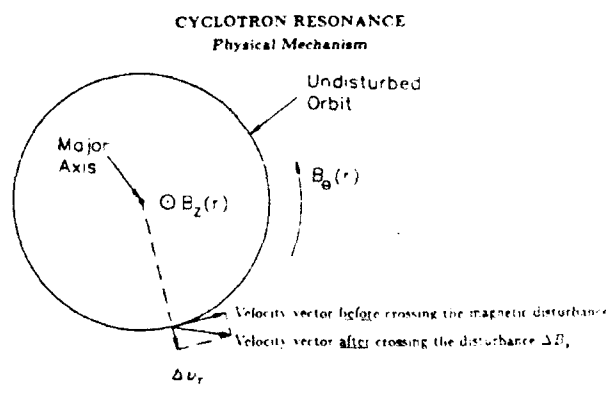


FIG. 4. Physical mechanism of the cyclotron resonance. The disturbance is located at approximately 5 o'clock at radius r_0 .

TABLE II Parameters used in the computation of cyclotron modes shown in Fig. 3.

Toroidal magnetic field B_θ	5 kG
Beam current	1 kA
Torus major radius	100 cm
Torus minor radius	15 cm
Beam minor radius	1 cm
S.F. field periods	6

ing the ratio year/day \neq integer, nature has avoided the excitation of a resonance from gravitational disturbances. As a consequence of this selection, the calendar had to be reformed three times (Caesar, Augustus, Pope Gregory XIII) over the last 2000 years. However, this is a rather small price to pay.

Since the initial observation of the cyclotron resonance in the NRL device, we have uncovered several field disturbances. By correcting these field deficiencies, a substantial increase in the beam lifetime has been observed with subsequent increase in the beam energy. One of the most important field errors was caused by the ports of the vacuum chamber. The ports disturb the flow pattern of the current induced by the rising B_z and create magnetic dipole-type field errors. The measured field errors from the ports and their Fourier modes are shown in Figs. 5(a) and 5(b), respectively. Figures 5(c) and 5(e) show the normalized transverse velocity components and 5(d) shows the normalized toroidal velocity as a function of time from the numerical solution of orbit equations. It is apparent that both transverse velocity components increase at the expense of the toroidal velocity as the beam crosses the $l = 10$ and 9 resonances.

It has been suggested that the beam loss in the modified betatron may be caused by the excitation of the cyclotron instability²⁰ instead of the cyclotron resonance. This instability results from the coupling of the cyclotron mode to the TE_{11p} modes of the toroidal chamber and is characterized by the resonance condition $[B_{\theta 0}/B_{z0} = (x_{\parallel}^2 r_0^2/a^2 + p^2)^{1/2} - p\beta_{\theta}]$, where $x_{\parallel} = 1.841$ and p is an integer. Figure 6 shows the cavity modes ω_{11p} and the cyclotron mode ω for several values of $\Omega_{\theta 0}/\Omega_{z0}$. The parameter

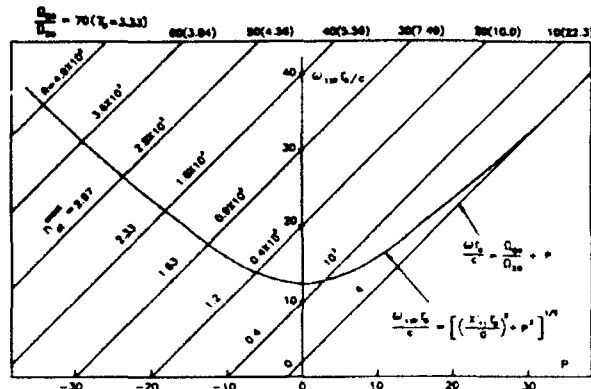


FIG. 6. TE_{11p} modes of the toroidal chamber and cyclotron mode. The cyclotron mode moves from left to right as the vertical magnetic field B_z rises while the toroidal magnetic field remains practically constant.

$R = -(r_0/c\Omega_{\theta 0})(d\omega/dt)/(d\Omega_{\theta 0}/dt)$ is the normalized time rate of the cyclotron mode caused by the rising B_z field. The parameter n_{st}^{exact} is the exact stellarator field index.¹³ Strong interaction is expected when the cyclotron mode crosses the cavity modes near cutoff because both R and n_{st}^{exact} are small.

To determine the importance of the cyclotron instability, an attempt was made to measure both the poloidal B_{ϕ}^{cl} and toroidal B_{θ}^{cl} magnetic field components of the electromagnetic modes inside the toroidal chamber using a fast, broadband B probe. The results of these measurements indicate that the peak of B_{θ}^{cl} is less than 3×10^{-5} G near cutoff

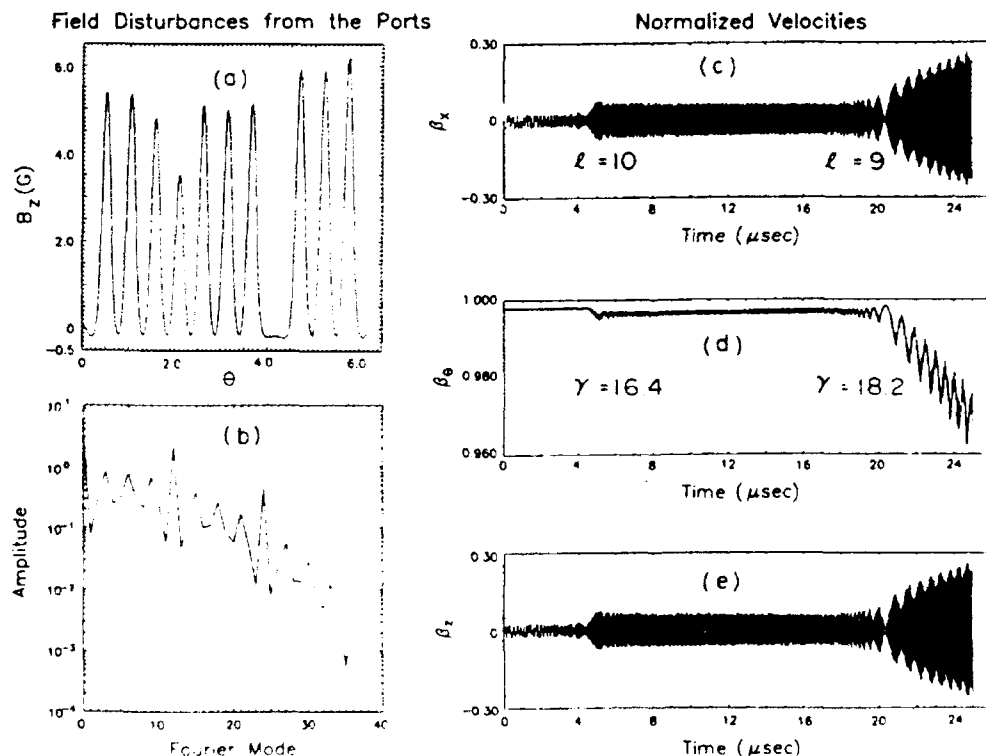
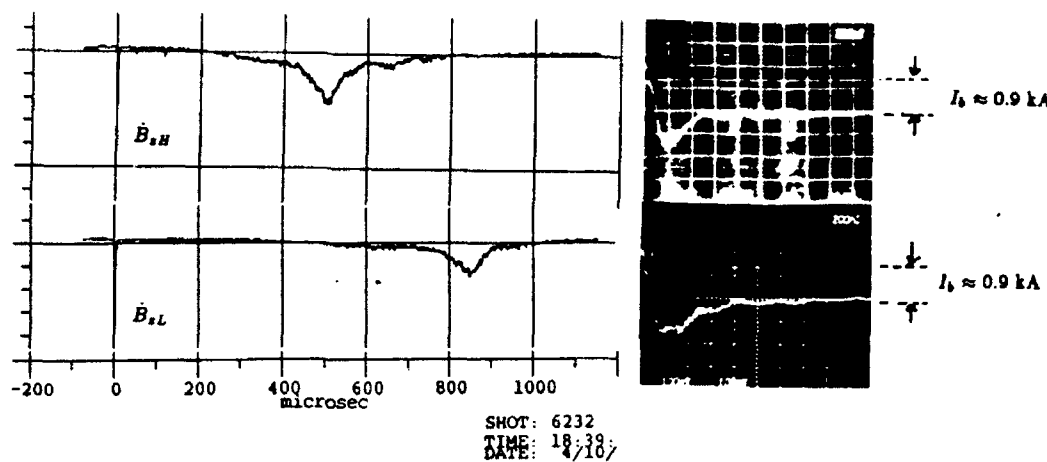


FIG. 5. Crossing of $l = 10$ and 9 cyclotron resonance during acceleration. (a) Measured field disturbances from the ports of the vacuum chamber. (b) Fourier modes of the disturbances. (c) and (e) normalized transverse velocity, and (d) normalized toroidal velocity versus time.



$$(\dot{B}_{zH}/\dot{B}_{zL}) = 1.82$$

$$B_{z0} = 3.8 \text{ kG}$$

$$I_{SF} = 21 \text{ kA}$$

FIG. 7. Two x-ray signals taken under identical conditions except for the time rate of the vertical field B_z . The electron ring lifetime varies approximately inverse proportionally to B_z .

(580 MHz), i.e., the amplitude of the electromagnetic modes inside the torus is negligibly small. Since the B_z^{c} required to excite the cyclotron instability is between 3–10 G, it is very unlikely that the beam loss is due to the cyclotron instability. In addition, the absence of electromagnetic modes with appreciable amplitude inside the toroidal cavity precludes the parametric instability²¹ as a serious beam loss mechanism.

The hypothesis that the beam loss is due to the cyclotron resonance is also supported by the fact that for a fixed toroidal magnetic field, the ring lifetime varies approximately inverse proportionally to the time rate of the vertical magnetic field dB_z/dt . Figure 7 shows the x-ray pulses for two shots with identical parameters, including the beam-trapped current, except for dB_z/dt . By reducing dB_z/dt by a factor of 1.82, the beam lifetime increased by approximately the same amount.

IV. EXISTING AND POTENTIAL APPLICATIONS OF ACCELERATORS

Table III lists selective existing and potential applications of accelerators. The first column shows the application, the second the dose or dose rate, and the third the desired average power. The required dose varies from a fraction of a Gy for radiation therapy to ~1 MGy for cracking of crude oil, i.e., it spans approximately seven orders of magnitude. With the exception of the last application listed in Table III, the rest of them have already been discussed in the scientific literature.^{1,2,22}

The radiation-induced cross-linkage of polymers is probably the most important industrial application of accel-

erators today and is used extensively by several companies both in the U.S. and abroad. For example, the Cryovac Division of W. R. Grace utilizes in excess of 40 electron accelerators with an aggregate beam power in excess of 1 MW. The annual value of irradiated products is ~\$800 M. Raychem

TABLE III. Application of accelerators.

Application	Dose or dose rate	Desired average power ^a
(1) Radiation therapy	0.25–1.4 Gy/min	VL
(2) Sterilization		
Pharmaceuticals	20–30 kGy	H
Human transplants	10–20 kGy	L
Musical instruments	10 kGy	L
Potable water	1 kGy	H
(3) Radiative processing		
Sludge disinfection	4–10 kGy	H
Food preservation	1.0–25 kGy	H
Cellulose depolymerization	5–10 kGy	H
Graft copolymerization	10–20 kGy	H
Curing of coatings	20–50 kGy	M
Vulcanization of silicones	50–150 kGy	H
Cross-linkage of polymers	100–300 kGy	H
Vulcanization of rubber	100–300 kGy	H
Flue-gas clean up	20–30 kGy	H
Cracking of crude oil	1000 kGy	H
Radiography	10–100 Gy/min	M
Excavation of tunnels	100–200 kGy	VH
Burning of nuclear wastes		VH

^a VH > tens of MW, H = several hundred kW, M = 10–100 kW, L ~ kW, VL < kW.

Corporation utilizes more than 20 accelerators in the energy range 0.3–10 MeV. The annual value of the irradiated products is ~\$1000 M. Accelerators are also used extensively by Western Electric to irradiate telephone wires. However, the company is unwilling to release any information related to this activity.

Recently, accelerators have been utilized to induce curing of composites.²³ These fiber-reinforced polymers²⁴ are presently used in several applications, including aircraft frames and wings, automobile bodies and doors, rocket motor cases, oxygen tanks, printed circuits, and tennis rackets. Curing the composites with electron beams has two important advantages: (1) Curing time is reduced by almost two orders of magnitude (from 4 days to 2 h), and (2) thermal stresses are reduced and thus the quality of the product is substantially improved.

Aerospacial has recently purchased two, 10 MeV, 20 kW accelerators from CGR to irradiate rocket motor cases at 5 Mrad.

The last application listed in Table III is presently under development at Los Alamos National Laboratory.²⁵ Briefly, it requires a 1.6 GeV, 25 mA proton beam that strikes a Pb-Bi target producing 55 neutrons per proton. The long half-life nuclear wastes are separated from those with short half-life and are irradiated by the neutron flux. Transmutation reduces the half-life of wastes. The higher atomic weight actinides form fissionable products that produce power in excess of that required to drive the accelerator. The contemplated radio-frequency quadrupole (RFQ) linear accelerator is 1/4 mile long, requires a 55 ft wide tunnel, and its cost has been estimated at \$500 M.

Substantial savings in the cost of the accelerator and the housing facility may result if high-current, compact accelerators could be used to generate the high-energy proton beam. The potential of high-current accelerator technology to this important application is presently under evaluation. Results will be reported in a future publication.

In conclusion, accelerators have several interesting industrial applications. However, the majority of these applications require low unit irradiation cost. High-current, compact accelerators have the potential to reduce the unit irradiation cost, and therefore their development is a step in the right direction.

ACKNOWLEDGMENTS

This research was supported by the Office of Naval Research (ONR) and the Space and Naval Warfare Systems

Command (SPAWAR).

- ¹ W. Scharf, in *Particle Accelerators and their Uses*, edited by F. T. Cole (Harwood Academic, London, 1986), p. 839.
- ² G. B. Lubkin (Editor), *Phys. Today* **36**(8), 17 (1983).
- ³ C. A. Kapetanakos, L. K. Len, T. Smith, J. Golden, K. Smith, S. J. Marsh, D. Dialetis, J. Mathew, P. Loschialpo, and J. H. Chang, *Phys. Rev. Lett.* **64**, 2374 (1990).
- ⁴ H. Ishizuka, R. Prohasko, A. Fisher, and N. Rostoker, in *Proceedings of the 7th International Conference on High-Power Particle Beams* (Kernforschungszentrum Karlsruhe GmbH, Karlsruhe, Germany, 1988), Vol. II, p. 857.
- ⁵ S. Humphries, Jr. and L. K. Len, in *Proceedings of 1987 IEEE Particle Accelerator Conference* (IEEE, New York, 1987), p. 914.
- ⁶ V. Bailey, L. Schlitt, M. Tiefenbach, S. Putnam, A. Mondelli, D. Chernin, and J. Petello, in *Proceedings of 1987 IEEE Particle Accelerator Conference* (IEEE, New York, 1987), p. 920.
- ⁷ W. K. Tucker, S. L. Shope, and D. E. Hasti, in *Proceedings of 1987 IEEE Particle Accelerator Conference* (IEEE, New York, 1987), p. 957.
- ⁸ M. R. Cleland (private communication).
- ⁹ P. Sprangle and C. A. Kapetanakos, *J. Appl. Phys.* **49**, 1 (1978).
- ¹⁰ C. A. Kapetanakos, P. Sprangle, D. P. Chernin, S. J. Marsh, and I. Haber, *Phys. Fluids* **26**, 1634 (1983).
- ¹¹ N. Rostoker, *Comments Plasma Phys.* **6**, 91 (1980).
- ¹² R. L. Gluckstern, in *Proceedings of Linear Accelerator Conference* (Brookhaven Laboratory, Upton, NY, 1979), p. 245.
- ¹³ C. Roberson, A. Mondelli, and D. Chernin, *Phys. Rev. Lett.* **50**, 507 (1983).
- ¹⁴ C. A. Kapetanakos, S. J. Marsh, and D. Dialetis, *Phys. Rev. Lett.* **61**, 86 (1988).
- ¹⁵ J. Golden, L. K. Len, A. V. Deniz, J. Mathew, T. J. Smith, P. Loschialpo, J. H. Chang, D. Dialetis, S. J. Marsh, and C. A. Kapetanakos, in Ref. 1, Vol. I, p. 221.
- ¹⁶ L. K. Len, T. Smith, J. Golden, K. Smith, S. J. Marsh, D. Dialetis, J. Mathew, P. Loschialpo, J. H. Chang, and C. A. Kapetanakos, *Proceedings of International Society for Optical Engineers (SPIE)* (SPIE, Bellingham, WA, 1990), Vol. 1226, p. 382.
- ¹⁷ P. Sprangle and C. A. Kapetanakos, *Part. Accel.* **18**, 203 (1986).
- ¹⁸ D. Chernin and P. Sprangle, *Part. Accel.* **12**, 101 (1982).
- ¹⁹ C. W. Roberson, A. Mondelli, and D. Chernin, *Part. Accel.* **17**, 79 (1985).
- ²⁰ P. Sprangle, J. Krall, C. M. Tang, and C. A. Kapetanakos, *Bull. Am. Phys. Soc.* **35**, 1005 (1990).
- ²¹ T. P. Hughes and B. B. Godfrey, *Phys. Fluids* **29**, 1698 (1986).
- ²² See National Technical Information Service Document No. DE84001632 (U.S. Department of Energy Report No. DOE/ER-0176, 1983). Copies may be obtained from the National Technical Information Service, Springfield, Virginia 22161. The price is \$23.00 plus a \$3.00 handling fee. All orders must be prepaid.
- ²³ J. Silverman (private communication).
- ²⁴ P. K. Mallick, *Fiber-Reinforced Composites* (Marcel Dekker, New York, 1988).
- ²⁵ C. D. Bowman (private communication).

Beam trapping in a modified betatron accelerator

C. A. Kapetanakos, D. Dialetis,^{*} S. J. Marsh,[†] L. K. Len,[‡] and T. Smith[‡]
Plasma Physics Division, Naval Research Laboratory, Washington, D.C. 20375-5000
 (Received 24 May 1991)

The experimental results on the trapping of the beam in the Naval Research Laboratory modified betatron accelerator are in good agreement with a revised model of resistive trapping, and thus it may be concluded that the wall resistivity is responsible for the inward spiral motion of the beam after injection.

INTRODUCTION

Currently, several laboratories [1–5] are engaged in studies to assess the feasibility of compact, high-current accelerators. Among the various accelerating schemes presently under investigation is the modified betatron accelerator (MBA) [6–8]. This device is under study at the University of California, Irvine [2] and also at the Naval Research Laboratory (NRL). Since the initial successful demonstration of acceleration [1] approximately two years ago, the NRL-MBA has achieved [11] trapped currents as high as 1.5 kA and energies approximately 18 MeV. The beam lifetime that is typically 700–900 μ sec is limited by the cyclotron resonance.

Following the installation of strong focusing windings [9,10] in the NRL device it is routinely observed [1,11] that for several combinations of injection parameters the beam consistently spirals from the injection position to the magnetic minor axis and is trapped. The explanation of this interesting phenomenon has been so far elusive. However, a fair understanding of the trapping mechanism is not only of academic interest but a necessity for any upgrading of the existing or the construction of a new device.

In this paper we report recent experimental results on the trapping of the beam in the NRL-MBA. The results are in agreement with a revised model of resistive trapping [12]. Two modifications have been introduced to the original model. First, the beam motion is not limited near the minor axis and therefore nonlinear effects and the fast diffusion times that scale as $\mu_0(b-a)^2/\pi^2\rho$, where $b-a$ is the thickness of the chamber and ρ is the wall resistivity, become important. Second, in order to take into account the intermediate motion [10] of the beam that has been omitted in the calculation of the image fields of the beam, the wall surface resistivity is computed using the skin depth that corresponds to the frequency of the intermediate mode and not the actual thickness of the chamber.

There are three distinct groups of diffusion times with which the self-magnetic-field of the beam leaks out of a resistive torus. The shortest are the “plane” characteristic times

$$\tau_{mk} \approx \mu_0(b-a)^2/\pi^2\rho k^2 = \frac{\tau_{01}}{k^2} \equiv \frac{\tau_p}{k^2},$$

where $k = 1, 2, 3, \dots$. The “plane” diffusion times are important when the beam is near the wall. The “cylinder” diffusion times are

$$\tau_{m0} \approx \tau_{10}/m = \tau_c/m = \mu_0 a(b-a)/2\rho m,$$

where $m = 1, 2, 3, \dots$. Both τ_p and τ_c determine the speed with which the self-magnetic-field of the beam penetrates the wall of the chamber and are instrumental in the resistive trapping of the beam. Finally, the “loop” diffusion time $\tau_{00} \equiv \tau_l = 2\tau_c[\ln(8r_0/a) - 2]$, where r_0 is the major radius of the torus, determines the speed with which the beam field diffuses into the hole of the doughnut. The “loop” diffusion time does not play any role in the resistive trapping of the beam.

The resistive trapping is due to the negative radial component of the image magnetic field of the beam that acts on its centroid, when such a beam moves poloidally inside a resistive chamber. This field component crossed with the axial (toroidal) velocity of the beam produces a poloidal force, which is in the opposite direction to the poloidal motion of the beam. In the absence of the strong focusing and when the self-fields dominate the external fields (high-current regime), the poloidal force in conjunction with the axial (toroidal) magnetic field drives the beam to the wall (drag instability [13]). However, in the presence of strong focusing the direction of the poloidal motion can be reversed and the beam spirals to the minor axis [12].

BRIEF DESCRIPTION OF THE EXPERIMENT

The NRL modified betatron has been described [1,14] previously. In this paper we give, for completeness, a short description of its basic components. The NRL-MBA is a toroidal device that comprises three different external magnetic fields; the betatron field B_z that can vary from 0–2.7 kG, the toroidal field B_θ that can vary between 0–5.1 kG, and the strong focusing field that has a maximum gradient between 0–31 G/cm, when the current I_{SF} in the windings varies from 0–30 kA.

The 100-cm major radius, 15.2-cm-inside minor radius vacuum chamber has been constructed using epoxy-reinforced carbon fibers. The desired conductivity is obtained by embedding in the outer layer of graphite a phosphor bronze screen. The measured dc resistance of the toroidal vessel is 68 ± 2 m Ω and the corresponding

Work of the U. S. Government
 Not subject to U. S. copyright

surface resistivity is $10.3 \text{ m}\Omega$ on a square. The graphite surface resistivity is $26.6 \text{ m}\Omega$ on a square.

The electrons are emitted from one end-face of a cylindrical carbon cathode. The other end-face is mounded on the cathode stalk. The emitting surface of the cathode faces the circular opening of the conical anode, which is located on the midplane of the device, 8.7 cm from its minor axis.

EXPERIMENTAL RESULTS

Over a wide range of parameters and after fine tuning the external fields the beam spirals from the injector near the minor axis and is trapped. The beam trapping time, i.e., the time it takes the beam to travel from the injection position to the vicinity of the minor axis is determined by measuring the time delay between the x-ray peaks that are generated at injection and at a $1 \times 1.1\text{-cm}$, 0.8-mm-thick lead target that is located on the magnetic minor axis. The lead target is mounted on the front surface of a 3- μm -thick polycarbonate foil that is stretched across the minor cross section of the vacuum chamber as shown in Fig. 1(a). The x rays are monitored by a collimated x-ray detector that is located 4 m away from the lead target. The scintillator-photomultiplier tube is housed inside a lead box and the x rays enter the scintillator through a 3-mm-diam hole. The foil is graphite coated on the upstream side to avoid charging. Figure 1(b) shows an open-shutter photograph of the light emitted as the beam passes through the foil. The x rays emitted as the beam

strikes the diode and the lead target are shown in the upper trace of Fig. 1(c). The trapping time τ_{tr} for this shot is $1.25 \mu\text{sec}$. The lower trace of Fig. 1(c) shows the output of the Rogowski coil that monitors the beam current. The peak of the signal corresponds to 1.2 kA.

The results shown in Fig. 1 were taken with a 0.5-cm hole in the anode. This hole is by a factor of 3 smaller than that used regularly in the NRL device. Thus, the trapped current has been reduced by a factor of 2-3. This reduction in the beam current was necessary in order to achieve satisfactory resolution in the open-shutter photographs.

To determine the effect of the foil on the transverse beam orbit, we carried out a series of experiments in which the 3- μm -thick foil was replaced with a foil of the same composition but with only half its thickness. The results show that the equilibrium position of the beam is slightly larger in the case of 1.5- μm -thick foil. It requires approximately 1-2 G higher vertical field ($\sim 4-8\%$) to shift the equilibrium to its original position and make the orbits identical.

As the electrons pass through the plastic foil, they suffer both inelastic and elastic scattering. The stopping power [15] of 0.6 MeV electrons passing through polyethylene (data for polycarbonate are not available) is $\sim 2 \text{ (MeV cm}^2\text{)/gm}$. Thus, the energy loss per pass is 0.6 keV. The total energy loss in $1.2 \mu\text{sec}$, i.e., in sixty revolutions around the major axis, is 36 keV or $\sim 6\%$. The energy loss in the thinner foil is only 18 keV and therefore the equilibrium position is expected to increase by

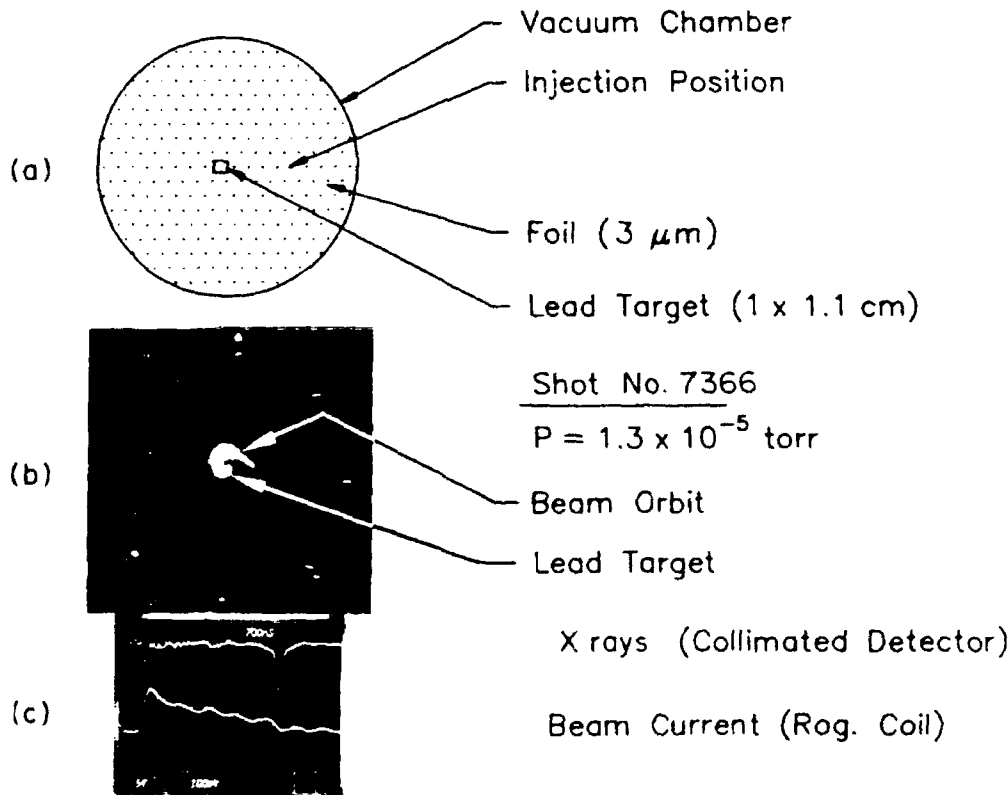


FIG. 1. Beam trapping time.

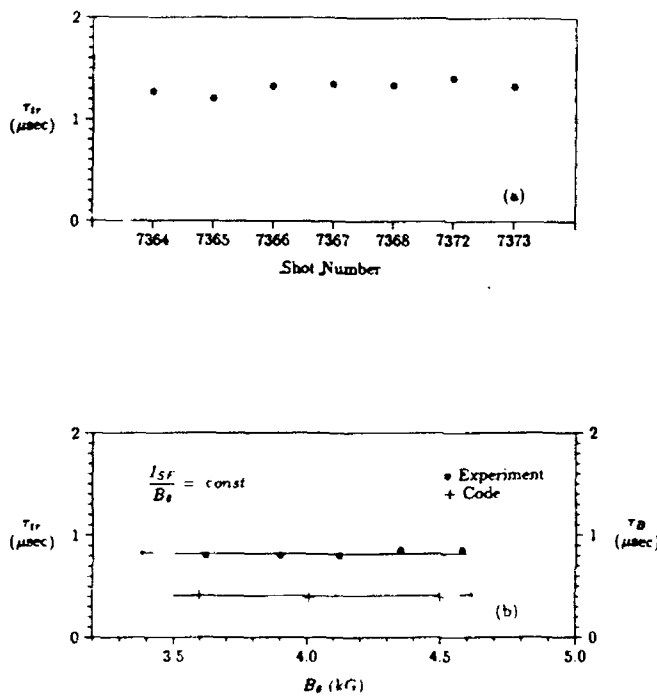


FIG. 2. (a) Trapping time reproducibility and (b) dependence of τ_{tr} and τ_B on B_θ for constant I_{SF}/B_θ .

3% when the thickness of the foil is reduced to half. This shift is not substantially different from that observed in the experiment. The elastic-scattering induced RMS angle is 0.9° for the first pass through the $1.5\text{-}\mu\text{m}$ -thick foil. Although substantial, the elastic scattering does not contribute to the shift of the equilibrium position.

The beam orbits are very reproducible and τ_{tr} shows only modest variations for the same operating parameters. Figure 2(a) shows τ_{tr} for seven shots taken with the same values of the fields. It is apparent from this figure that τ_{tr} varies by $\pm 7\%$. In a second run with five shots the variation was even smaller. Figure 2(b) shows τ_{tr} , vs B_θ for constant I_{SF}/B_θ , where I_{SF} is the current of the strong-focusing windings. For all practical purposes τ_{tr} remains constant in the narrow range tested.

In addition to τ_{tr} , the bounce period τ_B , i.e., the time the beam takes to perform a complete revolution in the poloidal direction, is of special interest. To determine τ_B , the foil target was removed and replaced with a 1.1-cm-wide, 1-mm-thick, 16-cm-long lead strip. The lead target is backed on the upstream side by a thin plastic strip and is mounted on a half lucite ring that is carbon coated. The symmetry axis of the target lies on the midplane of the device as shown in Fig. 3(a).

The light emitted from the upstream side of the target when the beam strikes it is monitored with an open

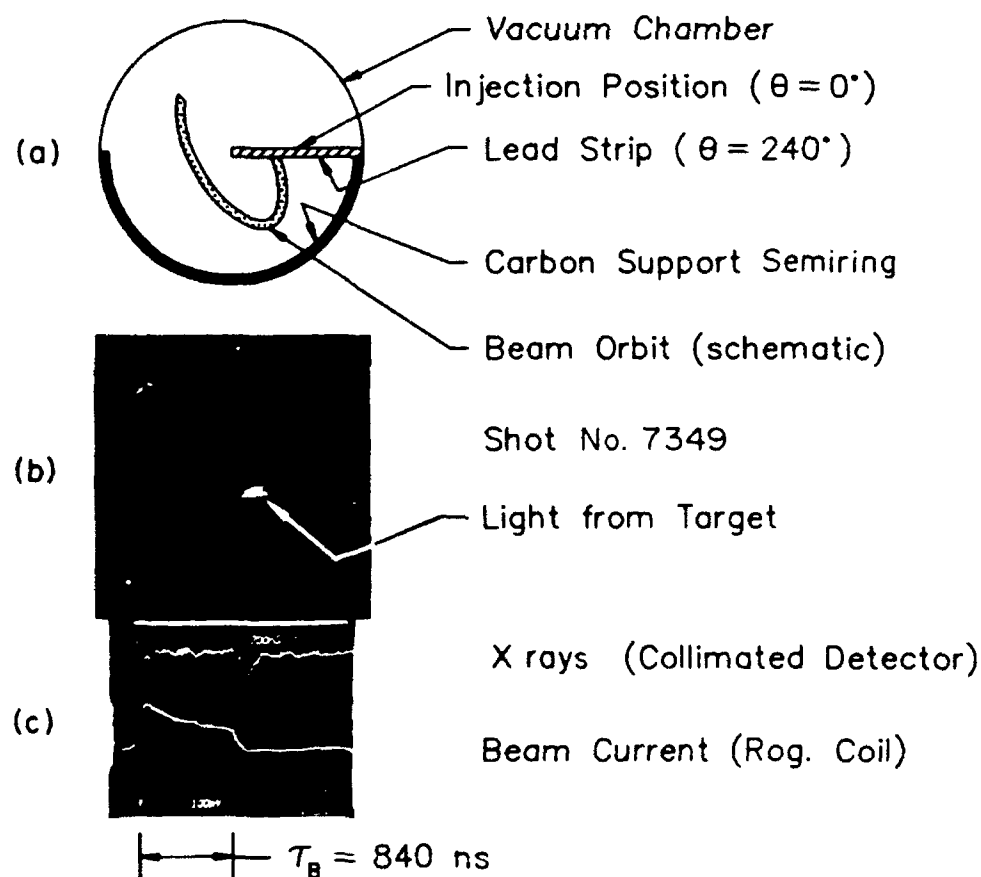


FIG. 3. Beam bounce period.

shutter camera. Results are shown in Fig. 3(b). The x-ray signal and the output of the Rogowski coil that monitors the beam current are shown in Fig. 3(c). The bounce period is inferred from the time delay of the two x-ray peaks, as indicated in Fig. 3(c), and in this shot is 840 nsec. The damage pattern on the lead strip has a diameter that is equal to the diameter of the anode hole. This implies that the diameter of the beam has not changed after about 40 revolutions around the major axis. In addition, we observe that the damage pattern is a semicircle that is always located near the lower edge of the strip. From this observation it may be concluded that the beam drifts 3 mm over 20 nsec, i.e., its bounce speed near the strip is $\sim 15 \text{ cm}/\mu\text{sec}$.

To verify that there is no correlation between τ_{tr} and τ_I , i.e., with the speed the beam magnetic field diffuses into the hole of the doughnut, the vacuum chamber was unbolted in two joints that are located 180° apart in the toroidal direction and a ring insulator was inserted in each of these joints. Sixty carbon resistors, 51Ω each, were symmetrically mounted on the outer surface of one of the two rings as shown in Fig. 4(a). To improve its voltage holding capabilities the inner surface of the blue nylon insulator was angled and a 0.6-cm-deep groove was machined at its plane of symmetry. In addition, its inner surface was protected from stray electrons by a 0.8-mm-thick lead strap that is supported by an epoxy reinforced

carbon fiber belt. The purpose of the second insulator was only to minimize the distortion of the toroidal chamber and thus shorting wide straps, instead of resistors, were installed on its outer surface.

There are two distinct currents flowing on the wall of the vacuum chamber. The first i_w is due to the rising vertical field and the second I_r is induced by the beam. Since the vertical field during the first quarter period varies as $B_z(t) = B_{zp} \sin(2\pi t/\tau)$, where B_{zp} is the peak field and τ is the period, the induced voltage in the chamber is $V = -V_0 \cos(2\pi t/\tau)$, where $V_0 = (4\pi^2 r_0^2 / \tau) B_{zp}$, and r_0 is the major radius of the torus. The current flowing on the wall of the chamber is described by the equation $V = L(di_w/dt) + Ri_w$, where L is the inductance and R the resistance of the torus. The instantaneous value of i_w can be found by integrating the above equation and is given by

$$i_w = - \frac{V_0}{R \left[1 + \left(\frac{2\pi L}{R} \right)^2 \right]} \times \left[\cos(2\pi t/\tau) + \frac{2\pi L}{R} \sin(2\pi t/\tau) - e^{-t/(L/R)} \right], \quad (1)$$

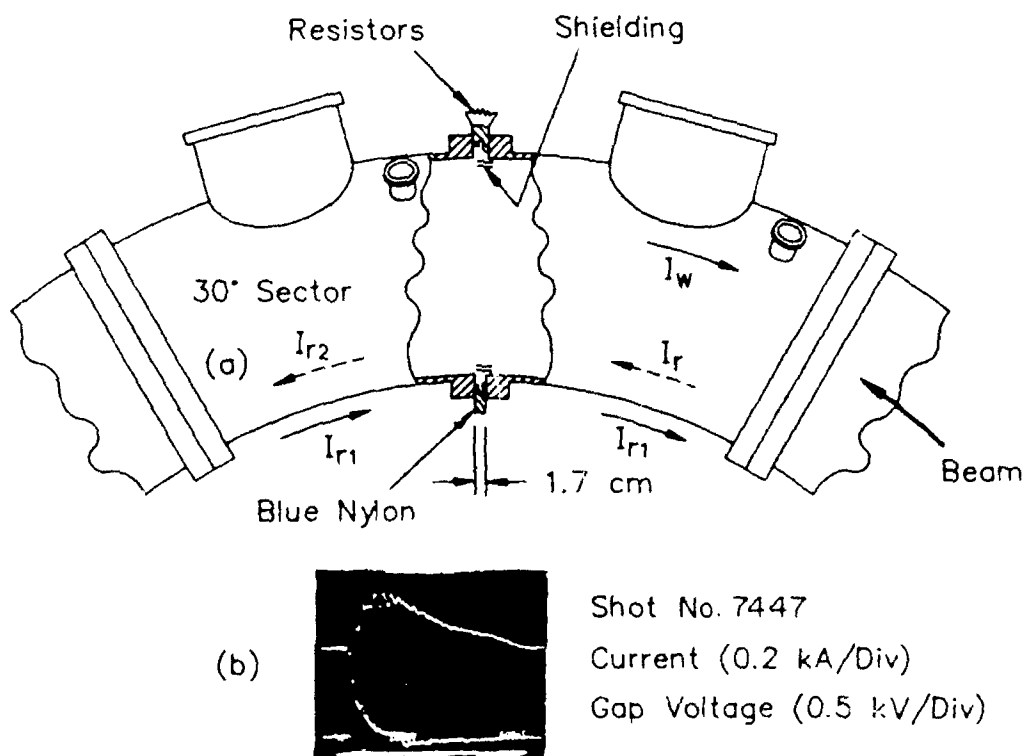


FIG. 4. (a) Schematic of the vacuum chamber joint with the insulator in place. (b) Current and gap voltage waveforms

with the initial condition $i_w(t=0)=0$.

The temporal profile of i_w predicted by the above simple model is identical to that predicted from the exact solution of the diffusion problem for a toroidal resistive shell [16] and also is in good agreement with the results of the TRIDIF code for a finite thickness toroidal vessel. According to Eq. (1), i_w has a maximum at time t_p , which for $\alpha \equiv 2\pi(L/R)/\tau \ll 1$ is determined from $\alpha^2[1-t_p/(L/R)] = -e^{-t_p/(L/R)}$. The peak value of the current is $i_{wp} = V/R$. The measured peak value of the current in the experiment is in good agreement with the above theoretical prediction and scales, as expected, with the value of the resistance at the gap.

The return current of the beam is measured with a fast Rogowski coil ($\tau_{rise} \approx 20$ nsec) that is located outside the vacuum chamber. With the resistors at the gap shorted, the Rogowski coil shows a slowly rising current that is consistent with the decay of I_r . However, when the shorting clips are removed the Rogowski coil shows a current pulse that rises to $\sim \frac{2}{3}$ of its peak value in less than 100 nsec as shown in Fig. 4(b). The lower trace in fig. 4(b) shows the voltage across the resistors V_g as measured directly by a Tektronix 7844 oscilloscope after a 100X attenuation. The shape of the time-integrated V_g is very similar to the current waveform registered by the Rogowski coil, i.e., V_g is proportional to the time derivative of the current.

COMPARISON WITH THEORY

The equations that describe the motion of the beam centroid have been solved numerically using analytical expressions for B_z and B_θ . The stellarator fields are determined numerically from Biot-Savart law by dividing each period of the windings into 20 segments. The image fields on the beam centroid have been computed analytically for a uniform density electron ring that is located inside a large major radius torus with resistive wall of thickness $b-a$, where a is the inner and b the outer radii of the torus. In contrast with previous calculation [12], the beam is not limited near the minor axis.

In the local cylindrical coordinate system (ρ, ϕ, z) with its origin on the geometric minor axis, the electrostatic potential inside the ring is given by [17]

$$\begin{aligned} \Phi_0 = \frac{Q_i}{2\pi\epsilon_0} & \left\{ \ln \frac{a}{r_b} + \frac{1}{2} - \frac{1}{2} \frac{\rho^2 + \Delta^2 - 2\Delta\rho \cos(\phi - \alpha)}{2r_b^2} \right. \\ & \left. + \frac{1}{2} \ln \left[1 + \left(\frac{\Delta\rho}{a^2} \right)^2 - 2 \frac{\Delta\rho}{a^2} \cos(\phi - \alpha) \right] \right\}, \end{aligned} \quad (2)$$

where Δ and α define the beam position on the transverse plane, r_b is the minor radius of the beam, and Q_i is the charge per unit length. Similarly, the magnetic vector potential inside the beam is [17]

$$\begin{aligned} A_{00} = \frac{\Phi_0 \beta_\theta}{c} + \sum_{k=0}^{\infty} A_{0k} U_{0k}^{(c)}(t) \\ + \sum_{m=1}^{\infty} \sum_{k=0}^{\infty} A_{mk} \left[\frac{\rho}{a} \right]^m [U_{mk}^{(c)}(t) \cos m\phi \\ + U_{mk}^{(s)}(t) \sin m\phi], \end{aligned} \quad (3)$$

where β_θ is the normalized toroidal beam velocity.

The time-dependent coefficients $U_{mk}^{(c)}(t), U_{mk}^{(s)}(t)$ are zero at $t=0$ and are determined by the differential equations

$$\begin{aligned} \dot{U}_{mk}^{(c)} + \frac{1}{\tau_{mk}} U_{mk}^{(c)} &= \frac{Q_i \beta_\theta}{2\pi\epsilon_0 c \tau_{mk}} \left[\frac{\Delta}{a} \right]^m \cos m\alpha, \\ \dot{U}_{mk}^{(s)} + \frac{1}{\tau_{mk}} U_{mk}^{(s)} &= \frac{Q_i \beta_\theta}{2\pi\epsilon_0 c \tau_{mk}} \left[\frac{\Delta}{a} \right]^m \sin m\alpha, \end{aligned} \quad (4)$$

where

$$\frac{1}{\tau_{mk}} = \frac{\alpha_{mk}^2}{\mu_0 \sigma}, \quad m = 0, 1, 2, \dots, \quad k = 0, 1, 2, \dots,$$

σ is the wall conductivity of the toroidal chamber, and α_{mk} are the zeros of the function

$$\begin{aligned} f_0(\alpha) = \frac{\pi}{2} x_0 [J_1(x_0) Y_0(x_1) - Y_1(x_0) J_0(x_1)] \\ - \frac{\pi}{2} \left[\ln \frac{8R_b}{b} - 2 \right] x_0 x_1 [J_1(x_0) Y_1(x_1) \\ - Y_1(x_0) J_1(x_1)] \end{aligned} \quad (5)$$

when $m=0$, and

$$\begin{aligned} f_m(\alpha) = \frac{\pi}{4} x_0 x_1 [J_{m+1}(x_0) Y_{m-1}(x_1) \\ - Y_{m+1}(x_0) J_{m-1}(x_1)] \end{aligned} \quad (6)$$

when $m=1, 2, 3, \dots$. The arguments of Bessel functions in (5) and (6) are $x_0 = \alpha a$, $x_1 = \alpha b$ and R_b is the major radius of the beam. For each m there is an infinite number of zeros denoted by the index $k=0, 1, 2$. The time-dependent coefficients A_{0k}, A_{mk} that appear in the vector potential are equal to

$$A_{mk} = - \frac{2g_m(\alpha_{mk})}{\alpha_{mk} f'_m(\alpha_{mk})},$$

where $f'_m(\alpha)$ is the derivative of $f_m(\alpha)$ and

$$\begin{aligned} g_0(\alpha) = \frac{\pi}{2} [J_0(x_0) Y_0(x_1) - Y_0(x_0) J_0(x_1)] \\ - \frac{\pi}{2} \left[\ln \frac{8R_b}{b} - 2 \right] x_1 [J_0(x_0) Y_1(x_1) \\ - Y_0(x_0) J_1(x_1)] \end{aligned}$$

when $m=0$, and

$$g_m(\alpha) = \frac{\pi}{2} x_1 [J_{m+1}(x_0) Y_{m-1}(x_1) - Y_m(x_0) J_{m-1}(x_1)]$$

when $m = 1, 2, 3, \dots$. The image fields at the beam centroid, i.e., when $\rho = \Delta$ and $\phi = \alpha$, are obtained from the expressions of Φ_0 and A_{0k} given above.

The radial components $B_\rho^{(c)}$ at the beam centroid is of special interest because it is responsible for the inward radial motion of the beam. This component is given by

$$B_\rho^{(c)} = \sum_{m=1}^{\infty} \sum_{k=0}^{\infty} \frac{m}{a} A_{mk} \left[\frac{\Delta(t)}{a} \right]^{m-1} \times [-U_{mk}^{(s)}(t) \cos m\alpha(t) + U_{mk}^{(c)}(t) \sin m\alpha(t)]. \quad (7)$$

Since $B_\rho^{(c)}$ is independent of A_{0k} and $U_{0k}^{(c)}$, i.e., it is independent of loop time $\tau_l = \tau_{00}$, the beam trapping time should also be independent of τ_l as observed in the experiment.

TABLE I. Parameters of the run shown in Fig. 5.

Torus major radius r_0	100 cm
Torus minor radius a	15.2 cm
Relativistic factor γ	1.5
SF radius ρ_0	23.4 cm
SF current I_{SF}	24 kA
Vertical field at injection B_{10}	26 G
Toroidal field B_{00}	4 kG
Beam minor radius r_b	3 mm
Beam current I_b	1.2 kA
Wall resistivity	8 mΩ cm
Intermediate frequency, ω_w	1.8 × 10 ⁹ sec ⁻¹

To gain further insight, we have computed the image fields, including first-order toroidal corrections, at the beam centroid for a beam inside a resistive toroidal shell—in this case $B_\rho^{(c)}$:

$$B_\rho^{(c)}(\text{shell}) = \frac{\sin \alpha}{R_b} \left[\frac{Q_l \beta_\theta}{4\pi \epsilon_0 c} \left[\ln \frac{a}{r_b} + 1 \right] + \frac{Q_l \beta_\theta}{4\pi \epsilon_0 c} \ln \left[1 - \left[\frac{\Delta(t)}{a} \right]^2 \right] - \frac{Q_l \beta_\theta}{16\pi \epsilon_0 c} \left[\frac{r_b}{a} \right]^2 \frac{1}{1 - \left[\frac{\Delta}{a} \right]^2} \right] + \frac{1}{2} \sum_{m=1}^{\infty} \frac{1}{m} \left[\frac{\Delta(t)}{a} \right]^m [U_{cm}^{(0)}(t) \cos m\alpha(t) + U_{sm}^{(0)}(t) \sin m\alpha(t)] + \frac{1}{2} \left[\ln \frac{8R_b}{a} - 2 \right] U_0^{(0)}(t) + U_0^{(1)}(t) + \frac{1}{a} \sum_{m=1}^{\infty} \left[\frac{\Delta(t)}{a} \right]^{m-1} \{ -[U_{sm}^{(0)}(t) + U_{sm}^{(1)}(t) + V_{sm}^{(1)}(t)] \cos m\alpha + [U_{cm}^{(0)}(t) + U_{cm}^{(1)}(t) + V_{cm}^{(1)}(t)] \sin m\alpha(t) \}, \quad (8)$$

where the time-dependent parameters $U_0^{(0)}(t)$, $U_0^{(1)}(t)$, $U_{cm}^{(0)}(t)$, $U_{sm}^{(0)}(t)$, $U_{cm}^{(1)}(t)$, $U_{sm}^{(1)}(t)$, $V_{cm}^{(1)}(t)$, and $V_{sm}^{(1)}(t)$ are zero at $t=0$ and are determined by the differential equations

$$\dot{U}_0^{(0)} + \frac{1}{\tau_l} \left[1 + \tau_c \frac{\dot{x}_c}{R_b} \right] U_0^{(0)} = \frac{2Q_l \beta_\theta}{4\pi \epsilon_0 c} \frac{1}{\tau_l} \left[1 + \frac{x_c}{2R_b} \right],$$

$$\dot{U}_0^{(1)} + \frac{1}{\tau_c} U_0^{(1)} = \frac{1}{2\tau_c} U_0^{(0)},$$

$$\dot{U}_{cm}^{(0)} + \frac{m}{\tau_c} U_{cm}^{(0)} = \frac{2Q_l \beta_\theta}{4\pi \epsilon_0 c} \frac{m}{\tau_c} \left[\frac{\Delta}{a} \right]^m \cos m\alpha,$$

$$\dot{U}_{sm}^{(0)} + \frac{m}{\tau_c} U_{sm}^{(0)} = \frac{2Q_l \beta_\theta}{4\pi \epsilon_0 c} \frac{m}{\tau_c} \left[\frac{\Delta}{a} \right]^m \sin m\alpha,$$

$$\dot{U}_{cm}^{(1)} + \frac{m}{\tau_c} U_{cm}^{(1)} = -\frac{\dot{x}_c}{2R_b} U_{cm}^{(0)},$$

$$\dot{U}_{sm}^{(1)} + \frac{m}{\tau_c} U_{sm}^{(1)} = -\frac{x_c}{2R_b} U_{sm}^{(0)},$$

$$\dot{V}_{cm}^{(1)} + \frac{m}{\tau_c} V_{cm}^{(1)} = \frac{Q_l \beta_\theta}{16\pi \epsilon_0 c} \frac{m^2}{\tau_c} \frac{a}{R_b} \left[\frac{r_b}{a} \right]^2 \times \left[\frac{\Delta}{a} \right]^{m-1} \cos(m-1)\alpha,$$

$$\dot{V}_{sm}^{(1)} + \frac{m}{\tau_c} V_{sm}^{(1)} = \frac{Q_l \beta_\theta}{16\pi \epsilon_0 c} \frac{m^2}{\tau_c} \frac{a}{R_b} \left[\frac{r_b}{a} \right]^2 \times \left[\frac{\Delta}{a} \right]^{m-1} \sin(m-1)\alpha,$$

where

$$\tau_0 = 2\tau_c \left[\ln \frac{8R_b}{a} - 2 - \frac{x_c}{2R_b} \right],$$

and

$$x_c = \Delta \cos \alpha \equiv R_b - r_0.$$

It is apparent from Eqs. (8) and (9) that the toroidal correction term of $B_\rho^{(c)}$ is a function of τ_l . However, this term is multiplied by $\sin \alpha(t)$ and therefore averages to zero in a poloidal period.

In the limit $(b-a) \ll a$, the toroidal electric field E_θ on the outer surface of the chamber for a stationary beam has a relatively simple, closed form. At $t=0$, $E_\theta=0$ and peaks within a few fast diffusion times τ_p . For a longer time, E_θ decays to zero with τ_l . This form of the electric field is consistent with the observed return current after the beam injection. When the resistors at the gap are shorted the current measured with the external Rogowski coil should rise at the same rate the beam return current

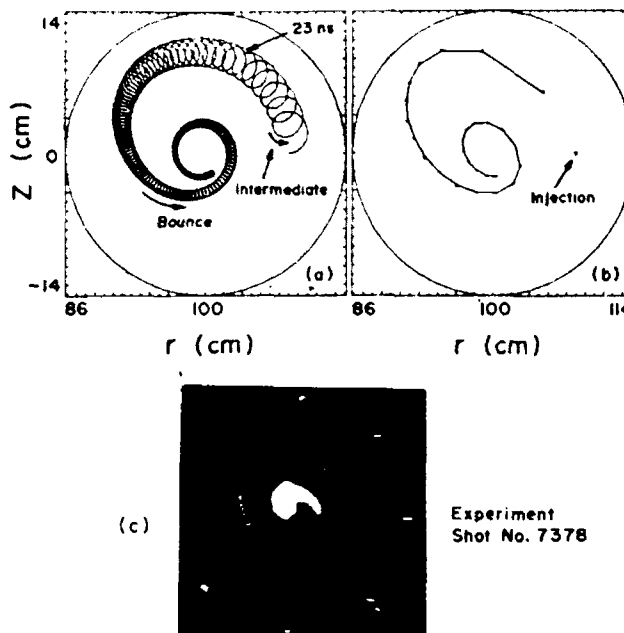


FIG. 5. Beam centroid orbit from the numerical integration of the equations of motion, using the image fields from the resistive shell model [(a) and (b)]. Results from the experiment (c).

decays. However, when the resistors at the gap are not shorted, a portion (I_{r1}) of the return current (I_r) flows on the outer wall of the chamber as shown in Fig. 4. I_{r1} rises considerably faster because the beam magnetic field can leak locally out of the resistive gap considerably faster than it can leak out of a uniform chamber.

Results from the numerical integration of orbit equations are shown in Fig. 5. The various parameters for the run are listed in Table I. Figure 5(a) shows the projection of the centroid's orbit on the $\theta=0$ plane. Both the intermediate and slow (bounce) modes are apparent. Since there are six field periods between $0 \leq \theta \leq 2\pi$, the electrons perform six oscillations during one revolution around the major axis. To take into account the intermediate motion that has been neglected in the calculation of the image fields, the surface resistivity in the code is

computed using the skin depth that corresponds to the intermediate frequency and not the actual thickness of the wall.

The solid circles in Fig. 5(b) show the positions the beam crosses the $\theta=240^\circ$ plane. This is a realistic simulation of the experimental situation. The time difference between two circles is equal to the period around the major axis, i.e., ~ 23 nsec. The parameters of this run are similar to those in Fig. 5(c) and the similarity of the two orbits is quite apparent. When the crossing plane is moved from $\theta=240^\circ$ to a different azimuthal position θ , the beam orbit rotates around the minor axis. The rotation predicted by the theory is very similar to that observed in the experiment.

There is some ambiguity, both in the experiment and theory, in the determination of the beam trapping time, because its exact value depends on the position and size of the target. However, this is not the case with τ_B , which can be measured very accurately. We made four computer runs for different values of B_θ keeping $I_{SF}/B_\theta = \text{constant}$. Figure 2(b) shows τ_B vs B_θ for three of these runs. For all practical purposes τ_B remains constant as B_θ varies. In the fourth run B_θ was reduced to 2 kG and although the beam orbit changed substantially τ_B was lower only by 7%.

As a rule, the theory predicts a τ_B and τ_r that are approximately a factor of 2 shorter than those observed in the experiment. With the exception of these two times the revised model of resistive trapping is in agreement with the experiment observations, although in the analysis the beam current remains constant while in the experiment the current decays. This decay is observed whenever there is a target inside the chamber but in general is absent during the acceleration experiments when the various targets are removed.

ACKNOWLEDGMENTS

This work is supported by the Office of Naval Research and the Space and Naval Warfare Command.

*Permanent address: Science Applications International Corporation, 1710 Goodridge Drive, McLean, VA 22102.

[†]Permanent address: SFA, Inc., Landover, MD 20785.

[‡]Permanent address: FM Technologies, Inc., 10529-B Braddock Road, Fairfax, VA 22032.

[1] C. A. Kapetanakos *et al.*, Phys. Rev. Lett. **64**, 2374 (1990).

[2] H. Ishizuka *et al.*, in *Proceedings of the Seventh International Conference on High-Power Particle Beams, Karlsruhe, Germany, 1988*, edited by W. Bauer and W. Schmidt (Kernforschungszentrum Karlsruhe GmbH, Karlsruhe, 1988), Vol. II, p. 857.

[3] S. Humphries, Jr., and L. K. Len, in *Proceedings of the 1987 Particle Accelerator Conference, Washington, D.C., 1987*, edited by E. R. Lindstrom and L. S. Taylor (IEEE,

New York, 1987), p. 914.

[4] V. Bailey *et al.*, in *Proceedings of the 1987 Particle Accelerator Conference* (Ref. 3), p. 920.

[5] W. K. Tucker *et al.*, in *Proceedings of the 1987 Particle Accelerator Conference* (Ref. 3), p. 957.

[6] P. Sprangle and C. A. Kapetanakos, J. Appl. Phys. **49**, 1 (1978).

[7] C. A. Kapetanakos *et al.*, Phys. Fluids **26**, 1634 (1983).

[8] N. Rostoker, Comments Plasma Phys. **6**, 91 (1980).

[9] C. Roberson *et al.*, Phys. Rev. Lett. **50**, 507 (1983).

[10] C. A. Kapetanakos *et al.*, Part. Accel. **21**, 1 (1987).

[11] C. A. Kapetanakos *et al.*, Phys. Fluids (to be published).

[12] P. Sprangle and C. A. Kapetanakos, Part. Accel. **18**, 203 (1986); Y. Seo and P. Sprangle, *ibid.* (to be published).

- [13] P. Sprangle and C. A. Kapetanakos, *Part. Accel.* **14**, 15 (1983).
- [14] L. K. Len *et al.*, in *Intense Microwave and Particle Beams*, Proceedings of the International Society for Optical Instrumentation Engineers, Los Angeles, CA, January 1990 (SPIE, Bellingham, WA, 1990), Vol. 1226, p. 38.
- [15] M. J. Berger and S. M. Seltzer, *NASA Report No. SP-3012*, 1964 (unpublished).
- [16] D. Dialetis *et al.*, *J. Appl. Phys.* **69**, 1813 (1991).
- [17] D. Dialetis *et al.* (unpublished).

Excitation of the $\ell = 12$ Cyclotron Resonance in the NRL Modified Betatron Accelerator*

L. K. Len,^{a)} T. Smith,^{a)} P. Loschialpo, J. Mathew, S. J. Marsh,^{b)} D. Dialetis,^{c)}
J. Golden,^{d)} J.H. Chang and C. A. Kapetanakos

Plasma Physics Division, Naval Research Laboratory, Washington, DC 20375-5000

The basic periodicity in the NRL device is twelve-fold. There are twelve toroidal field coils, twelve sectors, and so on. For a long time, the $\ell = 12$ resonance was the dominant resonance in the experiment. To test the importance of the $\ell = 12$ resonance, we have intentionally introduced an $\ell = 12$ field error using twelve resonant coils. By activating these coils when the resonance is observed, the duration of x-rays produced by beam loss was reduced from 900 μ s to 5.5 μ s, while the amplitude of the signal increased from 0.5 to \sim 40 volts. The full width of the x-ray pulse at half maximum is inversely proportional to the current through the resonant coils and proportional to the risetime of the pulse. Work is in progress with a set of twelve internal coils that have a risetime of 300 - 400 ns. The results with these coils have confirmed the importance of the $\ell = 12$ resonance. In addition, it has been shown experimentally that by adding a ΔB_θ such that the ratio of the total toroidal magnetic field to the vertical field is not an integer, the cyclotron resonance is not excited. These experiments have extended the beam lifetime by more than 100 μ s, which is approximately equal to the risetime of the applied ΔB_θ pulse. In the presence of such a pulse, the beam lifetime is 1 ms and the electron beam energy is 22 MeV, while the trapped current is in excess of 1 kA.

I. INTRODUCTION

The lifetime of the electron beam in the NRL modified betatron accelerator has been limited by the excitation of the cyclotron resonances.¹ These resonances occur whenever the condition $(B_{\theta o}/B_{z o}) = (2\ell^2 - 1)/2\ell$ is satisfied, with ℓ taking integer values.^{2,3} Here $B_{\theta o}$ and $B_{z o}$ are the toroidal and vertical magnetic fields on the minor axis of the chamber. In this paper, we present results from several experiments related to the excitation of electron cyclotron resonances. The first experiment deals specifically with the $\ell = 12$ resonance and the second addresses the spatial distribution of the beam losses. In the third experiment, a time rising ΔB_θ has been added to the main B_θ field. This has effectively resulted in a total $B_{\theta T}$ that maintains the condition of $B_{\theta T}/B_z = \text{constant} \neq \text{integer}$ over the risetime of the ΔB_θ pulse, and thus the beam does not cross any resonance.

II. EXPERIMENTAL APPARATUS

Detailed description of the NRL modified betatron accelerator can be found in previous publications^{1,4-7} where various experimental results, including observation of the electron cyclotron resonances were reported. There are three main external magnetic fields that provide confinement to the high current beam, namely, the toroidal (B_θ), the strong focusing (B_{sf}), and the vertical (B_z) fields. They are generated by pulsed, aircore

electromagnets and have risetimes equal to 2.3 ms, 1.0 ms, and 2.6 ms respectively. The peak value of B_θ is ~ 5 kG and that of B_z is ~ 2 kG. The strong focusing windings can be operated at peak currents as high as ~ 30 kA.

Two sets of resonant coils have been used in the experiments reported in this paper. A set of 12 single-turn coils are installed on the outside of the vacuum chamber (external resonant coils). They are approximately equally spaced around the toroidal chamber. The drivers for these coils can be configured to generate ΔB_θ with risetime of 12 and 5 μ s. To generate a faster resonant pulse, these coils have been replaced with 12 single-turn internal coils that are located accurately at the joints between sectors as shown in Fig. 1. The internal coils are wound on a blue nylon housing and encapsulated with epoxy.

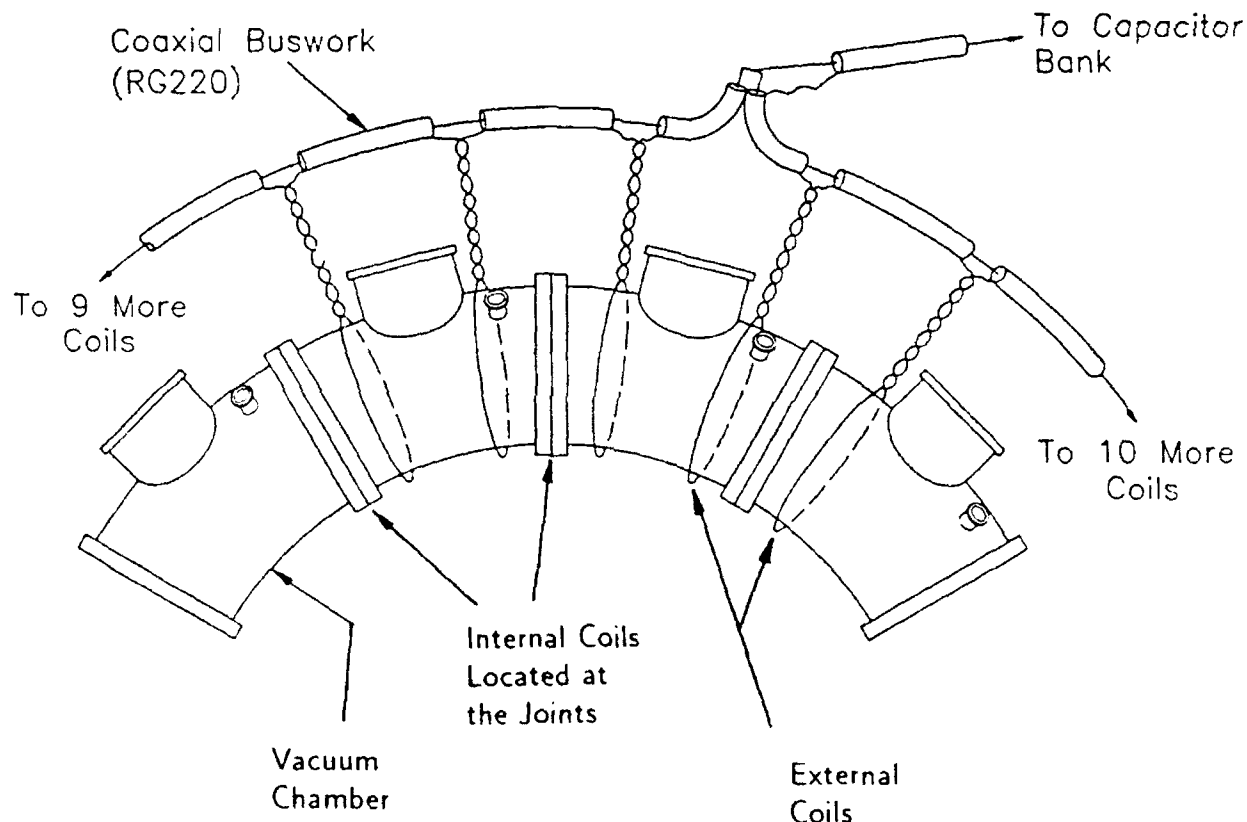


FIG. 1 Schematic view of the resonant coils with respect to the vacuum chamber sectors.

In the experiment with $B_{\theta T}/B_z = \text{constant} \neq \text{integer}$, the number of external coils was increased to 24 in order to produce a smoother ΔB_θ . In addition, the pulsed power driver was modified to increase the quarter period risetime to ~ 100 μ s.

Beam injection is initiated near the peak of the toroidal and strong focusing fields. The injector diode is located inside the vacuum chamber 8.6 cm from the minor axis. When the ratio of B_θ to B_z is nearly 12, the resonant coils are energized to produce the ΔB_θ disturbance. Diagnostics includes the following: Magnetic field probes to measure B_θ and B_z , three NPM-54 x-ray detectors that monitor the x-rays generated when the beam strikes the chamber wall, a Rogowski belt to measure the electron beam current and optical fibers that are located on the outside of the vacuum chamber. The light emitted when the energetic electrons strike these fibers is monitored with photomultiplier tubes. This technique has allowed us to determine accurately the beam dump positions.

III. EXPERIMENTAL RESULTS

In the modified betatron the electron beam performs a complicated motion following injection. To avoid hitting the diode or/and the wall as the beam spirals onto the minor axis during the trapping process, it is necessary to select the operating parameters carefully to maximize the beam trapping efficiency. The signals from the x-ray detectors looking at the diode and the lead shielding around the Rogowski belt are used in conjunction with the beam current monitor as a guide to arrive at the optimum field settings. The beam lifetime is inferred from the x-ray signal such as that shown in Fig. 2. The main peak at $800 \mu\text{s}$ corresponds to an energy of 20 MeV while the last peak at $1300 \mu\text{s}$ is 28 MeV.

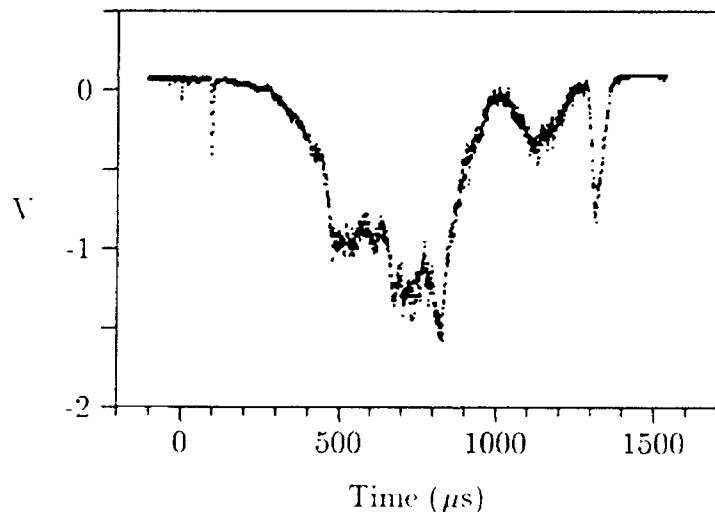


FIG. 2. Typical x-ray signal

For a long time, the $\ell = 12$ resonance has been the dominant cause of beam loss. Even after a careful realignment of the field coils, vacuum chamber, the injector, the supporting deck structures and reductions of other possible field errors, the $\ell = 12$ resonance remains significant. It is the first major resonance encountered as can be seen in Fig. 2.

The $\ell = 12$ resonance is of special interest because the NRL device has a twelve-fold periodicity. There are twelve sectors in the vacuum chamber and twelve toroidal field coils.

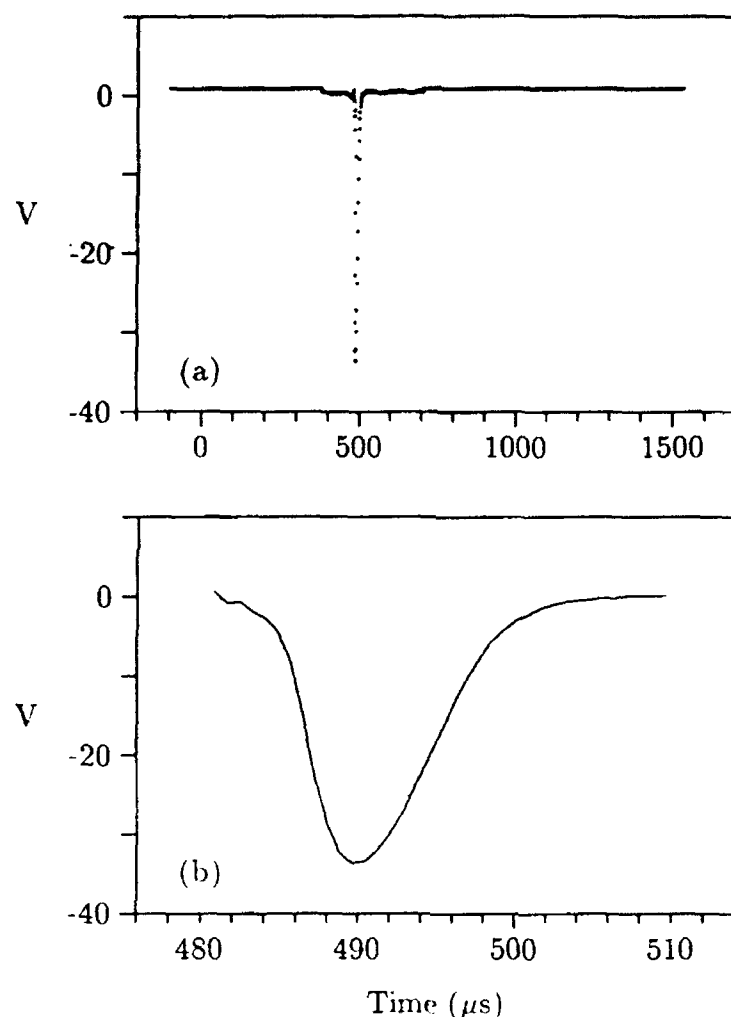


FIG. 3. X-ray signal when the resonant coils are activated at $\ell=12$. (a) Full trace; (b) Expanded trace.

To enhance this resonance, we have installed twelve resonant coils to generate a periodic field perturbation.

Initially, a set of twelve resonant coils was installed on the outside of the chamber (external coils). These coils are initiated at $\tau = 430 \mu\text{s}$, i.e., when the $\ell = 12$ condition is reached. A ΔB_θ pulse with a quarter period risetime of $12 \mu\text{s}$ and amplitude of 200 G is generated on the minor axis when the current in the coils is 9 kA . As it is apparent from Figs. 2 and 3(a), the width of the x-ray signal (a measure of rate of beam loss) is reduced from approximately $900 \mu\text{s}$ to $8 \mu\text{s}$, i.e., by more than two orders of magnitude while its amplitude has increased by a factor of twenty. The width of the x-ray signal varies inversely to the current in the resonant coils as shown in Fig. 4. The loss rate is also dependent on the risetime of the resonant coil pulse.

By connecting the coils in parallel instead of in series, the risetime was reduced to $5 \mu\text{s}$, and even shorter risetime pulses have been produced with a set of internal coils. The internal coils are powered by new drivers with a risetime of 400 ns . Being faster and nearer

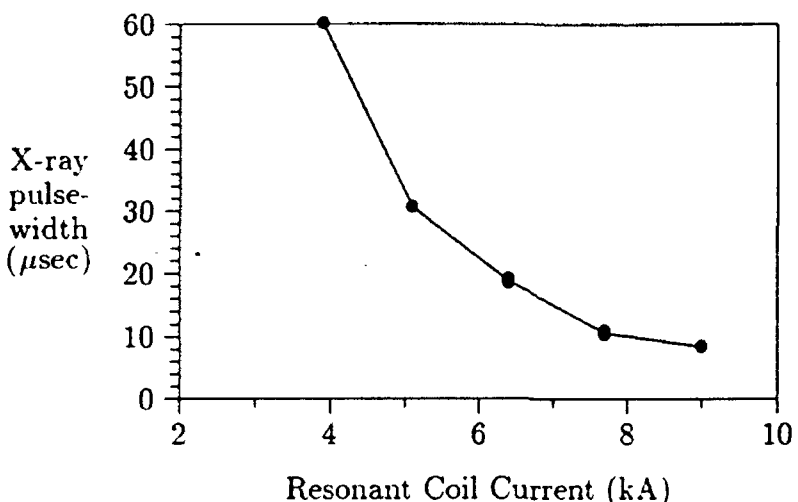


FIG. 4. Full width of the x-ray pulse at half-maximum versus the current in the resonant coils. The peak $\Delta B\theta$ generated in the chamber corresponds to 28 G/kA.

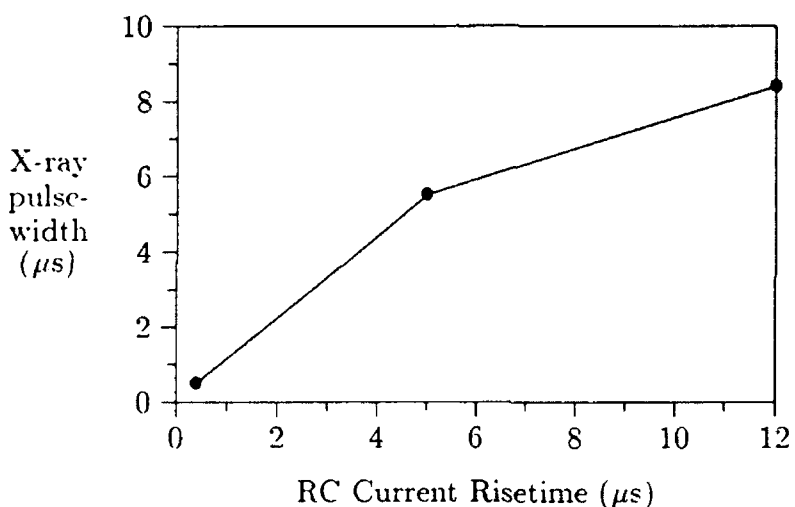


FIG. 5. Full width of the x-ray pulse at half maximum versus the current risetime of the resonant coils.

to the sector flanges, the internal coils require substantially higher voltage and current to produce the required field perturbations. The results from this experiment are shown in Fig. 5.

To determine the spatial distribution of beam losses when the resonant coils are energized, several 400- μ m-diameter optical fibers were mounted on the outside of the vacuum chamber. By the time the $\ell = 12$ resonance is crossed, the electrons have acquired sufficient energy to penetrate the chamber. The light generated when the electrons strike the fiber is monitored with a photomultiplier tube. The results from scanning around the torus at 10° intervals are shown in Fig. 6. Only six peaks instead of the expected twelve are observed. This is most likely due to the beating between the $\ell = 12$ and $\ell = 6$ mode that is excited by the six field periods of the stellarator windings. Computer simulation

shows that the strong focusing modulates the $\ell = 12$ peaks in such a way that only every other strikes the wall as shown in Fig. 7. It is still not clear at this time why three of the peaks are higher than the rest. Experiments are in progress to clarify this issue.

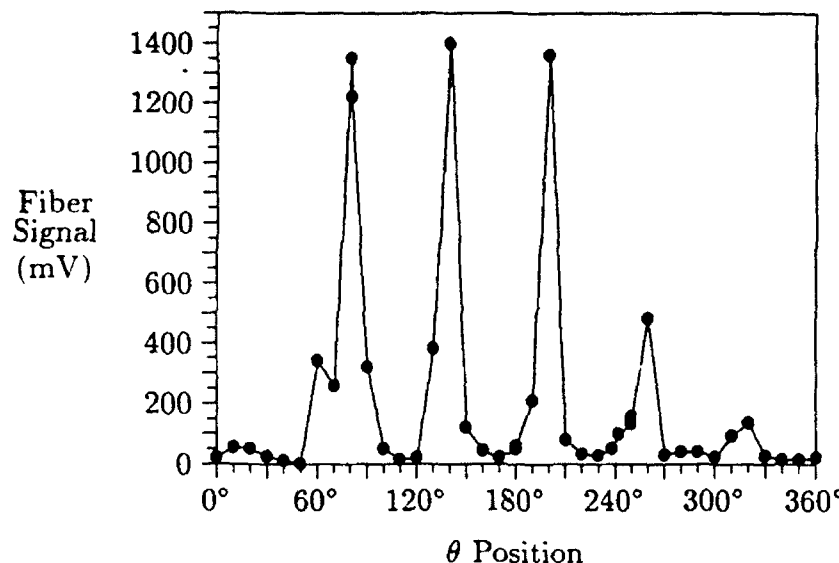


FIG. 6. Distribution of beam loss on the inner wall around the torus.

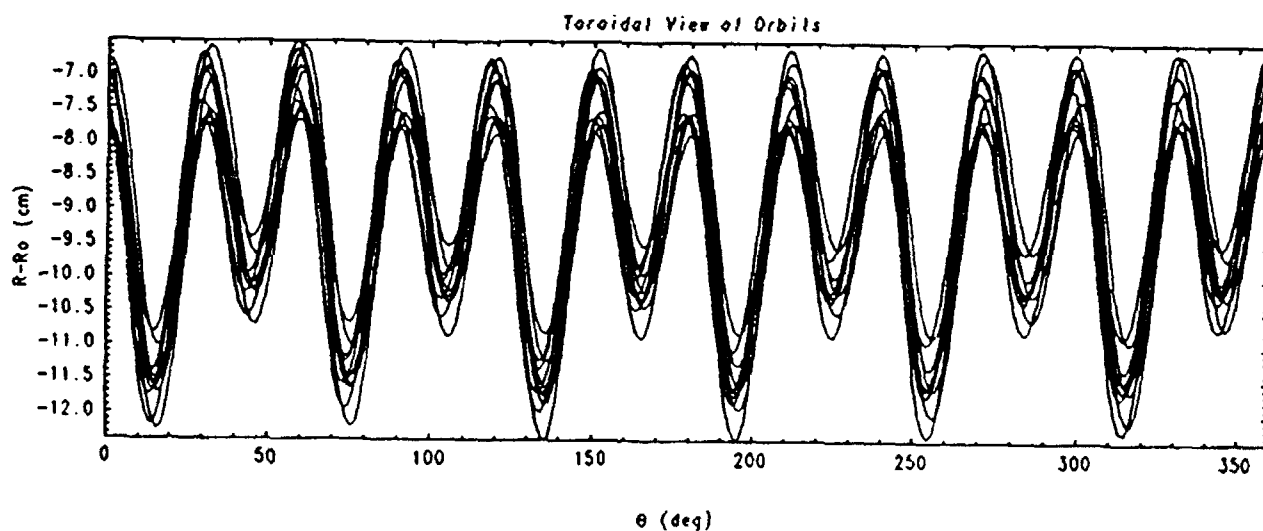


FIG. 7. Results from computer simulation. R_0 is the major radius.

Finally, we present the results from an experiment in which a time-rising ΔB_θ is used to extend the beam lifetime. It is well known that when $B_\theta/B_z = 2\ell^2/(2\ell-1) \approx \ell$ (= integer) (for the ℓ values relevant to our observation), resonances are excited and beam losses are observed. Therefore, by using an applied ΔB_θ to maintain $B_{\theta T}/B_z = \text{constant} \neq \text{integer}$,

where $B_{\theta T} = B_{\theta} + \Delta B_{\theta}$, crossing of resonances can be avoided. A set of 24 single-turn external coils, powered by a larger capacitor bank generates the ΔB_{θ} ramp. Results from the experiment are shown in Fig. 8 where the ΔB_{θ} was introduced at $\tau = 800 \mu\text{s}$. Beam loss is suppressed for 100 μs , which is the risetime of the applied B_{θ} .

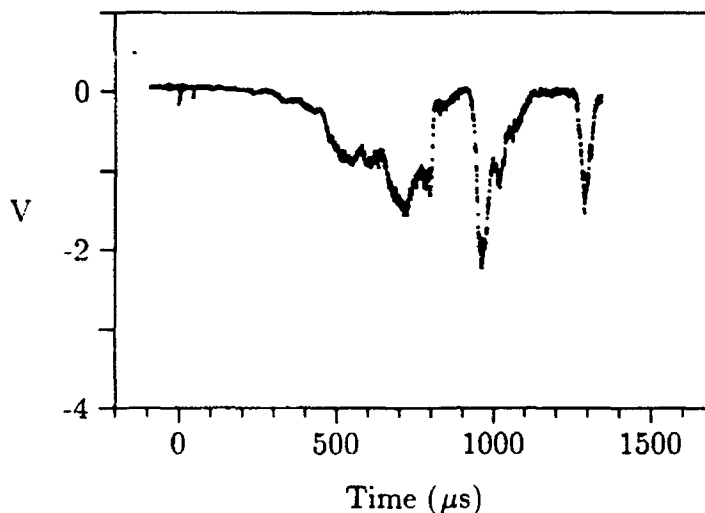


FIG. 8. X-ray signal for the case where a ΔB_{θ} has been added to extend the peak at 830 μs to 950 μs .

IV. REFERENCES

- * This work was supported by ONR and SPAWAR.
- a) Permanent address: FM Technologies, Inc., 10529-B Braddock Road, Fairfax, Virginia 22032.
- b) Permanent address: SFA, Inc., Landover, Maryland 20785.
- c) Permanent address: Science Applications International Corporation, 170 Goodridge Drive, McLean, Virginia 22102.
- d) Permanent address: Berkeley Research Associates, 5532 Hampstead Way, Springfield, Virginia 22151.
- ¹ C. A. Kapetanakos, L. K. Len, T. Smith, J. Golden, K. Smith, S. J. Marsh, D. Dialetis, J. Mathew, P. Loschialpo, and J. H. Chang, Phys. Rev. Lett. **64**, 2374 (1990).
- ² D. Chernin and P. Sprangle, Part. Accel. **12**, 101 (1982).
- ³ C. W. Roberson, A. Mondelli, and D. Chernin, Part. Accel. **17**, 79 (1985).
- ⁴ L. K. Len, T. Smith, J. Golden, K. Smith, S. J. Marsh, D. Dialetis, J. Mathew, P. Loschialpo, J. H. Chang, and C. A. Kapetanakos, *Intense Microwave and Particle Beams, SPIE*, **1226**, 382 (1990).
- ⁵ L. K. Len, T. Smith, J. Golden, S. J. Marsh, D. Dialetis, J. Mathew, P. Loschialpo, J. H. Chang, and C. A. Kapetanakos, *Proceedings of the 2nd European Particle Accelerator Conf.*, **1**, 446 (1990).
- ⁶ J. Golden, L. K. Len, T. J. Smith, D. Dialetis, S. J. Marsh, K. Smith, J. Mathew, P. Loschialpo, L. Seto, J. H. Chang, and C. A. Kapetanakos, *Intense Microwave and*

7 *Particle Beams II, SPIE, 1407, 418 (1991).*
C. A. Kapetanakos, D. Dialetis, S. J. Marsh, L. K. Len, and T. Smith, Phys. Rev. A,
44 (6), 3900 (1991).

Dynamic behavior of an electron ring close to a cyclotron resonance in a modified betatron accelerator

D. Dialetis,* S. J. Marsh,[†] and C. A. Kapetanakos

Plasma Physics Division, Naval Research Laboratory, Washington, D.C. 20375-5000

(Received 15 June 1992)

The effect on the electron-ring dynamics when a cyclotron resonance is crossed in a modified betatron accelerator has been studied analytically and numerically. It has been found that, in the presence of small vertical field errors, there is a field-error-amplitude threshold below which the normalized transverse velocity β_1 of the gyrating electrons is bounded (Fresnel regime) and above which it is unbounded (lock-in regime). In the lock-in regime, the average value of the normalized axial (toroidal) momentum $\gamma\beta_\theta$, where γ is the relativistic factor and β_θ is the normalized axial velocity, remains constant, i.e., the resonance is never crossed. In addition, above threshold, β_1 increases proportionally to the square root of the time. The threshold value of the vertical field error amplitude can be made larger either by increasing the acceleration rate or by adding a small oscillatory toroidal field to the main toroidal field. The multiple crossing of the same resonance, in the presence of such a small oscillatory toroidal field, was also studied with some interesting results.

PACS number(s): 41.75.Fr, 41.85.Lc, 29.27.Bd

I. INTRODUCTION

There is extensive experimental evidence suggesting that the gradual beam loss that is observed in the Naval Research Laboratory (NRL) modified betatron accelerator (MBA) is a consequence of crossing various cyclotron resonance modes during acceleration [1,2]. The cyclotron resonance is due to the excitation of the cyclotron motion by field errors associated with the toroidal and vertical magnetic fields. Consequently, these field errors can be either a vertical-field δB_z (VF) error or an axial-(toroidal) field δB_θ (TF) error or both.

Recirculating accelerators with low accelerating gradient such as the existing NRL modified betatron are sensitive to field errors, because the electrons have to perform a large number of revolutions around the major axis in order to obtain the desired peak energy. Successful detection and elimination or reduction of several field errors in the NRL device led to beam energies in excess of 20 MeV, while the trapped current is above 1 kA [3].

Although the cyclotron resonance is a potent mechanism with the potential to disturb the beam at a low acceleration rate and when the various fields are not carefully designed, it also may provide a powerful technique for extracting the beam from the magnetic-field configuration of the modified betatron [4]. The study of the cyclotron resonances is facilitated by introducing the detuning factor $w = r_0\Omega_{z0}/\gamma\beta_\theta c - l$, where r_0 is the major radius of the torus, c is the velocity of light, γ is the relativistic factor, β_θ is the normalized toroidal velocity, $\Omega_{z0} = |e|B_{z0}/mc$, B_{z0} is the toroidal magnetic field on the minor axis, e and m are the charge and mass of the electron, and l is the mode number of the resonance. The l mode of the cyclotron resonance occurs when the ratio of the toroidal field $B_{\theta0}$ to the vertical field B_{z0} is approximately equal to l . Since at equilibrium the ratio

$r_0\Omega_{z0}/\gamma\beta_\theta c$ is approximately unity, at least when the beam current is low and in the absence of strong focusing, the l -mode cyclotron resonance is crossed when the detuning factor is zero. Furthermore, the detuning factor appears naturally in the slow equations of motion derived by averaging out the fast cyclotron motion. The fact that $w + l$ is inversely proportional to $\gamma\beta_\theta$ has a profound effect on the ring dynamics. The quantity $\gamma\beta_\theta$ has a nonlinear dependence on the normalized perpendicular velocity β_1 , and, as a consequence, there is a threshold for the vertical field error amplitude below which β_1 is bounded (Fresnel regime) and above which β_1 increases continuously (lock-in regime) with time. In the lock-in regime, the detuning factor remains almost zero long after the resonance has been reached and, therefore, the resonance is never crossed. In addition, above threshold, β_1 increases proportionally to the square root of time while $\gamma\beta_\theta$ remains, on the average, a constant. The threshold value of the vertical field error amplitude can be made larger either by increasing the acceleration rate or by adding a small oscillatory toroidal field to the main toroidal field. The latter method is called dynamic stabilization of the resonance.

In the case of a vertical field error and in the absence of acceleration, space charge, and strong focusing field, our studies of the cyclotron resonances show that the normalized transverse velocity β_1 and thus the Larmor radius of the transverse motion of the gyrating particles grows linearly with time [5], provided that nonlinear effects associated with $\gamma\beta_\theta$ are neglected. When such effects are taken into account, β_1 is periodic and bounded.

As mentioned previously, in the presence of an accelerating field and of a large vertical field error, β_1 increases proportionally to the square root of time while $\gamma\beta_\theta$ saturates, i.e., the electrons lock into a specific resonance (lock-in regime). When the amplitude of δB_z is

below the threshold, β_1 exhibits Fresnel behavior, i.e., β_1 grows quickly for approximately 1 μ sec and then saturates until the beam reaches the next resonance.

In the case of an axial field error and in the absence of acceleration, when the ring is initially at exact resonance, β_1 grows exponentially with time only for a very short period. Since β_1 increases at the expense of β_0 , the particles are kicked off resonance and β_1 varies cyclicly with time. Similarly, in the presence of an accelerating field β_1 behaves as in the case of the vertical field error, i.e., below threshold it exhibits the Fresnel behavior and above threshold the ring locks into the resonance. The same is also true during acceleration even in the absence of a vertical or toroidal field error, but in the presence of stellarator fields of periodicity m , when the quasiequilibrium position of the ring is off the magnetic axis of the strong focusing system and the resonance mode is equal to m . The results of the studies with axial field error will be reported in a future publication. In the absence of a toroidal magnetic field, nonlinear effects associated with the crossing of resonances in synchrotrons have been considered previously by DePackh [6].

The preceding discussion is based on the assumption that the space charge is low and the strong focusing field is zero. In addition to introducing new characteristic modes, the strong focusing field makes the expression for the regular cyclotron mode more complicated [7]. However, it can be shown that for the parameters of the NRL device and provided $l \gg 1$, the strong focusing has only a minor effect on the cyclotron resonance. This conclusion is supported by extensive computer calculations.

This paper is organized as follows. The theoretical model is formulated in Sec. II. Section III A contains examples of both the Fresnel and lock-in state from the exact equations of motion. The slow equations of motion are derived in Sec. III B, and the simplified slow equations of motion with linearized detuning factor are given in Sec. III C. The asymptotic behavior in the Fresnel and lock-in state as well as the appropriate initial conditions to be used in the subsequent sections are presented in Sec. IV, while Sec. V contains a discussion of possible ways to cross a resonance without locking into it. Resonance diagrams for nonzero initial perpendicular velocity are displayed in Sec. VI, and the multiple crossing of the same resonance is demonstrated in Sec. VII. Finally, Sec. VIII contains the summary and conclusions.

II. MODEL WITH A VERTICAL-FIELD ERROR

Imperfections in the coils that generate the betatron field could result in a field error. A typical example is given in Fig. 1, which shows the VF error per kiloampere of the current circulating in the coils as a function of the toroidal angle, at $r = 100$ cm. This error is due to a small straight section in each coil that generates the betatron field in the vicinity of the power feeds. Table I provides the Fourier decomposition of the error. The values are the actual error amplitudes (in G) for a toroidal field $B_{\text{tor}} = 4650$ G as each particular resonance is reached during acceleration.

Obviously, near a resonance, only the mode associated with that resonance is acting on the ring. The contribu-

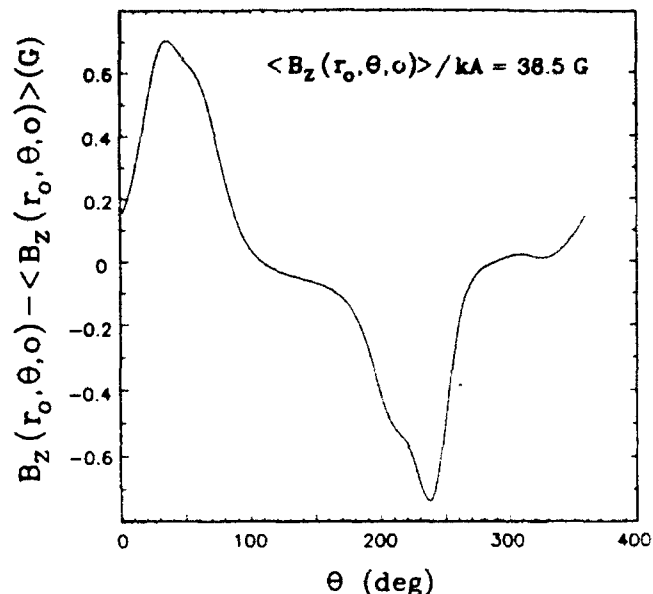


FIG. 1. Vertical field error per kiloampere of current in the coils that generate the betatron field, as a function of the toroidal angle θ , at $r = 100$ cm, $z = 0.0$ cm.

tion of all the other modes, being far away from the resonance, averages out to zero due to their fast oscillatory behavior. Therefore the VF error will be expressed in terms of the particular l mode associated with the resonance under study, i.e.,

$$\delta B_r = \delta B_{z0} K_{r0} \frac{r - r_0}{r_0} \sin(l\theta + \theta_0), \quad (1a)$$

$$\delta B_z = \delta B_{z0} \left[1 + K_{r0} \frac{r - r_0}{r_0} \right] \sin(l\theta + \theta_0), \quad (1b)$$

TABLE I. Fourier decomposition of VF error. Actual values of the VF error at each l mode for $B_{\text{tor}} = 4650$ G are listed.

Fourier mode	Fourier amplitude	cos (Fourier amplitude)	sin (Fourier amplitude)
1	108.2698	81.6151	71.1430
2	1.2152	0.3749	1.1559
3	8.8142	-6.5489	5.8994
4	0.9985	0.0905	0.9944
5	1.0148	-0.3835	-0.9395
6	0.5915	-0.5915	0.0000
7	0.3350	-0.0856	0.3238
8	0.3188	0.0884	-0.3063
9	0.3226	-0.2428	-0.2124
10	0.0759	0.0640	0.0407
11	0.1301	0.0868	-0.0970
12	0.0243	-0.0243	0.0000
13	0.0373	0.0264	0.0264
14	0.0112	0.0088	-0.0069
15	0.0062	-0.0045	0.0042
16	0.0034	0.0008	0.0033
17	0.0010	-0.0010	-0.0002
18	0.0012	-0.0012	0.0000
19	0.0002	-0.0002	0.0000
20	0.0000	0.0000	0.0000

$$\delta B_\theta = \delta B_{z0} \frac{z}{r_0} \cos(l\theta + \theta_0). \quad (1c)$$

In Eqs. (1), δB_{z0} , θ_0 , and K_{r0} are the amplitude, the phase, and the gradient in the radial direction of the l mode and r_0 is the major radius around which the analysis is carried out. It should be noticed that Eqs. (1a)–(1c) satisfy Maxwell's equations to first order in toroidal correlations.

The magnetic fields acting on the ring in the MBA are the betatron, the toroidal, and the stellarator field. For simplicity, the stellarator field is omitted in the present analysis. At high energies its contribution to the confinement of the ring is diminished and abundant computer runs have shown that the main results presented here are not altered in the presence of the stellarator field except for resonances $l=km$, where m is the field period of the stellarator and $k=1, 2, \dots$. In the analysis, the betatron field is approximated by

$$B_r^{(b)} = -n B_{z0} \frac{z}{r_0}, \quad (2a)$$

$$B_z^{(b)} = B_{z0} \left[1 - n \frac{r - r_0}{r_0} \right], \quad (2b)$$

where n is the field index and B_{z0} the field on the minor axis. Similarly, the toroidal magnetic field is given by

$$B_\theta = B_{\theta0} \frac{r_0}{r}, \quad (3)$$

where $B_{\theta0}$ is the field at $r=r_0$.

Since the VF error is a sinusoidal function of the toroidal angle θ , it is convenient to express the equations of motion in terms of the independent variable θ rather than time. In their transformed state, the equations of motion become

$$\begin{aligned} \xi'' + \left[i \frac{r_0 \Omega_{\theta0}}{\gamma \beta_\theta c} + \frac{1}{\gamma \beta_\theta} (\gamma \beta_\theta)' - \frac{1}{2} \frac{\xi' + \xi''}{1+P} \right] \xi' \\ = i \frac{r_0 (\Omega_r + i \Omega_z)}{\gamma \beta_\theta c} (1+P)^2 + 1+P, \end{aligned} \quad (4)$$

where the complex variable $\xi = [(r - r_0) + iz]/r_0$, $\xi' = d\xi/d\theta$, ξ'' is the complex conjugate of ξ' , and Ω is the cyclotron frequency, i.e., $\Omega = |e|B/mc$. The position of the ring centroid is given by

$$P \equiv \frac{r - r_0}{r_0} = \frac{1}{2}(\xi + \xi^*), \quad (5a)$$

$$Q \equiv \frac{z}{r_0} = \frac{1}{2i}(\xi - \xi^*). \quad (5b)$$

The quantity $\gamma \beta_\theta$ can be expressed as

$$\gamma \beta_\theta = \left[\frac{\gamma^2 - 1}{1 + \frac{1}{(1+P)^2} \xi' \xi''} \right]^{1/2}, \quad (6)$$

where γ is the relativistic factor and its derivative with respect to θ is equal to

$$\begin{aligned} \frac{1}{\gamma \beta_\theta} (\gamma \beta_\theta)' = & \frac{\gamma \gamma'}{(\gamma \beta_\theta)^2} - \frac{r_0 \Omega_z}{\gamma \beta_\theta c} \frac{1}{2i} (\xi' - \xi'') \\ & - \left[1 - \frac{r_0 \Omega_z}{\gamma \beta_\theta c} (1+P) \right] \frac{1}{2} \frac{\xi' + \xi''}{1+P}. \end{aligned} \quad (7)$$

The accelerating electric field is given by

$$E_\theta = -\frac{1}{c} r_0 \dot{B}_{z0}, \quad (8)$$

where \dot{B}_{z0} is the time derivative of the betatron field at $r=r_0$. Using the rate of change of time that is given by $t' = (r_0/c\beta_\theta)(1+P)$, it can be shown that

$$\gamma' = \left[\frac{r_0}{c} \right]^2 \dot{\Omega}_{z0} (1+P) \quad (9)$$

and

$$\Omega'_{z0} = \frac{r_0}{c} \dot{\Omega}_{z0} \frac{\gamma}{\gamma \beta_\theta} (1+P). \quad (10)$$

In the equations given above Ω_r and Ω_z include both the betatron field and the VF error. Notice that Eq. (4) is a second-order nonlinear differential equation of the complex quantity ξ . In terms of ξ , the position of the ring centroid is given by Eqs. (5), while its normalized velocity components v_r, v_z are

$$\beta_r + i\beta_z = \frac{\gamma \beta_\theta}{\gamma} \frac{1}{1+P} \xi'. \quad (11)$$

Obviously, the exact set of nonlinear equations given above is very complicated and difficult to handle. However, for a ring that has a bounce motion with a small amplitude, i.e., for small mismatch, and for large l -mode values, it is easy to show that near the resonance $|\xi| \approx |\xi'|/l$ and therefore $|\xi|$ is much smaller than $|\xi'|$. In this case, it is appropriate to linearize Eq. (4) with respect to ξ and ξ' . Under such conditions, Eq. (4) simplifies to

$$\xi'' + ib\xi' + K_1 \xi = f_1, \quad (12)$$

where

$$\begin{aligned} f_1 = \Delta + & \left[\frac{1}{2} (1+\Delta) (\xi' + \xi'') + ib\xi (\xi + \xi^*) - \frac{\gamma}{(\gamma \beta_\theta)_1} \gamma' - \frac{1}{2} (1-nC) (\xi \xi' + \xi^* \xi'') - \frac{1}{2} (\xi^* \xi' + \xi \xi'') \right] \xi' \\ & - K_2 \xi^* + \xi C (\xi + \xi^*) - \delta C [1 + \xi + (1+K_{r0}) \xi^* + \frac{1}{2} (\xi' + \xi'') \xi'] \sin(l\theta + \theta_0), \\ \frac{1}{(\gamma \beta_\theta)_1} = & \left[\frac{1 + \xi' \xi''}{\gamma^2 - 1} \right]^{1/2}, \end{aligned} \quad (13a)$$

$$b = \frac{r_0 \Omega_{z0}}{(\gamma \beta_\theta)_1 c}, \quad (13b)$$

$$C = \frac{r_0 \Omega_{z0}}{(\gamma \beta_\theta)_1 c}, \quad (13c)$$

$$\delta C = \frac{r_0 \delta \Omega_{z0}}{(\gamma \beta_\theta)_1 c}, \quad (13d)$$

$$\xi = \frac{1}{2} \frac{\xi \xi^*}{1 + \xi \xi^*}, \quad (13e)$$

$$\Delta = 1 - C, \quad (13f)$$

$$K_1 = C - \frac{1}{2}, \quad (13g)$$

$$K_2 = (1 - n)C - \frac{1}{2}. \quad (13h)$$

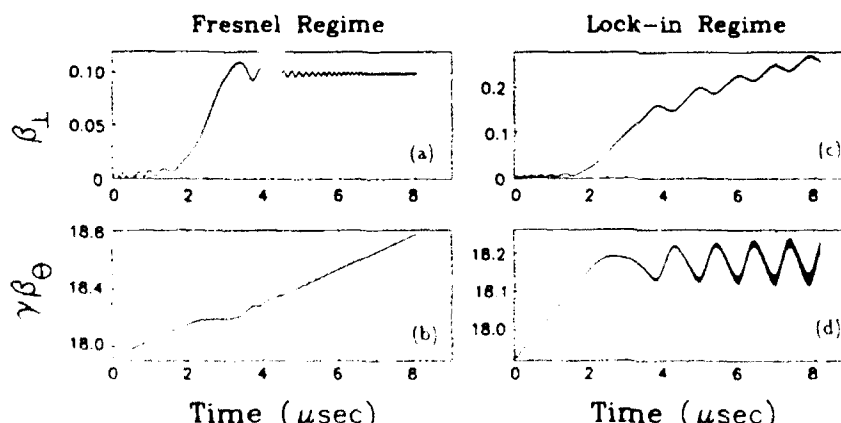
When the mismatch term Δ is small, then $C \approx 1$ and $K_2 \approx \frac{1}{2} - n$. Since the term $K_2 \xi^*$ in f_1 will be treated as a perturbation in the derivation of the slow equations of motion, K_2 must be small. Therefore we assume that n is close to $\frac{1}{2}$. Also, since we consider only values of $|\xi| < 0.2$, before the resonance is crossed, terms proportional to $|\xi|^2 |\xi|$ are omitted when compared to one. The simplified Eq. (12) is complemented by the derivatives with respect to θ of γ and $r_0 \Omega_{z0}/c$, which are given by

$$\gamma' = \left[\frac{r_0}{c} \right]^2 \dot{\Omega}_{z0} \left[1 + \frac{\xi + \xi^*}{2} \right] \quad (14a)$$

and

$$\frac{r_0 \Omega'_{z0}}{c} = \left[\frac{r_0}{c} \right]^2 \dot{\Omega}_{z0} \frac{\gamma}{(\gamma \beta_\theta)_1} \left[1 + \frac{\xi + \xi^*}{2} \right]. \quad (14b)$$

Results from the numerical integration of Eq. (12) and the exact Eq. (4) are in very good agreement, provided the initial values of $|\xi| < 0.30 \times 10^{-2}$ and $|\xi| < 0.2$. Therefore Eq. (12) will be used in the derivation of the slow equations by averaging out the fast cyclotron oscillatory motion.



III. DYNAMIC BEHAVIOR NEAR A RESONANCE: FRESNEL AND LOCK-IN REGIMES

A. Numerical results from the exact equations

The results from the numerical integration of the exact equations of motion, i.e., Eq. (4), as a resonance is crossed during acceleration indicate the following consistent behavior: there is a threshold value of the VF error amplitude δB_{z0} , below which the perpendicular velocity β_1 of the gyrating electrons increases by a certain amount as the resonance is crossed and then it remains relatively constant, after the resonance has been crossed. Above the threshold value, β_1 keeps increasing with time while $\gamma \beta_\theta$ remains, on the average, constant, and the resonance is never crossed, i.e., the ring is locked into the resonance. A typical example of this behavior is shown in Fig. 2 for the parameters listed in Table II. The threshold value of δB_{z0} is between 0.19 and 0.195 G. Figures 2(a) and 2(c) show β_1 versus time below and above threshold, while Figs. 2(b) and 2(d) show the corresponding $\gamma \beta_\theta$ versus time.

It is rather difficult to find from the exact equations of motion the source of the dynamic behavior shown in Fig. 2. This behavior can be explained by the slow equations of motion derived in Sec. III B.

To derive the slow equations of motion the instantane-

FIG. 2. β_1 and $\gamma \beta_\theta$ vs time obtained from the exact equations of motion [Eq. (4)], in the Fresnel and lock-in regimes and close to the threshold, for the parameters in Table II.

TABLE II. Parameters of the runs shown in Figs. 2-6.

Parameter	Value
Torus major radius r_0	100 cm
Toroidal magnetic field $B_{\phi 0}$	2771 G
Vertical magnetic field B_{z0}	305 G
Field index n	0.5
Rate of change of vertical field \dot{B}_{z0}	2 G/μsec
Resonance mode l	9
Amplitude of VF error δB_{z0}	0.190, 0.195 G
Constant phase of VF error θ_0	0.0
Gradient of VF error K_{z0}	0.0
Initial normalized toroidal momentum $\gamma\beta_\theta$	17.922
Initial normalized vertical velocity β_1	0.0
Initial phase of vertical velocity ϕ_0	0.0
Initial radial displacement $r - r_0$	0.0 cm
Initial vertical displacement z	0.0 cm
Integration time t_f	8 μsec

ous position of the particle ξ is decomposed into two components. The first is associated with the bounce motion and the second with the cyclotron or fast motion, i.e., $\xi = \xi_b + \xi_c$, where $\xi_b = \xi_b^{(s)} \exp(-i\nu_b \theta)$, $\xi_c = \xi_c^{(s)} \exp(-i\nu_c \theta)$, and ν_b and ν_c are the two characteristic frequencies of the system. Specifically, $\nu_b = \nu_-$ and $\nu_c = \nu_+$, where

$$\nu_{\pm} = \frac{b}{2} \pm \left[\left(\frac{b}{2} \right)^2 + K_1 \right]^{1/2}. \quad (15)$$

The complex amplitudes $\xi_b^{(s)}$ and $\xi_c^{(s)}$ are, in general, slowly varying quantities, provided that the perturbation is not very large. Since these two amplitudes vary slowly, the corresponding derivatives with respect to θ are equal to $\xi'_b = -i\nu_b \xi_b$ and $\xi'_c = V_c^{(s)} \exp[-(l\theta + \theta_0)]$, provided that $\nu_c \approx l$. The amplitude $V_c^{(s)}$ is a slowly varying quantity because $\xi_c^{(s)}$ has been expressed in a frame that rotates with angular velocity lc/r_0 . As a consequence of $|V_c^{(s)}| \ll |\xi'|$, the position of the cyclotron mode is given by $\xi_c \approx -(1/i\nu_c) V_c^{(s)} \exp[-i(l\theta + \theta_0)]$.

From the previous discussion, the complex position ξ and its derivative ξ' can be expressed as follows:

$$\xi = \xi_b - (1/i\nu_c) V_c^{(s)} e^{-i(l\theta + \theta_0)} \quad (16a)$$

and

$$\xi' = -i\nu_b \xi_b + V_c^{(s)} e^{-i(l\theta + \theta_0)}. \quad (16b)$$

It is apparent from Eqs. (16) that it is possible to extract the bounce and (slow) cyclotron motion in the rotating frame by inverting Eqs. (16). Specifically,

$$\xi_b = \frac{\nu_c}{\nu_c - \nu_b} \left[\xi - \frac{i}{\nu_c} \xi' \right] \quad (17a)$$

and

$$V_c^{(s)} = \frac{\nu_c}{\nu_c - \nu_b} (i\nu_b \xi_b + \xi') e^{i(l\theta + \theta_0)}. \quad (17b)$$

Figures 3(a) and 3(b) show the real and imaginary components of $\beta_\theta V_c^{(s)}$ for the parameters listed in Table II. For these same parameters, the actual orbit in the r - z plane, during the first 2 μsec, is given in Fig. 4(a), while Fig. 4(b) gives the bounce motion associated with the actual orbit, as computed from Eq. (17a).

B. Slow equations of motion

The method that is used in this section to obtain the equations of motion of the slowly varying quantities asso-

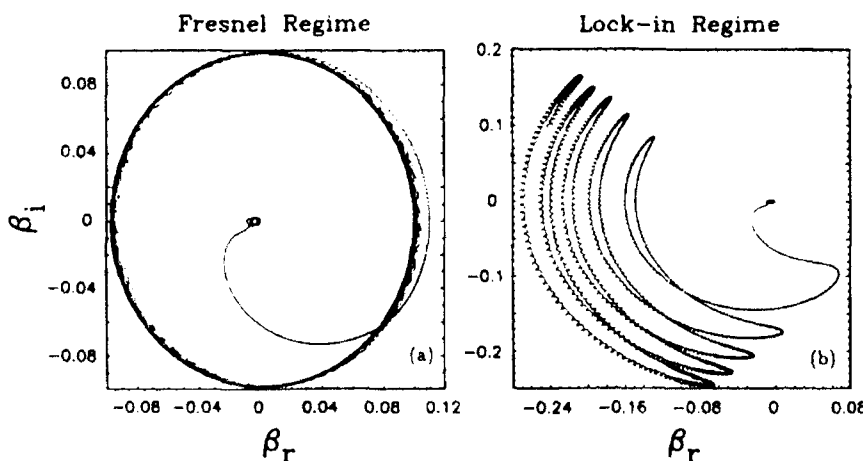


FIG. 3. Normalized perpendicular velocity in velocity space and in the rotating frame [Eq. (17b)] obtained from the exact equations of motion in the Fresnel and lock-in regimes (for the same parameters as in Fig. 2).

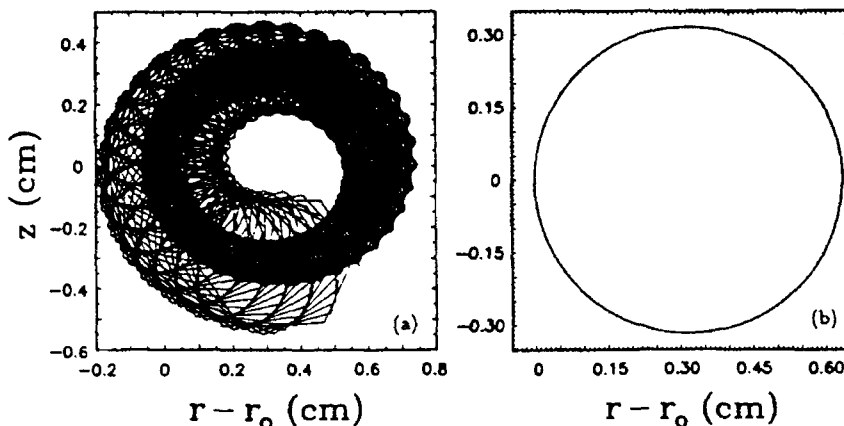


FIG. 4. (a) Exact orbit and (b) bounce motion orbit obtained from the exact equations of motion during the first 2 μ sec, and for the same parameters as in Figs. 2 and 3.

ciated with the cyclotron and bounce motions has been devised by Bogoliubov and Mitropolsky [8] and is a perturbation approach to the problem. Before this method can be applied, the simplified Eq. (12) should be written in a suitable form. For this purpose we express ξ, ξ' in terms of the quantities ξ_b, V_c as follows:

$$\xi = \xi_b + \frac{i}{v_+} V_c, \quad (18a)$$

$$\xi' = -i v_- \xi_b + V_c, \quad (18b)$$

where

$$v_{\pm} = \frac{b_0}{2} \pm \left[\left(\frac{b_0}{2} \right)^2 + K_{10} \right]^{1/2}, \quad (19a)$$

$$b_0 = \frac{r_0 \Omega_{00}}{(\gamma \beta_{\theta})_0 c}, \quad (19b)$$

$$C_0 = \frac{r_0 \Omega_{z0}}{(\gamma \beta_{\theta})_0 c}, \quad (19c)$$

$$K_{10} = C_0 - \frac{1}{2}, \quad (19d)$$

$$\frac{1}{(\gamma \beta_{\theta})_0} = \left[\frac{1 + |V_0|^2}{\gamma^2 - 1} \right]^{1/2}, \quad (19e)$$

In Eq. (19e), V_0 is the zero order, slowly varying quantity associated with V_c [see Eq. (26a)]. In addition, v_{\pm} are definitely slowly varying quantities, since they depend on $|V_0|^2$.

The equations of motion of V_c and ξ_b are

$$V'_c + i v_+ V_c = \frac{v_+}{v_+ - v_-} \left[f + \delta f + i v_- \xi_b - \frac{v'_+}{v_+} \frac{v_-}{v_+} V_c \right], \quad (20a)$$

$$\xi'_b + i v_- \xi_b = -\frac{i}{v_+ - v_-} \left[f + \delta f + i v'_- \xi_b - \frac{v'_+}{v_+} V_c \right], \quad (20b)$$

where

$$f = \Delta_0 + \frac{1}{2} (1 + \Delta_0) (\xi' + \xi^{*'}) \xi' - \delta C_0 \sin(I\theta + \theta_0), \quad (21a)$$

$$\delta f = \Delta - \Delta_0 + \left[-i(b - b_0) + \frac{1}{2} (\Delta - \Delta_0) (\xi' + \xi^{*'}) + i b \xi (\xi + \xi^*) - \frac{\gamma}{(\gamma \beta_{\theta})_1^2} \gamma' - \frac{1}{2} (1 - nC) (\xi \xi' + \xi^* \xi^{*'}) - \frac{1}{2} (\xi^* \xi' + \xi \xi^{*'}) \right] \xi' - (K_1 - K_{10}) \xi - K_2 \xi^* + \xi C (\xi + \xi^*) - \delta C [\xi + (1 + K_{r0}) \xi^* + \frac{1}{2} (\xi' + \xi^{*'}) \xi'] \sin(I\theta + \theta_0) - (\delta C - \delta C_0) \sin(I\theta + \theta_0). \quad (21b)$$

$$\Delta_0 = 1 - C_0, \quad (22a)$$

$$\delta C_0 = \frac{r_0 \delta \Omega_{z0}}{(\gamma \beta_{\theta})_0 c}, \quad (22b)$$

and b_0, C_0, K_{10} have already been defined.

To implement the perturbation theory, we introduce the parameter ϵ , which indicates the relative smallness of the various terms. In terms of ϵ , Eqs. (20) can be written as follows:

$$V'_c + i l V_c = \epsilon [f_c - i(v_+ - l)V_c], \quad (23a)$$

$$\xi'_b + i \epsilon v_- \xi_b = \epsilon f_b, \quad (23b)$$

where

$$f_c = \frac{v_+}{v_+ - v_-} [f + \delta f], \quad (24a)$$

$$f_b = -\frac{i}{v_+ - v_-} [f + \delta f]. \quad (24b)$$

Assuming that the field error $\delta B_{z0} \ll B_{z0}$, $|\Delta_0| \ll 1$, and since $l \gg |V_0|$ and $v_+ \approx l$, the right-hand side of Eqs. (23) is at least of order ϵ . In addition, since $|v_-| \ll 1$, the term $i v_- \xi_b$ in Eq. (23b) is of order ϵ . The terms that are proportional to the derivatives of v_\pm have been omitted because they are of higher order.

Furthermore, for high l -mode numbers $|\xi| \ll |\xi'|$ and in light of Eqs. (18), in terms of ϵ , ξ and ξ' can be written as follows:

$$\xi = \epsilon \left[\xi_b + \frac{i}{v_+} V_c \right], \quad (25a)$$

$$\xi' = -i v_- \xi_b \epsilon + V_c. \quad (25b)$$

The perturbation method is applied on Eqs. (23) and (25) by setting

$$V_c = V_0 e^{-i(l\theta + \theta_0)} + \epsilon V_1(\xi_0, \xi_0^*, V_0, V_0^*, \theta) + \dots, \quad (26a)$$

$$\xi_b = \xi_0 + \epsilon \xi_1(\xi_0, \xi_0^*, V_0, V_0^*, \theta) + \dots, \quad (26b)$$

$$V'_0 = \epsilon A_1(\xi_0, \xi_0^*, V_0, V_0^*) + \epsilon^2 A_2(\xi_0, \xi_0^*, V_0, V_0^*) + \dots, \quad (26c)$$

$$\xi'_0 = \epsilon B_1(\xi_0, \xi_0^*, V_0, V_0^*) + \epsilon^2 B_2(\xi_0, \xi_0^*, V_0, V_0^*) + \dots, \quad (26d)$$

where V_0, ξ_0 are the slowly varying quantities associated with V_c, ξ_b , respectively. Then, the slowly varying quantities A_1, A_2, \dots and B_1, B_2, \dots are determined by inserting the equations above into Eqs. (23) and eliminating the terms that lead to secular terms for each order of the perturbation parameter ϵ .

The computation is carried out to second order in ϵ and it is tedious but straightforward and will not be given here. To that order, the quantities V_1, ξ_1 , are equal to

$$V_1 = \frac{v_+}{v_+ - v_-} \frac{1}{il} \left[\Delta_0 + \frac{1}{2}(1 + \Delta_0) |V_0|^2 + \frac{i}{4} \delta C_0 e^{i(l\theta + \theta_0)} \right. \\ \left. - \frac{1}{2}(1 + \Delta_0) V_0^2 e^{-2i(l\theta + \theta_0)} \right], \quad (27a)$$

$$\xi_1 = -\frac{i}{v_+ - v_-} \frac{1}{2l} \left[\delta C_0 e^{-i(l\theta + \theta_0)} + \delta C_0 e^{i(l\theta + \theta_0)} \right. \\ \left. + \frac{i}{2}(1 + \Delta_0) V_0^2 e^{-2i(l\theta + \theta_0)} \right]. \quad (27b)$$

Also, to second order in ϵ , the slow equations for V_0 and ξ_0 are

$$V'_0 + i(v_+ - l)V_0 = f_c^{(s)}. \quad (28a)$$

and

$$\xi'_0 + i v_- \xi_0 = f_b^{(s)}, \quad (28b)$$

where

$$f_c^{(s)} = i \frac{v_+}{v_+ - v_-} \left\{ i \frac{\gamma \gamma'}{(\gamma \beta_\theta)_0^2} V_0 - v_- \xi_0 V_0 + b_0 \xi_0 (\xi_0 + \xi_0^*) V_0 - \left[\Delta_0 + \frac{\xi_0 C_0}{2} \right] v_- (\xi_0 - \xi_0^*) V_0 \right. \\ \left. + \frac{C_0}{2v_+} [\xi_0 (1 - |V_0|^2) - \Delta_0 (1 + 2\xi_0 - \Delta_0 (1 + \frac{1}{2}|V_0|^2))] V_0 \right. \\ \left. - \frac{\delta C_0}{2} \left[1 + \xi_0 + (1 + K_{r0}) \xi_0^* + \frac{1}{2}|V_0|^2 - \frac{1}{2}V_0^2 - \frac{\delta C_0}{8v_+} \frac{1}{1 + |V_0|^2} V_0 \right] \right\}, \quad (29a)$$

and

$$f_b^{(s)} = -\frac{i}{v_+ - v_-} \left\{ \Delta_0 + \frac{1}{2}|V_0|^2 - (b_0 v_- + \Delta_0 + |V_0|^2) \xi_0 \xi_0^* - \left[K_{20} - \frac{n C_0}{2} |V_0|^2 + (\Delta_0 + |V_0|^2) \xi_0 \right] \xi_0^* \right. \\ \left. - \frac{\delta C_0}{2v_+} \left[\left[1 + \frac{1}{2}\Delta_0 + \xi_0 - \frac{1}{2} \frac{K_{10}\xi_0}{1 + |V_0|^2} \right] (V_0 + V_0^*) + K_{r0} V_0^* - \frac{\delta C_0}{4} \xi_0 V_0 \right] \right\}. \quad (29b)$$

The quantities for ξ_0 and K_{20} are given in Eqs. (13e) and (13h) with $|\xi'|^2$ replaced by $|V_0|^2$ and C replaced by C_0 . The slow Eqs. (28) and (29) should be complemented by the derivatives of γ and $r_0 \Omega_{z0}/c$. Keeping only the zero order nonoscillatory parts in Eqs. (14a) and (14b), we obtain

$$\gamma' \approx \left[\frac{r_0}{c} \right]^2 \dot{\Omega}_{z0} \left[1 + \frac{\xi_0 + \xi_0^*}{2} \right] \quad (30)$$

and

$$\frac{r_0 \Omega'_{z0}}{c} \approx \left[\frac{r_0}{c} \right]^2 \dot{\Omega}_{z0} \frac{\gamma}{(\gamma \beta_\theta)_0} \left[1 + \frac{\xi_0 + \xi_0^*}{2} \right]. \quad (31)$$

Solutions of the slow equations are shown in Fig. 5 for the same input parameters (see Table II) used in the solution of the exact Eq. (4). Figures 5(a) and 5(c) show the zero order $\beta_1^{(0)} \equiv (\gamma \beta_\theta)_0 |V_0| / \gamma$ versus time, below and

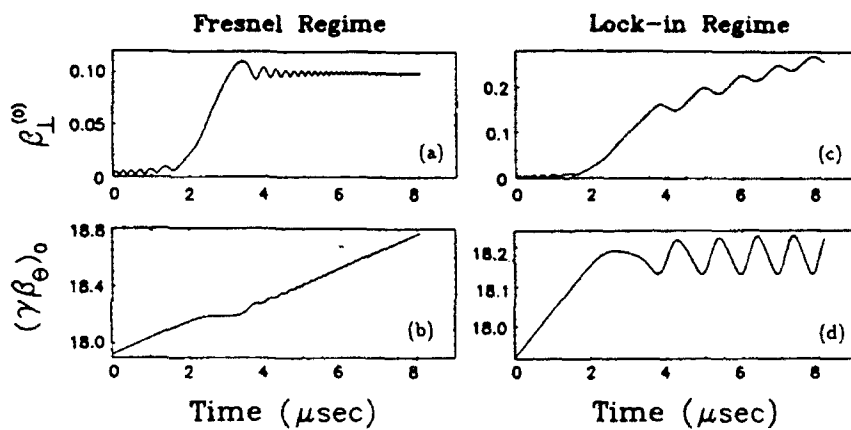


FIG. 5. β_1 and $\gamma\beta_0$ vs time obtained from the slow equations of motion [Eqs. (28) and (29)], in the Fresnel and lock-in regimes and close to the threshold, for the parameters in Table II.

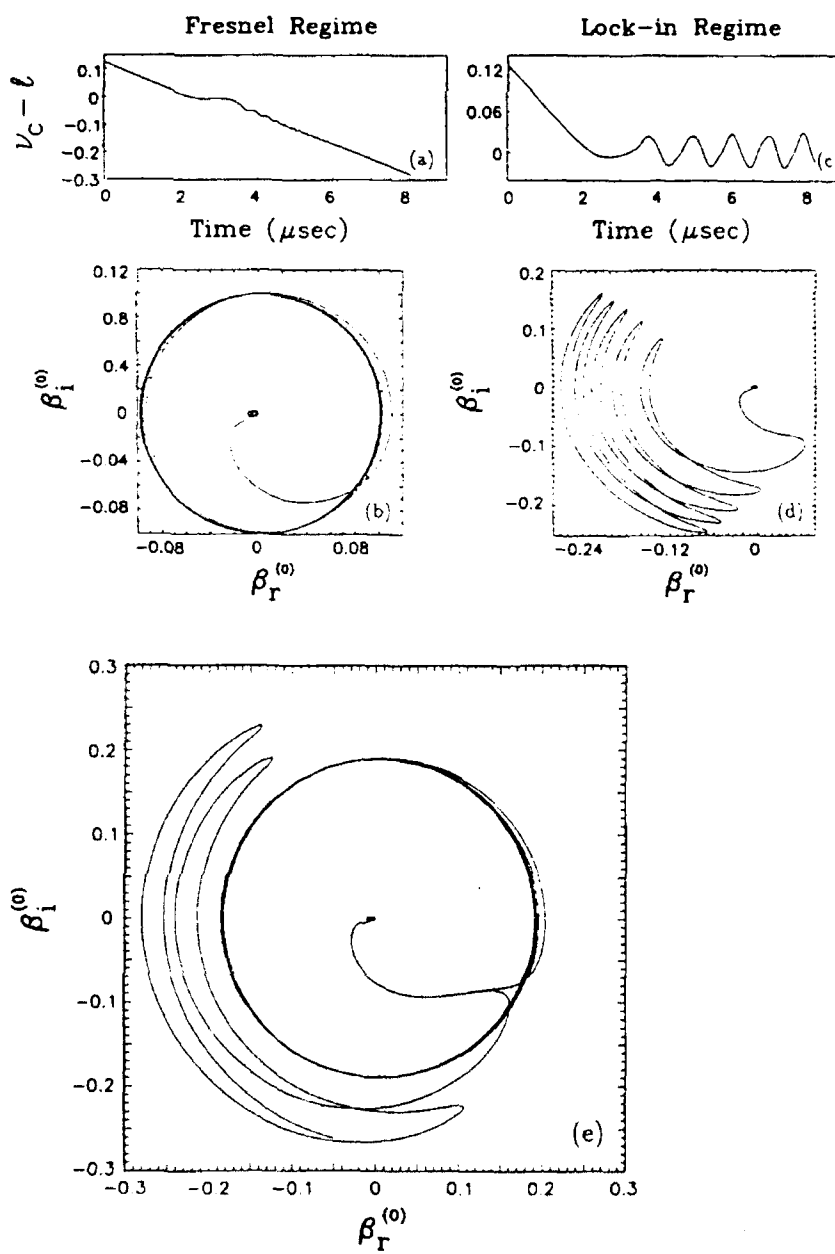


FIG. 6. Detuning factor vs time and normalized perpendicular velocity in velocity space obtained from the slow equations of motion in the Fresnel and lock-in regimes (for the same parameters as in Fig. 5).

above threshold, while Figs. 5(b) and 5(d) show the corresponding zero order $(\gamma\beta_\theta)_0$ versus time. Figure 6 shows the detuning factor $w = v_c - l$ and the real and imaginary parts of $(\gamma\beta_\theta)_0 V_0 / \gamma$, below and above threshold. By comparing Figs. 5 and 6 to Figs. 2 and 3 it is apparent that the slow equations predict accurately β_1 and $\gamma\beta_\theta$, when the initial perpendicular velocity is zero. Above threshold the detuning factor locks into the resonance, with only a small variation around zero. A plot of ξ_0 is not given, since it is exactly the same as that in Fig. 4(b). Obviously, the numerical integration of the slow equations is much faster than that of the exact Eq. (4) or (12), since the oscillatory terms have been averaged out.

C. Slow equations of motion with linearized detuning factor

The slow equations of Sec. III B are still too lengthy to provide insight into the origin of the threshold behavior. When $\delta B_{z0} |V_0| / l B_{z0} \ll 1$, the last term in Eq. (29b) can be neglected and the equation for the bounce motion simplifies to the equation

$$\begin{aligned} \xi'_0 + i v_- \left[1 + \frac{1}{K_{10}} (b_0 v_- + \Delta_0 + |V_0|^2) \right] \xi_0 \\ + i \frac{v_-}{K_{10}} \left[K_{20} - \frac{nC_0}{2} |V_0|^2 + (\Delta_0 + |V_0|^2) \xi_0 \right] \xi_0^* \\ = i \frac{v_-}{K_{10}} (\Delta_0 + \frac{1}{2} |V_0|^2), \quad (32) \end{aligned}$$

where we have used the fact that $|v_-| \ll v_+$, and the relation $v_- v_+ = -K_{10}$. Equation (32) indicates that the equilibrium position of the bounce motion is proportional to the generalized mismatch $\Delta_0 + \frac{1}{2} |V_0|^2$. Without exception the computer runs have shown that during the crossing of the resonance the equilibrium position of the bounce motion hardly changes when the gradient factor $K_{10} = 0$. That is not the case when $K_{10} \neq 0$. Therefore, if both the initial mismatch and the initial bounce position ξ_0 are zero, the latter quantity remains very small. Under these conditions, the slow equation for V_0 simplifies to the equation

$$\begin{aligned} V'_0 + i \left[v_+ - l + \frac{C_0}{2v_+} (\Delta_0 - \frac{1}{2} |V_0|^2) \right] V_0 \\ = i \left[i \frac{\gamma\gamma'}{(\gamma\beta_\theta)_0^2} V_0 - \frac{\delta C_0}{2} (1 + \frac{1}{2} |V_0|^2 - \frac{1}{2} V_0^2) \right], \quad (33) \end{aligned}$$

where terms proportional to Δ_0^2 , $|V_0|^4$, and $\Delta_0 |V_0|^2$ or higher have been omitted.

To simplify further Eq. (33), it is convenient to introduce the quantity U_0 by means of the relation

$$V_0 = \frac{U_0}{[\gamma^2 - 1 - |U_0|^2]^{1/2}}. \quad (34)$$

Since, to zero order, V_0 is equal to $[(\beta_1 + i\beta_2)/\beta_\theta] \exp[i(l\theta + \theta_0)]$, U_0 is, to the same order, equal to $\gamma(\beta_1 + i\beta_2) \exp[i(l\theta + \theta_0)]$, and it is easy to show

from Eqs. (19e) and (34) that

$$(\gamma\beta_\theta)_0 = [\gamma^2 - 1 - |U_0|^2]^{1/2}. \quad (35)$$

A straightforward transformation of Eq. (33) from the V_0 to the U_0 variable leads to the slow equation for U_0 , namely

$$U'_0 + i \left[v_+ - l + \frac{C_0}{2v_+} \left[\Delta_0 - \frac{1}{2} \frac{|U_0|^2}{(\gamma\beta_\theta)_0^2} \right] \right] U_0 = -iB_0, \quad (36)$$

where

$$B_0 = \frac{1}{2} \frac{r_0 \delta \Omega_{z0}}{c}. \quad (37)$$

Equation (36) indicates that the detuning factor $w = v_+ - l$ should be redefined by adding to it the small correction term

$$C_0 \left[\Delta_0 - \frac{1}{2} \frac{|U_0|^2}{(\gamma\beta_\theta)_0^2} \right] / 2v_+.$$

Above threshold, the small correction term is important because it compensates for the small time-dependent contribution of K_{10} in v_+ [cf. Eq. (19a)]. If the small correction term is omitted in either Eq. (36) or (33), then, above threshold, the average value of $(\gamma\beta_\theta)_0$ does not remain constant but increases with θ . This is contrary to the solution of either Eqs. (28) and (29) or the exact Eq. (4) or (12).

When the mismatch $\Delta_0 + \frac{1}{2} |V_0|^2 \approx 0$ and the initial ξ_0 is also zero, then $\xi_0 \approx 0$ and the relativistic factor γ is equal to $\gamma = \gamma_0 + \gamma' \theta$ [cf. Eq. (30)], where γ_0 and γ' are the initial values of γ and the acceleration rate [assumed to be a constant, and given by Eq. (30) with $\xi_0 = 0$], respectively. Assuming that $\gamma' \theta \ll \gamma_0$ and $||U_0|^2 - |U_{00}|^2| \ll 1$, where U_{00} is the initial value of U_0 , the detuning factor can be linearized with respect to $\gamma' \theta$ and $|U_0|^2 - |U_{00}|^2$, namely

$$w = w_0 - \alpha \theta + \frac{1}{2} \delta [|U_0|^2 - |U_{00}|^2], \quad (38)$$

where

$$w_0 = v_{+0} - l + \frac{C_{00}}{2v_{+0}} \left[\Delta_{00} - \frac{1}{2} \frac{|U_{00}|^2}{(\gamma\beta_\theta)_{00}^2} \right], \quad (39a)$$

$$\alpha = v_{+1} \frac{\gamma_0 \gamma'}{(\gamma\beta_\theta)_{00}^2}, \quad (39b)$$

$$\delta = v_{+1} \frac{1}{(\gamma\beta_\theta)_{00}^2}, \quad (39c)$$

$$v_{+1} = \frac{b_{00}}{2} \left[1 + \frac{\frac{b_{00}}{2}}{\left[\left(\frac{b_{00}}{2} \right)^2 + K_{100} \right]^{1/2}} \right], \quad (39d)$$

$$(\gamma\beta_\theta)_{00} = [\gamma_0^2 - 1 - |U_{00}|^2]^{1/2}, \quad (39e)$$

and $v_{+0}, b_{00}, c_{00}, \Delta_{00}, K_{100}$ are the initial values of $v_+, b_0, c_0, \Delta_0, K_{10}$, respectively. The dependence of K_{10}

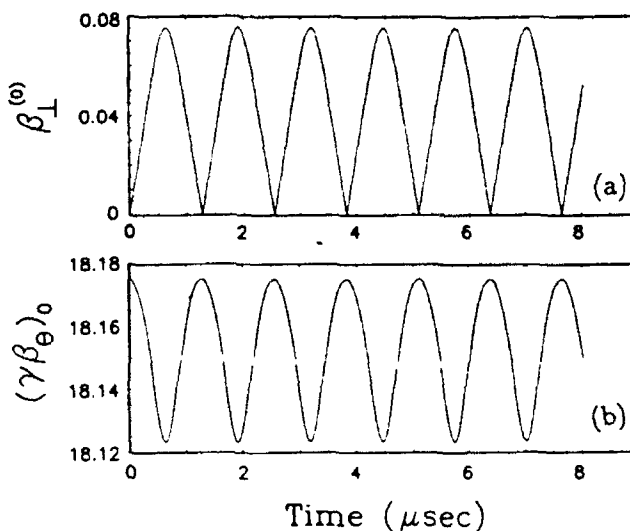


FIG. 7. β_1 and $\gamma\beta_\theta$ vs time obtained from the slow equations of motion without acceleration, for the parameters in Table III.

on θ and on $(\gamma\beta_\theta)_0$ has been neglected, since v_+ is weakly dependent on K_{10} when $b_0 \approx l \gg 1$. Also, since $\Delta_0 \approx -\frac{1}{2}|U_0|^2/(\gamma\beta_\theta)_0^2$, $C_0 \approx 1$, and $\delta \approx l/(\gamma\beta_\theta)_0^2$, the small correction term that is added to the detuning factor in Eq. (36) provides such a small contribution to δ , of order $1/l^2$, that it has been neglected. Therefore the slow equation for U_0 with linearized detuning factor is

$$U'_0 + i[\omega_0 - \alpha\theta + \frac{1}{2}\delta(|U_0|^2 - |U_{00}|^2)]U_0 = -iB_0 \quad (40)$$

This equation predicts the same temporal behavior for β_1 and $\gamma\beta_\theta$ as the original slow Eqs. (28) and (29). The cause of this behavior is the nonlinear term proportional to $|U_0|^2 - |U_{00}|^2$ (it will be shown shortly that when $\delta=0$, the solution is the Fresnel integral, which is bounded). We conclude that the existence of the Fresnel and lock-in regimes in the exact Eq. (4) or in Eq. (12) is due to the dependence of the term $r_0\Omega_{\theta 0}/\gamma\beta_\theta c$ upon $\gamma\beta_\theta$ and the fact that $\gamma\beta_\theta$ depends nonlinearly on the perpendicular velocity.

It is interesting to examine the case when there is no acceleration ($\alpha=0$), the particles are at exact resonance ($\omega_0=0$) and the initial perpendicular velocity is zero ($|U_{00}|^2=0$). Then Eq. (40) becomes

$$U'_0 + i\frac{1}{2}\delta|U_0|^2U_0 = -iB_0, \quad (41)$$

and it can be solved exactly. For that purpose, define $A \equiv |U_0|^2$. Then, separating the real and imaginary parts of Eq. (41), it is easy to show that

$$U_{0r} = -\frac{\delta}{8B_0}A^2, \quad (42a)$$

$$U_{0i} = -\frac{1}{2B_0}A', \quad (42b)$$

and from the definition of A it follows that

$$A' = \left[A \left(4B_0^2 - \frac{\delta^2}{16}A^3 \right) \right]^{1/2}. \quad (43)$$

The exact solution of this differential equation is

$$\int_0^{\lambda^2 A} \frac{dx}{[x(1-x)(x^2+x+1)]^{1/2}} = 2B_0\lambda\theta, \quad (44)$$

where $\lambda = (\delta/8B_0)^{1/3}$. The integral can also be expressed in terms of the elliptic integral of the first kind [9] $F(\varphi, k)$, i.e.,

$$F\left[2 \operatorname{arccot} \frac{1}{3^{1/4}} \left(\frac{1-\lambda^2 A}{\lambda^2 A} \right)^{1/2}, \frac{\sqrt{2-\sqrt{3}}}{2}\right] = 3^{1/4} 2B_0\lambda\theta. \quad (45)$$

For very small or very large values of the argument of the arccot, the approximate solution is

$$A \equiv (\gamma_0\beta_1)^2 = \left(\frac{8B_0}{\delta} \right)^{2/3} \frac{\tan^2 \mu\theta}{\sqrt{3 + \tan^2 \mu\theta}}, \quad (46)$$

where $\mu = 3^{1/4}\lambda B_0$. The solution of Eq. (43) is bounded. When $\mu\theta \ll 1$, $A \approx (B_0\theta)^2$ and β_1 is proportional to θ , which is the usual linear secular solution. But the nonlinear dependence of $\gamma\beta_\theta$ on β_1 forces the solution to be bounded. Figure 7 shows β_1 and $\gamma\beta_\theta$ versus time for the parameters listed in Table III, by integrating either the

TABLE III. Parameters of the run shown in Fig. 7.

Parameter	Value
Torus major radius r_0	100 cm
Toroidal magnetic field $B_{\theta 0}$	2771 G
Initial generalized mismatch $\Delta_0 + 0.5 V_0 ^2$	0.0
Field index n	0.5
Rate of change of vertical field \dot{B}_{z0}	0.0 G/μsec
Resonance mode l	9
Amplitude of VF error δB_{z0}	0.3 G
Constant phase of VF error θ_0	0.0
Gradient of VF error K_{z0}	0.0
Initial normalized toroidal momentum $\gamma\beta_\theta$	18.1753
Initial normalized vertical velocity β_1	0.0
Initial phase of vertical velocity φ_0	0.0
Initial normalized radial bounce displacement ξ_{0r}	0.0
Initial normalized vertical bounce displacement ξ_{0z}	0.0
Integration time t_f	8 μsec

slow Eq. (40) or (36), or Eqs. (28) and (29). Integration of the exact Eq. (4) for the same parameters also gives identical results. The peak value of β_1 and the period $(\pi/\mu)r_0/c$ as computed from the approximate Eq. (46) are 0.0757 and 1.247 μ sec, respectively, in good agreement with Fig. 7.

In conclusion, our analysis indicates that there is a completely different behavior near a resonance with or without acceleration. Even at exact resonance, β_1 is always bounded without acceleration, but it is unbounded with acceleration and in the presence of a large field error.

IV. ASYMPTOTIC BEHAVIOR IN THE FRESNEL AND LOCK-IN REGIMES

In order to study the asymptotic behavior of Eq. (40), it is convenient to transform it into dimensionless form. For this purpose, when $\alpha > 0$, we introduce the quantities $\sigma = \sqrt{\alpha}\theta$, $\sigma_0 = w_0\sqrt{\alpha}$, $\hat{\epsilon} = (\delta/2\alpha^{3/2})^{1/2}B_0$, and $\hat{U}_0 = (\delta/2\alpha^{1/2})U_0$.

Then, Eq. (40) becomes

$$\frac{d\hat{U}_0}{d\sigma} + i[\sigma_0 - \sigma + |\hat{U}_0|^2 - |\hat{U}_{00}|^2]\hat{U}_0 = -i\hat{\epsilon}, \quad (47)$$

where \hat{U}_{00} is not equal to the initial value of \hat{U}_0 and will be defined shortly. Let $\hat{\epsilon}_{\text{thr}}$ be the threshold value of $\hat{\epsilon}$. When $\hat{\epsilon} \ll \hat{\epsilon}_{\text{thr}}$, i.e., when $B_0^2\delta/(2\alpha^{3/2}) \ll \hat{\epsilon}_{\text{thr}}^2$, the change in \hat{U}_0 associated with the crossing of the resonance is small, i.e., $||\hat{U}_0|^2 - |\hat{U}_{00}|^2| \ll 1$, and Eq. (47) simplifies to

$$\frac{d\hat{U}_0}{d\sigma} + i(\sigma_0 - \sigma)\hat{U}_0 = -i\hat{\epsilon}. \quad (48)$$

The crossing of the resonance occurs at $\sigma = \sigma_0$, i.e., at $\theta_0 = w_0/\alpha$. The solution of this equation is

$$\hat{U}_0 = e^{i(1/2)(\sigma - \sigma_0)^2} \left[\hat{U}_{00} e^{-i(1/2)\sigma_0^2} - i\hat{\epsilon} \int_{-\sigma_0}^{\sigma - \sigma_0} e^{-i(1/2)\sigma'^2} d\sigma' \right], \quad (49)$$

i.e., the particular solution can be written in terms of the Fresnel integral. When $\sigma_0 \gg 1$, the asymptotic expression of the Fresnel integral leads to the approximate solution

$$U_0 \approx e^{i(\omega^2/2\alpha)} \left[\left[U_{00} + \frac{B_0}{w_0} \right] e^{-i(w_0^2/2\alpha)} - i \frac{B_0}{\sqrt{\alpha}} \int_{-\infty}^{-\omega/\sqrt{\alpha}} e^{-i(1/2)\xi^2} d\xi' \right], \quad (50)$$

where the solution has been transformed to the original variables and $\omega = w_0 - \alpha\theta$. U_0 is very sensitive to the phase $w_0^2/2\alpha$, when $U_{00} + B_0/w_0 \neq 0$. Since $\alpha \ll 1$, a small change in the initial time interval $\tau_0 \equiv (r_0/c)w_0/\alpha$ from the resonance [e.g., a small change in the initial value of $(\gamma\beta_0)_0$] will cause a very different behavior of $|U_0|$ versus time. To alleviate this problem, we define the

initial condition of Eq. (50), and also of Eq. (40), by means of the initial variable \tilde{U}_{00} , i.e.,

$$U_{00} = \tilde{U}_{00} e^{i(w_0^2/2\alpha)} - \frac{B_0}{w_0}, \quad (51)$$

where $\tilde{U}_{00} = (\delta/2\alpha^{1/2})^{-1}\hat{U}_{00}$ and \hat{U}_{00} is the value in Eq. (47) around which the detuning factor is linearized. Then Eq. (50) becomes

$$U_0 = e^{i(\omega^2/2\alpha)} \left[\tilde{U}_{00} - i \frac{B_0}{\sqrt{\alpha}} \int_{-\infty}^{-\omega/\sqrt{\alpha}} e^{-i(1/2)\xi^2} d\xi \right], \quad (52)$$

and is independent of τ_0 , but it does depend on the initial phase of \tilde{U}_{00} . Equation (52) indicates that as θ tends to minus infinity, $||U_0|^2 - |\tilde{U}_{00}|^2|$ tends to zero. Therefore $|\tilde{U}_{00}|$ is the appropriate constant around which the detuning factor should be linearized, and w_0, α, δ become functions of \tilde{U}_{00} (and not of U_{00}). Because $|U_0|$ tends to $|\tilde{U}_{00}|$ as $\theta \rightarrow -\infty$ we shall call \tilde{U}_{00} the asymptotic initial value of U_0 . When $\theta \gg 1$ (or $|\omega|/\sqrt{\alpha} \gg 1$), the asymptotic value of $|U_0|$ is

$$|U_0| \sim |\tilde{U}_{00} - iB_0\sqrt{\pi/\alpha}(1+i)|. \quad (53)$$

Therefore, when $\tilde{U}_{00} \neq 0$, the final value of $|U_0|$ could be smaller than its asymptotic initial value $|\tilde{U}_{00}|$. When $\tilde{U}_{00} = 0$, the asymptotic value of β_1 is

$$\beta_1(\theta \gg 1) = \sqrt{2\pi/\alpha} \frac{B_0}{\gamma_0 + \gamma'\theta}, \quad (54)$$

where $|\gamma'\theta| \ll \gamma_0$. Since the width of the Fresnel integral is $\Delta\sigma = 2\pi^{1/2}$, we conclude that the time Δt it takes for the resonance to be crossed is

$$\Delta t = 2 \frac{r_0}{c} \sqrt{\pi/\alpha}. \quad (55)$$

Therefore the final β_1 and Δt are inversely proportional to the square root of the acceleration rate in the Fresnel regime, provided $\hat{\epsilon} \ll \hat{\epsilon}_{\text{thr}}$. Figure 8 shows $\beta_1^{(0)}$ and $(\gamma\beta_0)_0$ versus time for the parameters of Table II, except that $\delta B_{z0} = 0.1$ G, i.e., far away from the threshold. Notice the smooth variation of $\beta_1^{(0)}$ during the first microsecond and compare to the oscillatory behavior that occurs in Fig. 5(a). The difference is due to the choice of the initial condition. In Fig. 8(a), $\tilde{U}_{00} = 0$, while in Fig. 5(a), $U_{00} = 0$. When $\omega > 0$ and $|\omega|/\sqrt{\alpha} \gg 1$, i.e., well before the resonance crossing, the asymptotic value of U_0 , as given by Eq. (52), is

$$U_0 \sim \tilde{U}_{00} e^{i(\omega^2/2\alpha)} - \frac{B_0}{\omega}. \quad (56)$$

When $\tilde{U}_{00} = 0$, we have $|U_0| = -B_0/|\omega|$, which explains the smooth variation of $\beta_1^{(0)}$ in Fig. 8(a).

We have shown above that if the initial condition, given by Eq. (51), is chosen the solution of Eq. (40), in either the Fresnel or the lock-in regime, is independent of the initial time interval τ_0 from the resonance, when $w_0/\sqrt{\alpha} \gg 1$. This is no longer true if the initial condition given by Eq. (51) is chosen for the solution of Eq.

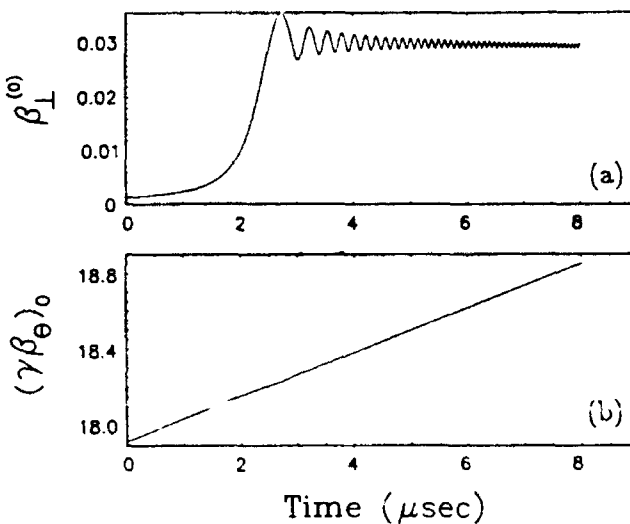


FIG. 8. β_1 and $\gamma\beta_\theta$ vs time from the slow equations of motion in the Fresnel regime far away from the threshold, i.e., for the parameters of Table II, except that $\delta B_{z0}=0.1$ G [the initial condition is given by Eq. (51), with $\bar{U}_{00}=0$].

(36), which has a nonlinear detuning factor w . The nonlinear dependence of w on θ causes the solution to depend on τ_0 . To second order in θ , the detuning factor is given by

$$w=w_0-\alpha\theta+\frac{1}{2}\alpha_2\theta^2+\frac{1}{2}\delta[|U_0|^2-|\bar{U}_{00}|^2], \quad (57)$$

where w_0, α, δ have already been defined, \bar{U}_{00} will be redefined shortly, and

$$\alpha_2=\left[3-\frac{(\gamma\beta_\theta)_0^2}{\gamma_0^2}\right]\frac{\gamma_0\gamma'}{(\gamma\beta_\theta)_0^2}\alpha. \quad (58)$$

When $w/\sqrt{\alpha} \gg 1$, i.e., well before the resonance crossing, the term proportional to δ can be neglected in Eq. (57), and the asymptotic solution of Eq. (40) is

$$U_0 \sim \exp\left(-i \int_0^\theta w d\theta\right) \left[U_{00} + \frac{B_0}{w_0} \right] - \frac{B_0}{w}, \quad (59a)$$

where

$$w=w_0-\alpha\theta+\frac{1}{2}\alpha_2\theta^2. \quad (59b)$$

Inverting Eq. (59b), we get (since $\alpha_2\theta^2 \ll 1$)

$$\theta=-\frac{w-w_0}{\alpha}+\frac{\alpha_2}{2\alpha^2}(w-w_0)^2, \quad (60)$$

and, therefore,

$$\int_0^\theta w d\theta=\left[1+\frac{\alpha_2 w_0}{6\alpha^2}\right]\frac{w_0^2}{2\alpha}-\left[1+\frac{\alpha_2}{\alpha^2}(w_0-\frac{1}{3}w)\right]\frac{w^2}{2\alpha}. \quad (61)$$

Instead of Eq. (51), where $\alpha_2=0$, if we redefine the initial condition by the relation

$$U_{00}=\bar{U}_{00}e^{i(1+\alpha_2 w_0/6\alpha^2)w_0^2/2\alpha}-\frac{B_0}{w_0}, \quad (62)$$

then Eq. (59a) becomes

$$U_0 \sim \bar{U}_{00}e^{i(1+\alpha_2 w_0/6\alpha^2)w_0^2/2\alpha}-\frac{B_0}{w}. \quad (63)$$

Notice that U_0 depends on w_0 and, therefore, on τ_0 . However, if $\alpha_2 w_0/\alpha^2 \ll 1$, then the dependence is weak and the solution of Eq. (36) with the initial condition given by Eq. (62) is also weakly dependent on τ_0 . Equation (63) indicates that as θ tends to minus infinity, $|U_0|^2-|\bar{U}_{00}|^2$ tends to zero, and, therefore, \bar{U}_{00} is the appropriate parameter around which the detuning factor should be expanded. Also, $w_0, \alpha, \alpha_2, \delta$ are functions of \bar{U}_{00} . As before, we call \bar{U}_{00} the asymptotic initial value of U_0 . From this point on, the solutions of Eqs. (28) and (29) are obtained using the initial condition computed from Eq. (62). If such an approach is not followed, each small change in the initial parameters, e.g., $(\gamma\beta_\theta)_0, B_{z0}$, etc., would produce a different U_0 which could be either in the Fresnel or the lock-in regime, to the extent that one might get the impression that the behavior is random.

An analytic expression of $\beta_1^{(0)}$ on θ , above threshold, can be easily obtained assuming that $(\gamma\beta_\theta)_0$ remains almost constant. This assumption is justified by the numerical solution of either Eqs. (28) and (29) or Eq. (36). Results are shown in Fig. 9(b) for the same parameters listed in Table II, except that $\delta B_{z0}=0.4$ G. In contrast to the solutions of Eqs. (28) and (29) or Eq. (36), Eq. (40) predicts that $(\gamma\beta_\theta)_0$ initially behaves in the same manner, but gradually increases as θ (or time) increases to very large values. The exact Eq. (4) or (12) gives also an average $\gamma\beta_\theta$ that varies as in Fig. 9(b). Since $\gamma\beta_\theta$ remains constant, on the average, after the resonance has been reached, we conclude that

$$(\gamma_0+\gamma'\theta)^2-1-|U_0|^2=\text{const.} \quad (64)$$

If the initial value $\bar{U}_{00}=0$, then at $\theta=\theta_0 \equiv w_0/\alpha$, we have $|U_0| \approx 0$ and $\gamma=\gamma_0+\gamma'\theta_0$, and Eq. (64) leads, to zero or-

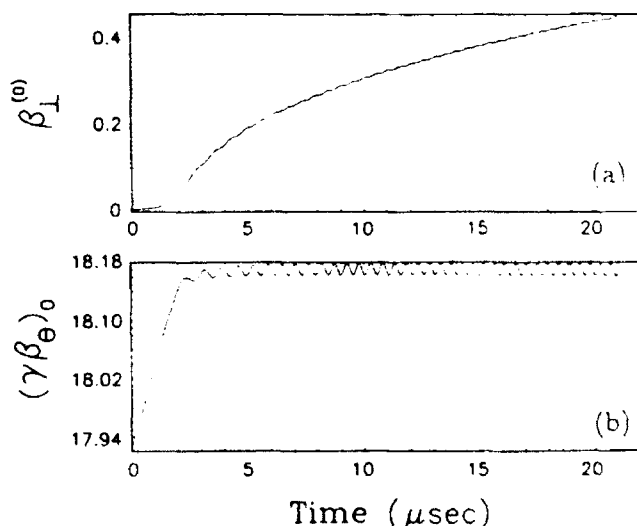


FIG. 9. Asymptotic behavior of β_1 and $\gamma\beta_\theta$ above the threshold (lock-in regime) for the parameters of Table II, except that $\delta B_{z0}=0.4$ G.

der in β_1 , to the expression

$$\beta_1^2 \approx \frac{1 + \frac{\gamma'}{2\gamma_0}(\theta + \theta_0)}{\left[1 + \frac{\gamma'}{\gamma_0}\theta\right]^2} \frac{2\gamma'(\theta - \theta_0)}{\gamma_0}. \quad (65)$$

When $\gamma'\theta \ll \gamma_0$, β_1 is proportional to the square root of time, which is demonstrated in Fig. 9(a) and also β_1 is proportional to the square root of the acceleration rate γ' . In contrast, below threshold, it has been shown that β_1 is inversely proportional to the square root of γ' .

V. DYNAMIC STABILIZATION AND THRESHOLD LAW

There are at least three possible ways to cross a cyclotron resonance without locking into it: (a) by reducing or eliminating the field errors, (b) by accelerating fast through the resonance, and (c) by adding a small time-dependent toroidal field that provides dynamic stabilization. In effect, it will be shown that the dynamic stabilization is equivalent to increasing the acceleration rate. The effectiveness of the second stabilizing mechanism is discussed at the end of this section. Here, we analyze the effectiveness of the stabilizing toroidal field, which is assumed to be sinusoidal with amplitude $\delta B_{\theta 0}$, and period τ which is much larger than the time Δt it takes to cross the resonance. The total toroidal field is described by

$$B_{\theta 0}(t) = B_{\theta 0} + \delta B_{\theta 0} \sin \frac{2\pi(t - t_d)}{\tau}, \quad (66)$$

where t_d is the time delay. Inserting Eq. (66) into Eqs. (13b) and (19b) [with the initial value $B_{\theta 0}(0)$ in b_{00}] and linearizing the detuning factor in Eq. (36), the parameters α, α_2 become

$$\alpha = \nu_{+1} \left[\lambda_0 - \kappa_0 \frac{\delta \Omega_{\theta 0}}{\Omega_{\theta 0}(0)} \cos \left(\frac{2\pi t_d}{\tau} \right) \right], \quad (67a)$$

$$\alpha_2 = \left\{ 3 - \frac{(\gamma \beta_{\theta 00})^2}{\gamma_0^2} \left[\lambda_0 \alpha + \frac{r_0 \delta \Omega_{\theta 0}}{(\gamma \beta_{\theta 00})^2} \kappa_0^2 \sin \left(\frac{2\pi t_d}{\tau} \right) \right] \right\}, \quad (67b)$$

where

$$\lambda_0 = \frac{\gamma_0 \gamma'}{(\gamma \beta_{\theta 00})^2}, \quad (68a)$$

$$\kappa_0 = \frac{2\pi r_0}{\tau c} \frac{\gamma_0}{(\gamma \beta_{\theta 00})}, \quad (68b)$$

and $\omega_0, \delta, \nu_{+1}$ are given by Eqs. (39a), (39c), and (39d). The expansion of the detuning factor in Eq. (36) is done around \tilde{U}_{00} and not around the initial value U_{00} , so that all the parameters given above depend on \tilde{U}_{00} . For simplicity, let us assume that $t_d = 0$. If the toroidal field decreases as the resonance is being crossed, i.e., if $\delta B_{\theta 0} < 0$, then according to Eq. (67a) α becomes larger. This is equivalent to replacing γ' in α with a larger effective value. It is shown shortly that the larger the acceleration

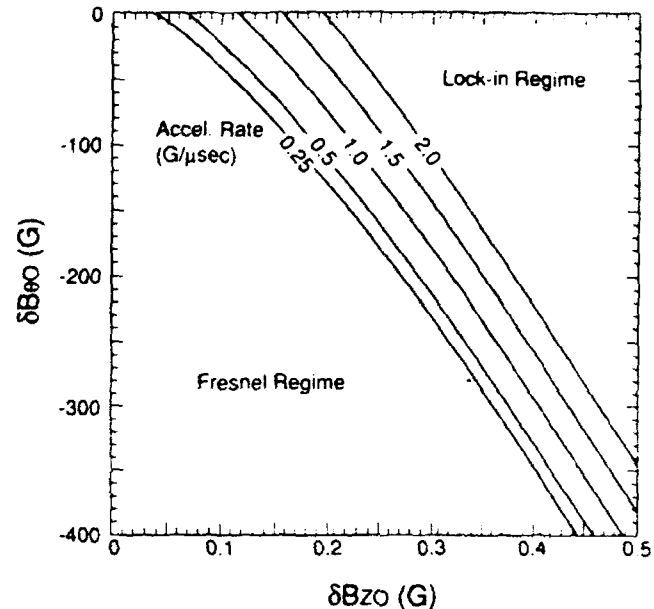


FIG. 10. Threshold law in the presence of a stabilizing time-dependent toroidal magnetic field, i.e., $\delta B_{\theta} = \delta B_{\theta 0} \sin(2\pi t/\tau)$ and zero initial perpendicular velocity ($\tilde{U}_{00} = 0$).

rate, the larger becomes the threshold value. Therefore a small time-dependent toroidal field with negative time derivative does provide dynamic stabilization.

The threshold law is obtained by determining numerically the threshold value of $\hat{\epsilon}$ in the dimensionless Eq. (47) in the special case when $\tilde{U}_{00} = 0$. Then the threshold law is expressed by the relation

$$\frac{\delta}{2\alpha^{3/2}} B_{\theta 0}^2 \text{thr} = \hat{\epsilon}_{\text{thr}}^2 \equiv 1.36. \quad (69)$$

Figure 10 gives the threshold values of $\delta B_{\theta 0}$ as a function of $\delta B_{\theta 0}$ for different acceleration rates, when $B_{\theta 0} = 2771$ G, $\tau = 50 \mu\text{sec}$, and $l = 9$. The beneficial effect of a large acceleration rate or a small time-dependent toroidal field becomes obvious from this figure. Each line in the figure separates the Fresnel from the lock-in regimes for each different value of the acceleration rate.

VI. DYNAMIC BEHAVIOR WITH INITIAL PERPENDICULAR VELOCITY

When the asymptotic initial value of U_0 is not zero, the display of the dynamic behavior close to the resonance becomes more difficult, because the dynamics depend on the initial phase as well as on the initial amplitude of \tilde{U}_0 . The results are conveniently presented as contour plots (i.e., the resonance diagrams) of the final $\beta_1 \equiv |U_0|/\gamma$ in the $\beta_1^{(0)}(0), \phi_0$ plane, where $\beta_1^{(0)}(0)$ and ϕ_0 are the amplitude and phase of the asymptotic initial value \tilde{U}_{00}/γ_0 . The rest of the parameters, including the interval of integration over θ or time, are kept constant. Since the final β_1 becomes large in the lock-in regime while it is bounded in the Fresnel regime, the contours are very dense at the boundary between the two regions.

Figure 11 shows the two regimes for the parameters listed in Table IV. Although the results shown in Fig. 11

TABLE IV. Parameters of the run shown in Figs. 11 and 12.

Parameter	Value
Torus major radius r_0	100 cm
Toroidal magnetic field $B_{\phi 0}$	2771 G
Initial generalized mismatch $\Delta_0 + 0.5 V_0 ^2$	0.0
Field index n	0.5
Rate of change of vertical field \dot{B}_{z0}	2.4 G/ μ sec
Resonance mode l	9
Amplitude of VF error δB_{z0}	0.195, 0.3 G
Constant phase of VF error θ_0	0.0
Gradient of VF error K_{r0}	0.0
Amplitude of stabilizing toroidal field $\delta B_{\phi 0}$	0, -200 G
Period of stabilizing toroidal field τ	70 μ sec
Time delay of stabilizing toroidal field t_d	0.0 μ sec
Initial normalized toroidal momentum $\gamma\beta_{\phi}$	17.922
Initial normalized radial bounce displacement ξ_{0x}	0.0, 0.003, -0.003
Initial normalized vertical bounce displacement ξ_{0z}	0.0
Integration time t_f	8 μ sec

have been obtained by integrating Eqs. (28) and (29), Eq. (36) or (40) gives the same results, provided that there is negligible bounce motion. In Fig. 11(a), δB_{z0} has been chosen equal to 0.195 G, which is very close to the threshold value when $\beta_1^{(0)}(0)$. By increasing the field error amplitude from 0.195 to 0.3 G, the lock-in regime dominates for small initial $\beta_1^{(0)}(0)$ for the entire range of

initial phase angles as shown in Fig. 11(b). By turning on the stabilizing field, the Fresnel region increases at the expense of the lock-in region. Results are shown in Fig. 11(c) for $\delta B_{z0} = 0.195$ G and $\delta B_{\phi 0} = -200$ G. This figure should be compared with Fig. 11(a) that has the same field error amplitude but not stabilizing field. Finally, in Fig. 11(d) the acceleration rate has been increased from

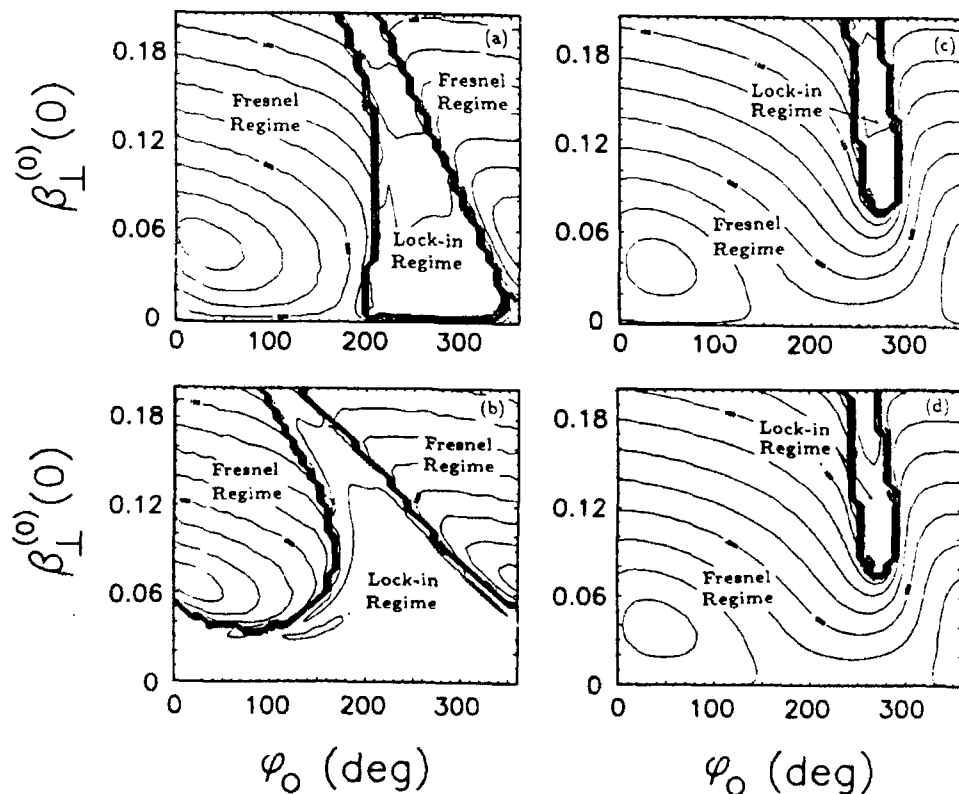


FIG. 11. Resonance diagrams, i.e., contour plots of the final β_1 , when the initial amplitude and phase of the normalized perpendicular velocity $\dot{U}_{\phi 0}/\gamma_0$ are not zero, for the parameters in Table IV, and in (a) $\delta B_{z0} = 0.195$ G, $\delta B_{\phi 0} = 0.0$ G, $\dot{B}_{z0} = 2$ G/ μ sec; (b) $\delta B_{z0} = 0.3$ G, $\delta B_{\phi 0} = 0.0$, $\dot{B}_{z0} = 2$ G/ μ sec; (c) $\delta B_{z0} = 0.195$ G, $\delta B_{\phi 0} = -200$ G, $\tau = 70$ μ sec, $\dot{B}_{z0} = 2$ G/ μ sec; (d) $\delta B_{z0} = 0.195$ G, $\delta B_{\phi 0} = 0.0$ G, $\dot{B}_{z0} = 4$ G/ μ sec.

$\dot{B}_{z0}=2$ to 4 G/ μ sec, while $\delta B_{z0}=0.195$ G and $\delta B_{\theta 0}=0$. Again, comparison of Fig. 11(d) with Fig. 11(a) shows that the Fresnel region has increased at the expense of the lock-in region. When the electrons in the ring are uniformly distributed over the initial phase angle, the resonance diagrams give, for each initial $\beta_{\perp}^{(0)}(0)$, the percentage of the ring that crosses the resonance and the percentage that locks into it.

In all the results presented so far, the equilibrium position of the bounce motion was located at the origin of the coordinate system [i.e., $\Delta_{00}+|\bar{U}_{00}|^2/2(\gamma\beta_{\theta 00})^2=0$] and the amplitude of the bounce motion was selected negligibly small (since the initial $\xi_0=0$). If the equilibrium position is chosen off the origin [i.e., $\Delta_{00}+|\bar{U}_{00}|^2/2(\gamma\beta_{\theta 00})^2\neq 0$], and the amplitude of the bounce motion is negligibly small, by judiciously choosing ξ_{00} , the resonance diagrams remain the same for the same set of parameters. When $\Delta_{00}+|\bar{U}_{00}|^2/2(\gamma\beta_{\theta 00})^2\neq 0$, and in the special case of a field index $n=\frac{1}{2}$, the parameters γ' and r_0/c in Eqs. (68a) and (68b) should be replaced by $(1+\Delta_{10})\gamma'$ and $(1+\Delta_{10})r_0/c$, respectively, where $\Delta_{10}=[\Delta_{00}+|\bar{U}_{00}|^2/2(\gamma\beta_{\theta 00})^2]/K_{100}$. Also, the initial bounce position must be equal to $\xi_{00}=\Delta_{10}$, to have bounce motion with negligible amplitude. Finally, the term

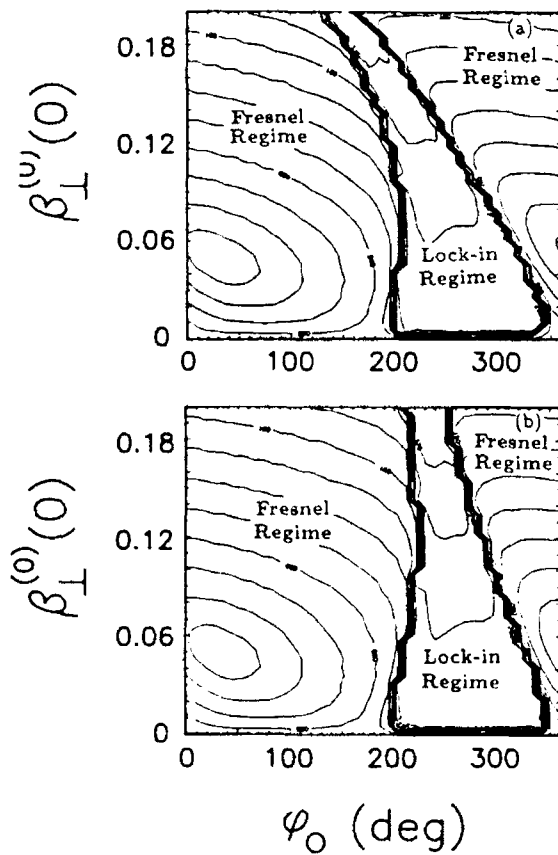


FIG. 12. Resonance diagrams for the same parameters as in Fig. 11(a), except that the radius of the bounce motion is 0.3 cm in both (a) and in (b) and in (a) the initial position of the bounce motion, i.e., $\xi_{00}=(0.3 \text{ cm}, 0.0 \text{ cm})$; in (b) $\xi_{00}=(-0.3 \text{ cm}, 0.0 \text{ cm})$.

$$(v_{-0}-2b_{00}\xi_{00}) \left[\Delta_{10} + \frac{1}{2} \frac{|U_{00}|^2}{(\gamma\beta_{\theta 00})^2} \right] / K_{100}$$

should be added to the detuning factor in Eq. (36), and, therefore, the term $(v_{-0}-2b_{00}\xi_{00})\Delta_{10}$ should be added to w_0 in Eq. (39a), where v_{-0} is the initial value of the bounce frequency.

When there is a small bounce motion superimposed to the cyclotron motion there is a modest change of the resonance diagrams. This becomes apparent by comparing Fig. 11(a) with Fig. 12. These figures have been obtained from Eqs. (28) and (29) with the same parameters, except for the initial bounce position. In Fig. 11(a), the initial position of the bounce motion is at the origin, while in Fig. 12(a), it is at (0.30 cm, 0.0 cm) and in Fig. 12(b) it is at (-0.30 cm, 0.0 cm). In the latter two cases, the amplitude of the bounce motion is 0.30 cm.

VII. MULTIPLE CROSSING OF A RESONANCE

When a small toroidal field with sinusoidal time dependence is added to the main toroidal field $B_{\theta 0}$, the detuning factor may become zero more than once, as time evolves, for the same resonance mode l . This is defined as a multiple crossing of the resonance mode l . Results are shown in Fig. 13. These results have been obtained from Eqs. (28) and (29) for the parameters listed in Table V and $\delta B_{z0}=0.35$ G. Figure 13(a) shows that the detuning factor w becomes zero five times and a Fresnel jump occurs each time the resonance mode l is crossed. It is not necessary that all the crossings have a Fresnel jump. A lock into the resonance could occur at some crossing if

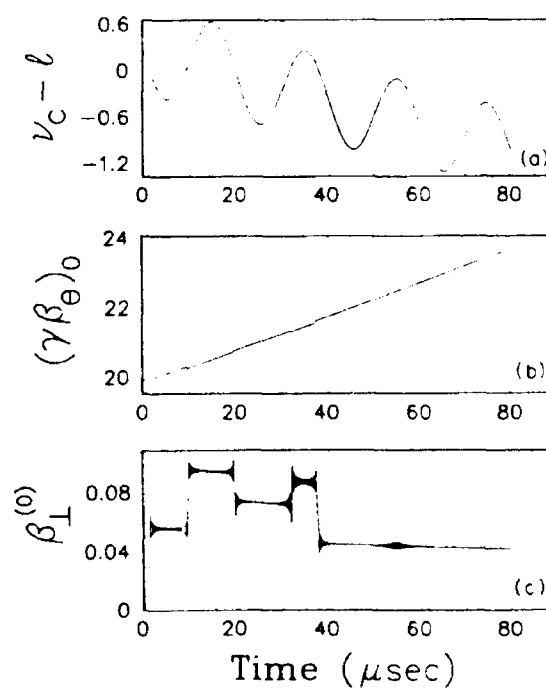


FIG. 13. $v_c - l$, $\gamma\beta_{\theta 0}$, and β_{\perp} vs time during a multiple crossing of the resonance $l=8$, obtained from the slow equations of motion [Eqs. (28) and (29)], for the parameters of Table V, and $\delta B_{z0}=0.35$ G.

TABLE V. Parameters of the run shown in Fig. 7.

Parameter	Value
Torus major radius r_0	100 cm
Toroidal magnetic field B_{∞}	2771 G
Initial generalized mismatch Δ_0	0.0
Field index n	0.5
Rate of change of vertical field \dot{B}_{z0}	0.8 G/ μ sec
Resonance mode l	8
Amplitude of VF error δB_{z0}	0.35, 1.0 G
Constant phase of VF error θ_0	0.0
Gradient of VF error K_{z0}	0.0
Amplitude of stabilizing toroidal field δB_{∞}	-200 G
Period of stabilizing toroidal field τ	20 μ sec
Time delay of stabilizing toroidal field t_d	0.0 μ sec
Initial normalized toroidal momentum $\gamma\beta_0$	19.875
Initial normalized vertical velocity β_1	0.0
Initial phase of vertical velocity φ_0	0.0
Initial normalized radial bounce displacement ξ_{0x}	0.0
Initial normalized vertical bounce displacement ξ_{0z}	0.0
Integration time t_f	80 μ sec

the asymptotic initial velocity is in the lock-in regime of the resonance diagram. As a rule, the detuning factor follows the time-dependent toroidal field. Figure 13(b) shows that when all the crossings are in the Fresnel regime, $\gamma\beta_\theta$ follows γ between crossings, while Fig. 13(c) shows that there are five Fresnel jumps in β_1 . In contrast, when the ring locks into the resonance, then $\gamma\beta_\theta$ follows the time-dependent toroidal field while w remains very small. This is shown in Fig. 14, obtained by integrating Eqs. (28) and (29), for the parameters listed in Table V and $\delta B_{z0} = 1.0$ G. According to Fig. 14(a) the first cross-

ing occurs at 1 μ sec and the ring locks into the resonance up to approximately 10 μ sec. As long as it remains locked, $w \approx 0$, while $\gamma\beta_\theta$ follows the time varying toroidal field [Fig. 14(b)]. Figure 14(c) shows that just before 10 μ sec, β_1 decreases to zero, while $\gamma\beta_\theta$ increases at a faster rate than γ . Since at this time $(\gamma\beta_1)^2 = \gamma^2 - 1 - (\gamma\beta_\theta)^2 \approx 0$, a continuously rising $\gamma\beta_\theta$ would require a negative $(\gamma\beta_1)^2$, which is an unphysical situation. Thus the ring unlocks from the resonance. The same cycle is repeated up to 45 μ sec, when β_1 , due to

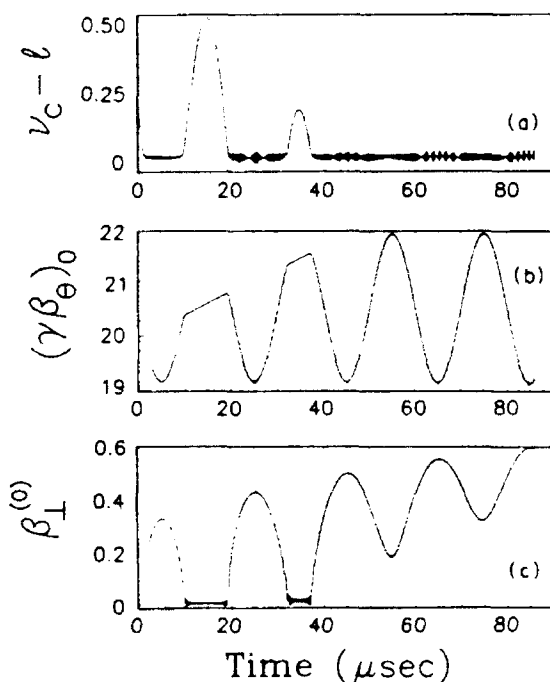


FIG. 14. $v_c - l$, $\gamma\beta_\theta$, and β_1 vs time during a multiple crossing of the resonance $l = 8$ under the same conditions as in Fig. 13, except that $\delta B_{z0} = 1.0$ G.

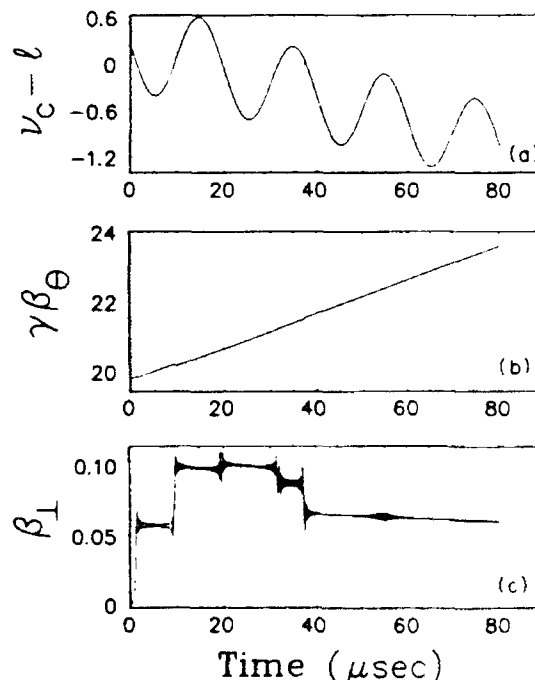


FIG. 15. $v_c - l$, $\gamma\beta_\theta$, and β_1 vs time during a multiple crossing of the same resonance $l = 8$, under the same conditions as in Fig. 13, but obtained by integrating the exact equations of motion [Eq. (4)].

the rise of its average value, cannot become zero. After this time, $\gamma\beta_\theta$ remains locked to the sinusoidal variation of the field, while ω remains almost zero. Therefore the next resonance mode $l+1$ is never reached, in spite of the fact that γ keeps increasing. The energy is transferred to $\gamma\beta_1$ rather than $\gamma\beta_\theta$. The exact Eq. (4) or (5) or the nonlinear slow Eq. (36), give identical results to those obtained from Eqs. (28) and (29) which are shown in Fig. 14. However, this is not the case with Fig. 13. Results from the integration of the exact Eq. (4) for the parameters listed in Table V and $\delta B_{z0} = 0.35$ G are shown in Fig. 15. The detuning factor and $\gamma\beta_\theta$ in Fig. 15(a) and 15(b) are very similar to the results shown in Figs. 13(a) and 13(b). However, the transverse velocity in Fig. 15(c) is similar to that of Fig. 13(c) until the third crossing occurs at 19 μ sec. The difference is due to the fact that the slow Eqs. (28) and (29) are approximate, and the phase of β_1 computed from the exact and the slow equations becomes gradually different for long times. Therefore, for long times, when many resonances are to be crossed or multiple crossing occurs, the exact Eq. (4) should be used. The slow equations provide a valuable insight in the dynamic behavior close to a particular resonance, but are not reliable over long periods of time.

VIII. SUMMARY AND CONCLUSIONS

Magnetic-field errors excite resonances that the electron ring must cross during acceleration. In the presence of a VF error, there is a threshold value of the field error amplitude that separates two distinct regimes. Below threshold (Fresnel regime) and for zero initial \tilde{U}_{00} , the perpendicular velocity increases by a finite amount as the resonance is crossed. The increase as well as the time it takes to cross the resonance are inversely proportional to the square root of the acceleration rate. Above threshold (lock-in regime), the perpendicular velocity is proportional to the square root of the acceleration rate and increases with the square root of time, while $\gamma\beta_\theta$ remains on the average constant, and the detuning factor remains extremely small. Therefore the ring locks into the resonance. The dynamic behavior without acceleration is entirely different even at exact resonance. The perpendicular velocity is proportional to time initially, but, due to the nonlinearities in the equations of motion, it reaches a maximum, then it decreases to zero and repeats periodically the same cycle. Therefore it is bounded.

The threshold is predicted by the slow equations of motion that have been derived by averaging out the fast cyclotron motion. The origin is the nonlinear dependence of $\gamma\beta_\theta$ on the perpendicular velocity and the fact that the cyclotron frequency is inversely proportional to $\gamma\beta_\theta$. By the appropriate choice of the initial conditions it was shown that the solutions of the slow or the exact equations of motion could be made weakly dependent on the initial time interval from the resonance. Possible ways to increase the threshold have been discussed. It has been shown, that the threshold value of the VF error amplitude is proportional to the $\frac{1}{2}$ power of the acceleration rate. Dynamic stabilization, i.e., the addition of a small time-dependent field to the main toroidal field, also

provides an effective increment to the acceleration rate, if it has a negative time derivative, and, therefore, increases the threshold. When the initial perpendicular velocity is not zero, the dynamic behavior has been presented by means of the resonance diagrams. These diagrams predict that a small bounce motion has only a modest effect on the Fresnel and lock-in regimes. Finally, the multiple crossing of the same resonance has been analyzed in the presence of dynamic stabilization and we have concluded that for long periods of time the exact equations of motion should be used.

Following the successful demonstration of acceleration in the NRL device, a concerted effort was made to locate and eliminate or reduce the various field disturbances that may excite the cyclotron resonance. Reduction in many of these field errors, together with the operation of higher toroidal and strong focusing fields led to beam energies in excess of 20 MeV, while the trapped current was above 1 kA.

In addition, three different cyclotron resonance stabilization techniques were tested in the NRL modified batatron: enhancement of the acceleration rate, dynamic stabilization or tune jumping, and avoidance of the resonance.

The damage done to the beam at each resonance depends on the speed with which the resonance is crossed. By enhancing the acceleration rate the resonance is crossed faster and thus the damage inflicted to the beam is reduced. To achieve higher acceleration rate, the vertical field coils were divided into two halves with midplane symmetry and powered in parallel. The experimental results show a striking reduction of the beam losses at $l=12, 11$, and 10 , when the acceleration rate increased from 0.69 to 1.93 G/ μ sec.

The crossing of the resonance can be also speeded up by modulating the toroidal magnetic field with a rapidly varying ripple. This is the dynamic stabilization or tune jumping technique and requires a carefully tailored pulse to be effective over many resonances. These results have been reported [10] previously and in general they are in agreement with the predictions of Sec. V and extensive computer calculations.

It is apparent from the resonance condition that when $B_{00}/B_{z0} = \text{const} \neq \text{integer}$, the cyclotron resonance is not excited. To test this prediction, a linearly rising toroidal field ramp ΔB_θ was superimposed on the main toroidal field. During the rise time of the ramp ($\sim 100 \mu$ sec), the ratio $B_{00} + \Delta B_\theta/B_{z0} \approx \text{const} \neq \text{integer}$. The experimental results indicate that during this time period the beam losses are completely suppressed. Although very powerful, the resonance avoidance technique by keeping the ratio $B_{00}/B_{z0} = \text{const} \neq \text{integer}$ is not practical because to be effective over the entire spectrum of l requires very high toroidal field. Among the three stabilization techniques tested, acceleration of the beam at a higher acceleration rate appears to have the highest practical potential.

ACKNOWLEDGMENT

This work was supported by the U.S. Office of Naval Research and by SPAWAR.